☐ NTNU
Norwegian University of
Science and Technology

Adaptive Resonant Controllers in a Modular Multilevel Converter

An Analytical Study of the Circulating Current
Suppressing Controller

Eivind Magnus Amundsen Kjøsnes

Norwegian University of Science and Technology
Department of Electric Power Engineering

Preface

This thesis concludes my final semester at the Norwegian University of Science and Technology. The thesis is a continuation of the specialisation project from autumn 2017, and some parts are therefore repeated in this text. The work has been under the supervision of Lars Norum at the Department of Electrical Power Engineering and in cooperation with PhD candidate Anirudh Budnar Acharya. Lars and Anirudh formulated the thesis' topic, and it has been such an exciting topic to study.

Therefore, I would like to thank my supervisor Lars Norum for accepting me as his last master student before he enters retirement. Also, I want to give my sincere thanks to Anirudh for excellent guidance and support during the thesis. I would not be able to get this far without his exceptional commitment and brilliant explanations.

The work undertaken in this thesis will result in submission of a paper for the IEEE ICIT 2019 conference. The submission deadline is set for August 2018, and thus the paper has yet not been written.

E.K.

Executive Summary

In this thesis work, the modular multilevel converter was investigated. More specifically, an analytical study of circulating current suppression methods for low-bandwidth systems was undertaken. A comparative study of two frequency adaptive digital controllers proposed in earlier research papers have been evaluated to check which yields the most efficient controller.

The modular multilevel converter (MMC) is a converter aimed for high voltage direct current applications. Compared to other voltage source converters, the MMC has several distinct advantages; high efficiency, scalability, modularity, and superior harmonic performance. One of the key advantages is its modular design. The redundancy is proportional to the number of submodules, and having multiple submodules in series gives high redundancy. If one submodule were to fail, the converter could continue to operate with high efficiency by bypassing the failed submodule.

However, its modular design does also have some drawbacks. First, the more submodules, the higher switching losses. However, the switching losses can be reduced by lowering the switching frequency. By reducing the switching frequency, the system's bandwidth reduces as well. Consequently, the controller's ability to suppress disturbances reduces. Second, a circulating current is introduced to the system. The circulating current is responsible for transferring power from the dc-link to the ac-side, and also balance the energy of the capacitors. If not controlled, the circulating current will be predominant of a second harmonic, which results in higher resistive losses. The additional resistive losses affect the lifetime of semiconductor devices and passive components due to the temperature rise.

To suppress the second harmonic during grid frequency fluctuations, studies of a digital frequency adaptive controller was undertaken. A proportional resonant controller was digitally realised in an infinite impulse response (IIR) filter. By only changing one variable, the filter adapts its resonant peak according to the measured grid frequency. A phase-locked loop was used in combination with a look-up table to measure the grid frequency and to give a new parameter for the IIR filter.

A comparative study of two frequency adaptive digital PR controllers has been undertaken. Both methods are used to change the resonant peak of the IIR filter. The first method proposed in [1] focuses on changing ω_0, while the second method proposed in [2] focuses on changing the sampling time. Both controllers were simulated in a system where the grid frequency changed from 50 Hz to 52 Hz, resulting in a 4 Hz jump in the second harmonic. A *fast Fourier transform* (FFT) analysis reveals that both methods work with high efficiency. However, in medium- and low-bandwidth systems the method proposed in [1] was able to suppress the second harmonic more effectively.

Sammendrag

Denne masteroppgaven undersøker dynamikken i en modulær multilevel omformer (MMC). En analytisk studie av ulike måter for å dempe den sirkulære strømmen i systemer med lav båndbredde har blitt undersøkt. Avslutningsvis blir to ulike frekvensadaptive kontrollere evaluert for å se hvilken som demper den sirkulære strømmen mest effektivt.

Den modulære multilevel omformeren er en omformer rettet mot høyspennings likestrømsapplikasjoner. Sammenlignet med andre variabelkildeomformere, har MMC flere fordeler; høy effektivitet, skalerbarhet, modularitet og overlegen harmonisk ytelse. En av de viktigste fordelene er dens modulære design. Å ha flere submoduler i serie gir stor redundans. Jo høyere antall submoduler, desto bedre redundans. Hvis en submodul skulle svikte, kan omformeren fortsette å operere med stor effektivitet ved å forbikoble den ødelagte submodulen.

Selv om det modulære designet gir flere fordeler så fører det også til noen ulemper. For det første, jo flere submoduler dess høyere brytertap. For å holde brytningstapene lave, kan byttefrekvensen reduseres. En konsekvens av å redusere byttefrekvensen er den reduserte systembåndbredden til kontrolleren, og kontrollerens evne til å undertrykke forstyrrelser blir lavere. For det andre innføres en sirkulasjonsstrøm til systemet. Sirkulasjonsstrømmen sørger for overføring av strøm fra DC-siden til AC-siden, i tillegg til å balansere kondensatorenes energi. Hvis ikke sirkulasjonsstrømmen blir kontrollert, vil sirkulasjonsstrømmen være dominert av en andre harmonisk, noe som resulterer i høyere varmetap. Varmetapene fører til at halvlederkomponentene aldres raskere, som igjen fører til hyppigere utskifting av halvlederkomponenter.

En digital adaptive regulator har blitt studert for å dempe den andre-harmoniske komponenten i den sirkulære strømmens under frekvensfluktuasjoner i nettet. En proporsjonal-resonansregulator har blitt realisert i et *infinite impulse response* (IIR) filter. Ved å endre på en variabel i filteret, tilpasser filteret sin resonanstopp tilsvarende til den målte nettfrekvensen slik at den andre harmoniske i den sirkulære strømmen blir redusert. En *phase lock loop* ble brukt i kombinasjon med en oppslagstabell for å gi nye parameterverdien som samsvarte med nettfrekvensen.

En sammenligning av to frekvensadaptive regulatorer har blitt gjennomført. Begge kontrollerne endrer resonanstoppen i IIR-filteret, men det gjøres ved to ulike metoder. Den første metoden publisert i [1] endrer ω_0, mens den andre metoden publisert i [2] endrer samplingstiden T_s. Begge kontrollerne ble simulert i et system hvor nettfrekvensen ble økt fra 50 Hz til 52 Hz, noe som resulterte i en økning på 4 Hz i den andre harmoniske i den sirkulære strømmen. En *fast Fourier transform*-analyse viser at begge metodene demper den andre harmoniske strømmen med stor effektivitet. Men metoden framsatt i [1] viste seg å være mer effektive i systemer med medium og lav båndbredde.

Table of Contents

Nomenclature

N	Total amount of submodules in each arm
v_{AB}	Voltage potential between node A and B.
V_C	Capacitor voltage in each submodule
C	Capacitance of the capacitor used in each submodule
$v_{u,l}$	Sum of the capacitor voltages in the upper and lower arm,
V_d	Input dc voltage
i_{diff}	Differential current
i_s	Output alternating current
$i_{u,l}$	Upper and lower arm current
I_D	dc-side current
i_{circ}	Circulating current
v_a	ac bus voltage
v_s	Output voltage
L	Arm inductance
R	Arm resistance
$n_{u,l}$	Number of inserted submodules in the upper and lower arm
i_d	DC-side current
i_u	Upper arm current
i_l	Lower arm current
v_c	Internal voltage
v_r	Resonant voltage output
m_a	Modulation amplitude
m_f	Modulation index
M	Number of phases
K_P	Proportional gain
K_R	Resonant gain
α_f	Bandwidth for the feed-forwarding bandpass filter
α_c	Controller bandwidth for the output-current
α_h	Bandwidth of resonant-controller
ω_c	Damping factor for the non-ideal PR controller
f_c	Carrier frequency
a_i & b_i	IIR parameters for the denominator and numerator, respectively
s	Continuous integral
$W_{u,l}$	Stored energy in the upper and lower arm, respectively
λ	Weighting factor
J	Weighting cost
f_{sw}, ω_{sw}	Switching frequency and

Abbreviations

MMC	Modular Multilevel Converter
PV	Photo-
HVDC	High-voltage direct-current
VSC	voltage source controller
LCC	Line-commutated converter
SM	Submodule
HB	Half-bridge
FB	Full-bridge
IGBT	Insulated-Gate Bipolar Transistor
KVL	Kirchhoff's voltage law
KCL	Kirchhoff's current law
PWM	Pulse width modulation
P, I, D, R	Proportional, integer, derivative, resonant
PWM	Pulse width modulation
PD	Phase disposition
POD	Phase opposition disposition
APOD	Alternate phase opposition disposition
PS	Phase Shifted
DSP	Digital signal processor
FPGA	Field Programmable Gate Array
CPU	Central processing unit
IIF	Infinite Impulse Response
MPC	Model predictive strategy
BPF	Bandpass filter

Chapter 1

1 Introduction

1.1 Background

In 2016, the *Paris Agreement* was signed by 195 of the world countries. The aim of the agreement was to limit the global temperature rise to well below the maximum 2 ℃ compared to pre-industrial temperature, and preferably further limit the temperature to a maximum rise of 1.5 ℃. To mention a few relevant countries, Norway has promised to limit the greenhouse emissions by 40 % compared to the 1990 levels within 2030. The *Energy Roadmap 2050* launched by *The European Commission* has set a long-term path to reduce the green gas emission up to 80-95 % by 2050 compared to the emissions in 1990. Meeting such ambitious goals require a transformation of the existing energy system. Integration of centralised multi-megawatts renewable energy sources such as solar and wind parks are highly necessary to meet the goals. Furthermore, it is also expected that the European power grid must interconnect with its neighbouring power grids; namely the North-African, Middle-East, and Russian power grids. In 2018, the supreme legislature of Norway (*Stortinget)* voted "yes" to join *ACER* (Agency for the Cooperation of Energy Regulators), meaning that Norway will tie its national grid closer to the European grid by building more subsea HVDC cables. All of the abovementioned interconnections to the European power grid lay the foundation of a *Super grid* [3], which enables electricity to flow bidirectionally on transmission highways with minimum losses.

HIGH VOLTAGE DIRECT CURRENT

The transmission losses must be reduced before the abovementioned grids can be interconnected. In the last 100 years, the favourable method for transmission power has been using alternating current (AC) as it was easier to transform to higher voltage levels. Consequently, today's electricity grid is comprised of AC transmission lines. However, AC transmission has some limitations, namely distance and transmission losses. AC cables have capacitive characteristics and are usually limited to a practical length of 50 to 60 km. The length is often limited due to its high losses and temperature rise associated with the charge and discharge of the capacitive cable. AC overhead lines have inductive characteristics, and overhead lines longer than 200 km need FACTs to compensate for the voltage drop and phase shift in the line. Thus, to effectively transmit power longer than the abovementioned distances HVDC technology can be used.

In DC, in contrast to AC, there is no generation of reactive power as the electrons flow only in one direction. In addition, a three-phase alternating current grid delivers power based on the RMS value, whereas HVDC allows transmission of power at a peak voltage level. Resulting in more power transmitted at the same peak voltage. Using the same tower body and foundations as for

AC transmission lines, HVDC can transmit more than 300 % power compared to HVAC [4]. Though HVDC has lower transmission losses, the initial cost of HVDC converter stations is costly. Therefore, HVDC transmission becomes cost-effective at lengths longer than 50-90km and 700-800 km for cables and overhead lines respectively.

MODULAR MULTILEVEL CONVERTER

Recent breakthroughs in semiconductor technology and power electronics enable new and more cost-effective voltage sources converters. In 2003, the introduction of the modular multilevel converter (MMC) was introduced by Marquardt [5]. In comparison to the two-level voltage source converter (VSC), the MMC features distinctive advantages such as 1) high efficiency, 2) redundancy, 3) scalability and modularity, and 4) superior harmonic performance for high-power applications by using a high number of identical submodules [6]. These advantages have made the MMC the preferred power electronic topology for VSC HVDC stations. Despite its many advantages, the MMC requires some very complicated control to operate correctly. For example, the circulating current within converter contributes to higher losses within the MMC. If not controlled correctly, the circulating current can cause unstable operation within the converter. In addition to the circulating current, the MMC must balance the capacitive energy within the *arms* while simultaneously transmitting power from the dc to the ac side of the converter.

However, the potential of the MMC was quickly recognised by the industry, and in 2010 the first commercial MMC HVDC was commissioned by Siemens [7]. Today there are more than 21 projects involving MMC technology [8]. To mention a few operational areas, MMC technology is used in delivering land power to offshore oil rigs, interconnecting grids, and offshore wind connections [8]. The superior and independent control of the output voltage has made the MMC the favourable choice when integrating offshore wind parks to the grid. By proper use of control techniques, the output voltage can help to stabilise the grid voltage phase and magnitude. In combination with its relative compactness, the MMC is a key enabler of offshore wind parks and electrification of oil rigs.

Bulk power transmission requires a high number of submodules as the converter can operate with high redundancy. However, having many submodules increases the switching frequency of the submodules which results in high switching losses. To keep the losses as low as possible, the switching frequency is kept low which results in a low bandwidth system. A concerning problem in low bandwidth control system is its lack of ability to suppress disturbances, often associated with frequency fluctuations. Hence, frequencies outside the initially targeted frequency are not suppressed which may result in an unstable system with higher losses.

This thesis investigates the abovementioned issue by comparing two different methods of making an adaptive control system which can suppress frequencies during grid frequency fluctuations. The method changes only one variable and can help to reduce the commission time when interconnecting two grids operating at different frequencies. In a world where profitable growth is driving the

industry, the proposed method contributes to quick installation and consequently lowering the potential commissioning time.

1.2 Problem Description

The modular multilevel converter is emerging as one of the most promising converter technologies for HVDC applications. Though the modular design offers several advantages, it also poses some challenges. Voltage imbalances between the upper and lower arm submodules give rise to a circulating current which tries to balance the submodule voltages. Without a circulating current controller, a second harmonic component will be predominant in the system, which results in an increased rms value of the arm currents. The increased rms current results in higher resistive losses, and it affects the lifetime of both semiconductor devices and passive components.

This research focuses on circulating current suppression control, especially adaptive control of the circulating current in low-bandwidth systems. It is confirmed that low-bandwidth circulating current suppression controllers are sensitive to grid frequency fluctuations. To reduce the resistive losses, and thus the lifetime of the components associated with the second harmonic component, the circulating current suppression controller must be improved. Thus, a comparative study of two state-of-the-art digital controllers proposed by previous researches is evaluated.

1.3 Thesis Outline

The thesis consists of six chapters.

Chapter 2 – This chapter gives a thorough introduction to the operating principles of the modular multilevel converter. Some of the covered topics are the topology, dynamic relationship between the output voltage and the insertion of submodules.

Chapter 3 – This chapter demonstrates current control methods which are needed for the control system. The controllers demonstrated are the output current control, circulating current control, and arm energy loop control. In addition to the controllers, it is shown how to discretise a continuous transfer function using Tustin's pre-warped approximation.

Chapter 4 – This chapter embarks on adaptive control. Mathematical derivations needed to prove that only one variable change in a biquad filter is enough to make the filter adaptive. The two adaptive, digital controllers are introduced at the end of the chapter.

Chapter 5 – This chapter presents the simulated results from two methods. Measurements of the circulating current error and FFT analysis is shown.

Chapter 6 – This section concludes the master thesis. Further work is also presented with some suggestions to get more realistic results.

Chapter **2**

2 Operating Principles

In this chapter, the topology, equations governing the fundamental dynamics of the MMC, different capacitor sorting algorithms and pulse width modulation techniques are studied. To ensure proper operation of a modular multilevel converter, it is of utmost importance to have a control system which takes the behaviour and complexity of the internal control into consideration. Therefore, strong emphasis on derivations is done.

2.1 Topology

A three-phase modular multilevel converter is shown in Figure 2.1. Each phase *(M)* is represented by a leg which consists of two separate arms; a lower and an upper. The two identical arms consist of *N* identical submodules, an arm resistor and inductor. The arm resistor represents the resistive losses in the wire and switching of the semiconductors in each submodule. The arm inductance acts as a filter to reduce high frequencies harmonics and limit the rate of current change during faults [6]. Generally, the grid and MMC is usually divided by transformer step up or down the voltage to the converter ratings. Also, the transformer gives galvanic isolation and traps the grid zero sequence currents.
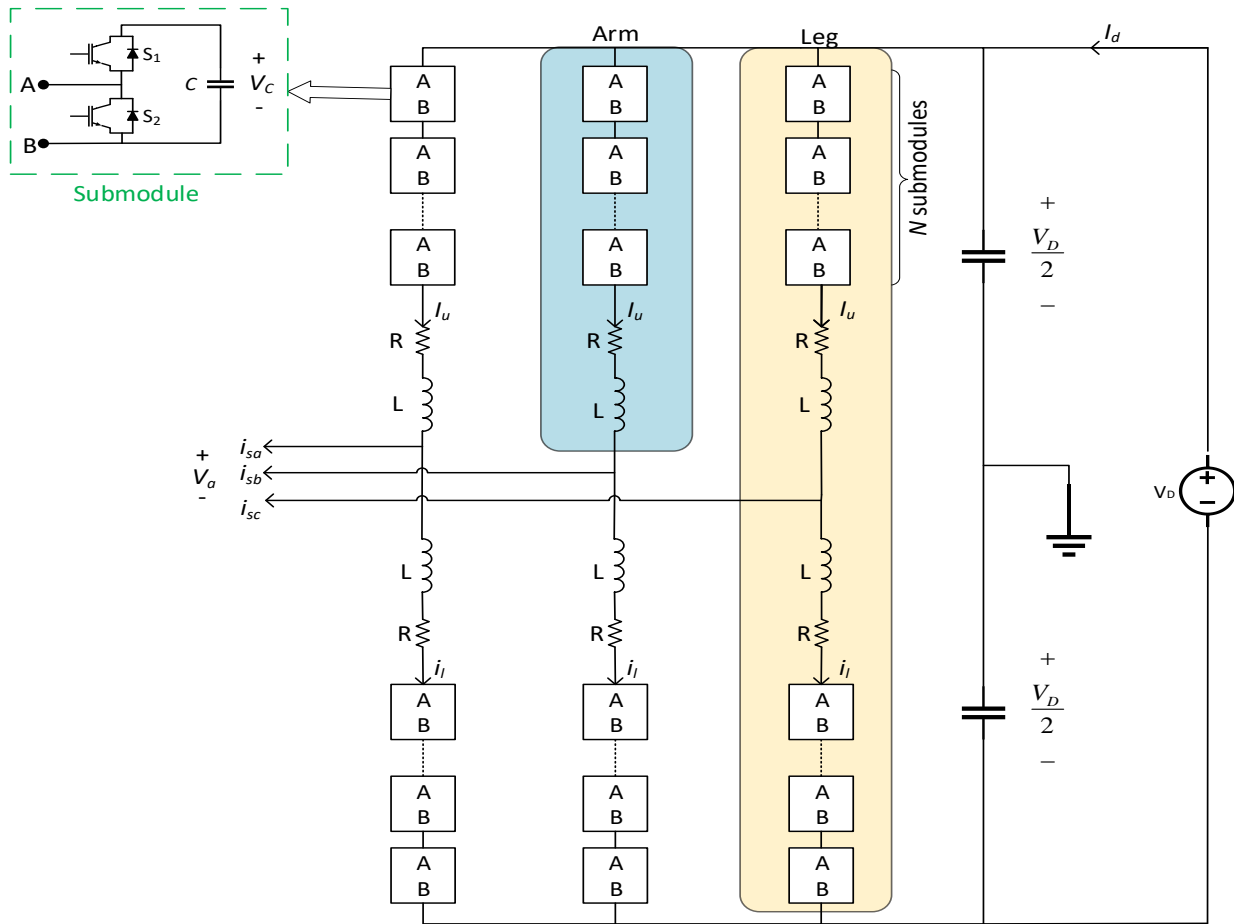
Figure 2.1 The topology of a three-phase modular multilevel converter.

2.1.1   Submodule Topology

There are several different methods of realising the submodules such as the half-bridge, full-bridge, clamp-double, three-point neutral-point-clamped. This section discusses the two most popular topologies, the half- and full-bridge. Further in this thesis, only the half-bridge submodule is considered.

HALF-BRIDGE SUBMODULE

The half-bridge submodule has two different switching states; *bypass* and *insertion*. Figure 2.2 shows the schematics of the half-bridge submodule and its operational states.

(a) Schematic overview of the half-bridge submodule

(b) Insertion, charging
$S_1{=}1$, $S_2{=}0$
$V_{AB} = V_c$

(c) Bypass
$S_1{=}0$, $S_2{=}1$
$V_{AB} = 0$

(d) Insertion, discharging
$S_1{=}1$, $S_2{=}0$
$V_{AB} = -V_c$

(e) Bypass
$S_1{=}0$, $S_2{=}1$
$V_{AB} = 0$
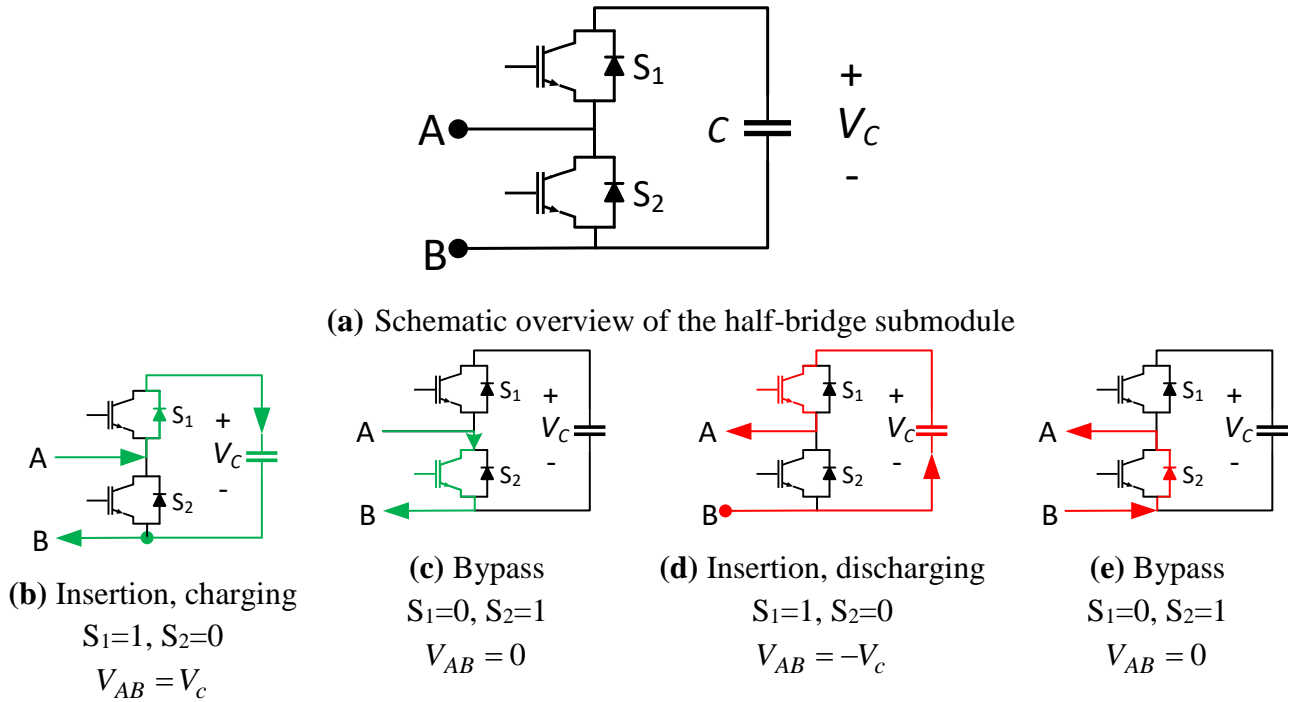
Figure 2.2 Different operational states of the half-bridge submodule.

Each submodule has a voltage $V_c(t)$ which is dependent on the current flowing through the capacitor. Considering the positive arm current as indicated in Figure 2.2 (b) and (c), the capacitor is charged when S_1 is conducting current into the positive side of the capacitor. In (c), the submodule is bypassed as the current flows through switch $S2$. Consequently, the submodule voltage remains constant. For a negative arm current, as shown in (d) and (e), the capacitor discharges when S_1 is conducting, while it is bypassed when S_2 is conducting. Therefore, the voltage of each respective submodule is expressed by the following equation

$$v_{ab} = sV_c \tag{2.1}$$

where s represents the bypass- or insertion state by 0 and 1 of switch S_1, respectively, and V_c is the submodule's capacitor voltage.

FULL-BRIDGE SUBMODULE
Unlike the half-bridge submodule, the full-bridge submodule has four operational states. Figure 2.3 shows the different states of the converter.

(a)

(b) Bypass   **(c)** Charging   **(d)** Discharging   **(e)** Bypass

(f) Bypass   **(g)** Discharging   **(h)** Charging   **(i)** Bypass
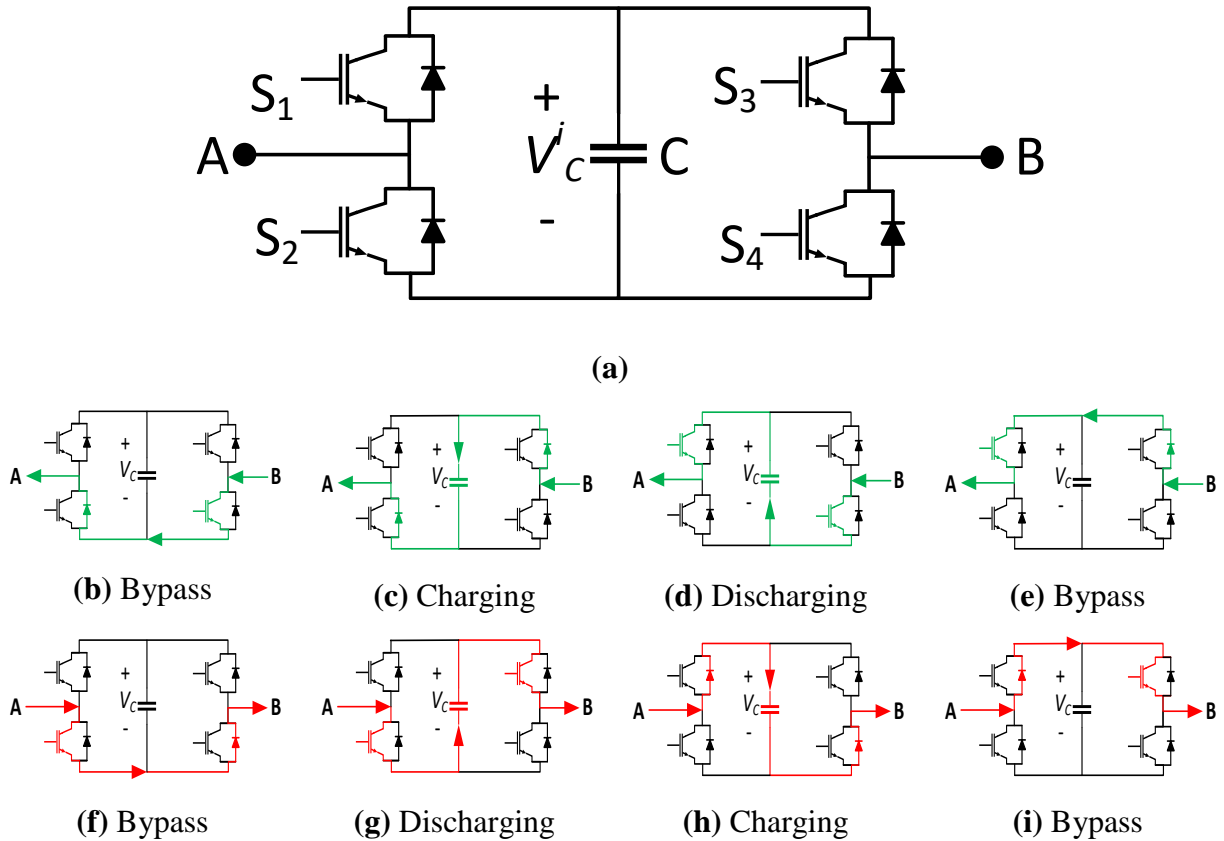
Figure 2.3 Operational states of the full-bridge submodule.

As seen in Figure 2.3, the full-bridge submodule can operate in all four quadrants and can provide bi-directional power flow. This characteristic makes the full-bridge MMC advantageous in HVDC applications as it can block a dc-side fault by generating a counter voltage [9]. This advantage makes the FB-SM very competitive compared to the HB-SM, as dc circuit breakers are both expensive and immature. The drawback of the full-bridge submodules is the number of required power electronic semiconductors, making the full-bridge submodule larger and costlier compared to the half-bridge submodule. Higher switching losses are also expected due to its double amount of semiconductor devices. However, as a FB-SM can provide bi-directional voltage, both the upper and lower arm can contribute to a voltage output twice as high compared to the HF-SM. This results in a smaller voltage across each submodule, and consequently lower rating of the capacitors may be used. Therefore, the relationship between the losses and costs of the MMC is not necessarily as high as first expected.

The MMC has issues with low-frequency voltage fluctuations in start-ups of motors or low-speed drives, and several researchers have tried to address this problem in [10-12]. Recently, a new proposed method using full-bridge submodules has been able to improve the low-frequency ripple with an injecting control scheme [12]. However, this is not further investigated in this thesis.

2.1.2   Half-Bridge vs Full-Bridge Submodule

The specific characteristics of the half- and full-bridge submodule are summarised in Table 2.1. The most evident difference between the half- and full-bridge submodule is the full-bridge submodules' bidirectional voltage capability. The full-bridge submodule can control the output voltage between positive and negative, while the voltage polarity of a half-bridge submodule is dependent on the current direction.

Table 2.1 Characteristics of the half- and full-bridge submodule

Submodule	Numbers of valves	Voltage levels	Losses	DC fault handling
Half-bridge	2	$0, v_c$	Low	No
Full-bridge	4	$0, \pm v_c$	High	Yes

The HB-SM is by far the most popular submodule as the switching and conduction losses in the IGBT are lower compared to the FM-SM. This results in a more efficient, compact and less expensive MMC. In addition, the half-bridge submodule is easier to control than the full-bridge submodule. Right now, the half-bridge is the most common used submodule modulation techniques using half-bridge submodules have been researched the most. Consequently, the advantages of the full-bridge submodule such as the blocking of a dc-side short circuit fault are usually not valued enough to be utilised in MMCs. However, this might change in the future.

2.2   Basic Operation Principles

Power electronic converters require a control system to ensure correct operation of the IGBT switching. The plant must be modelled in detail, and correct tuning of the gain is necessary to have an effective control system. Deriving equations for a desired control system can develop a dynamic simulation model of the converter. Both internal and outer control must be developed to control the internal dynamics and output of the MMC.

Figure 2.4 illustrates the operating principle of a one-phase MMC consisting of four submodules. The figure illustrates two arbitrary time intervals, T_1 and T_2, showing the switching process as submodules become inserted and bypassed. In time interval T_1, two of the submodules in the upper and lower arm is inserted. This results in an output voltage of zero voltage as the output voltage is equal to the sum of the lower and upper arm voltages. In T_2, all the lower arm submodules are inserted while the upper arm submodules are bypassed. This results in a peak output voltage equal to $V_d/2$. Similarly, the minimum output voltage is found to $-V_d/2$. The maximum and minimum output voltage yields to the following expression

$$v_s^{\max} = \frac{V_d}{2} \text{ and } v_s^{\min} = -\frac{V_d}{2} \tag{2.2}$$

Incorrect voltage balancing of the submodule's capacitors is one of the most concerning problems in the MMC. It occurs when one capacitor gets charged to a higher voltage when being inserted

for too long. A balancing current will try to equalise the voltage difference, and hence a current may flow in undesired directions inside the MMC. This current is also known as the *circulating current*, and it may flow between the upper and lower arm, as well as from leg to leg. This phenomenon is undesired, as additional current flows inside the converter. The additional current results in higher switching and conduction losses. Thus, the IGBTs must be designed for a higher current rating due to the additional temperature rise caused by the resistive losses. Consequently, a voltage balancing algorithm must be developed to prevent unnecessary high capacitor ripples. The ideal capacitor voltage is equal to the input voltage divided by the total number of N submodules: V_d / N. A circulating current control scheme and voltage balancing algorithm can be developed to achieve equal voltage over the capacitors.
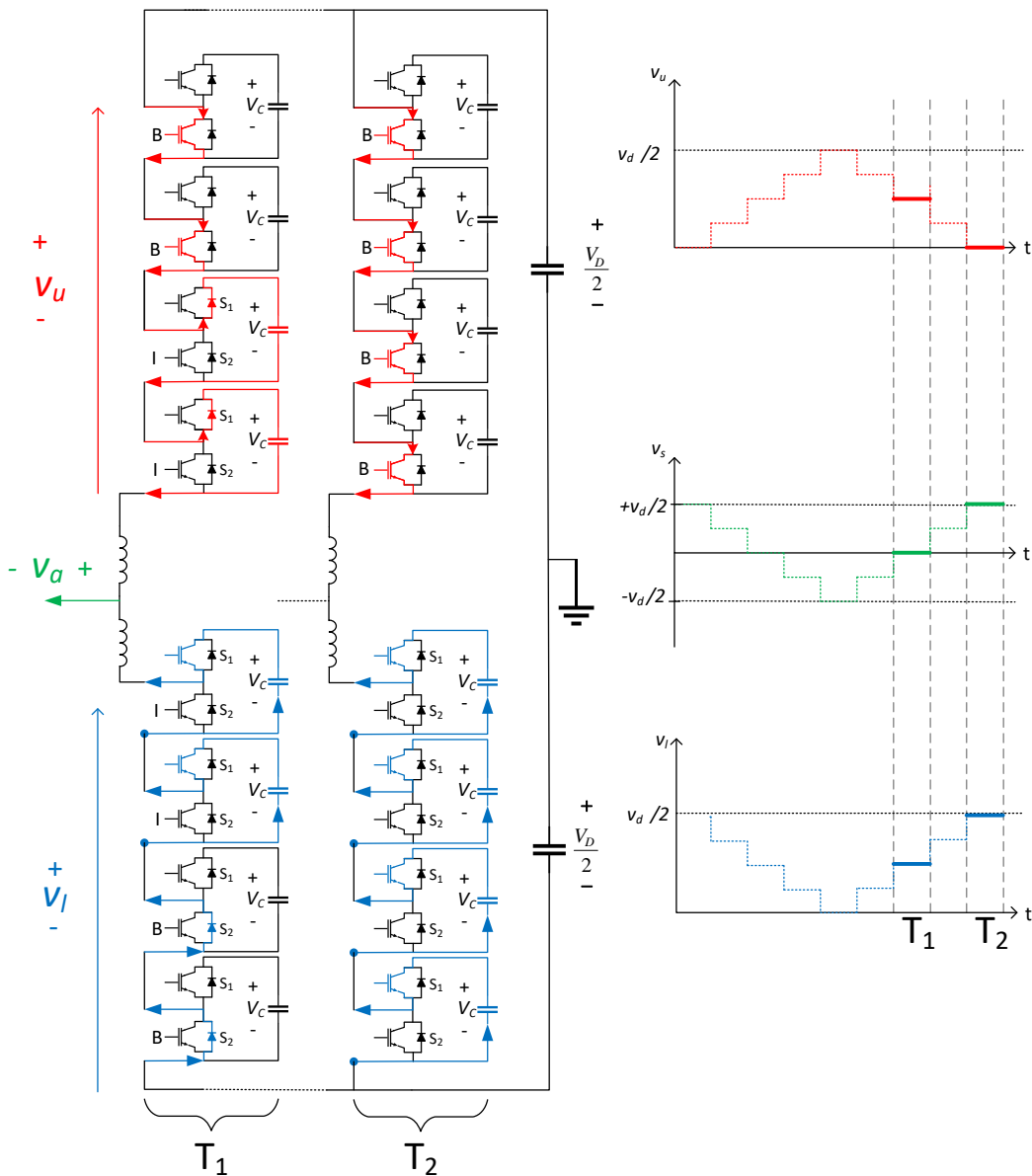
Figure 2.4 The working principle of a 4-level 1-phase MMC at two respective time intervals.

2.2.1 Dynamic Relationships – A Mathematical Approach

Average modelling is a technique that aims to reduce the computational time in a dynamic model. This technique realises a fast, reliable and efficient simulation model with high accuracy. It assumes that capacitors in the upper- and lower arm have purely capacitive characterises with the same capacitance C_d. The grid inductance and resistance are neglected to get a simplified model. Figure 2.5 shows the simplified average one-phase modular multilevel converter model.
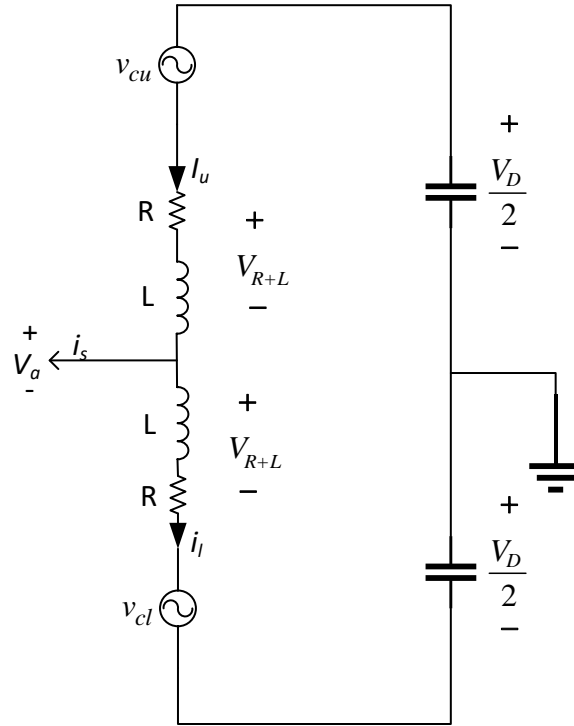
Figure 2.5 Average model of a one-phase MMC.

The MMC is considered balanced, and thus the upper- and lower arm voltage are described as

$$\overline{v_u} = \overline{v_l} = \frac{V_d}{2} \tag{2.3}$$

The output current is found by applying KCL to Figure 2.5

$$i_s = i_u - i_l \tag{2.4}$$

The output and circulating currents are expressed by the upper and lower currents

$$i_u = \frac{i_s}{2} + i_{circ} \qquad\qquad i_l = -\frac{i_s}{2} + i_{circ} \tag{2.5}$$

where

$$i_{circ} = \frac{i_u + i_l}{2} \tag{2.6}$$

The circulating current consists of two currents; a direct and alternating current. The alternating current is undesirable in the converter as it contributes to higher resistive losses, and consequently lowering the efficiency of the converter. To keep the converter losses as low as possible, the alternating current should be kept as low as possible. Thus, the circulating current should preferably be purely dc

$$\overline{i_u} = \overline{i_l} = \overline{i_{circ}} = \frac{\overline{i_{dc}}}{M} \tag{2.7}$$

DYNAMIC RELATIONSHIPS OF THE CURRENTS
A dynamic representation of the currents is found by applying KVL to Figure 2.5. The following equations are derived for the upper and lower arm

$$v_a = \frac{v_d}{2} - L\frac{di_u}{dt} - Ri_u - v_{cu} \tag{2.8}$$

$$v_a = -\frac{v_d}{2} + L\frac{di_l}{dt} + Ri_l + v_{cl} \tag{2.9}$$

By adding (2.8) to (2.9), the following equations can be obtained

$$v_a = \underbrace{\frac{1}{2}(v_{cl} - v_{cu})}_{v_s} + \frac{L}{2}\frac{d}{dt}\left(\underbrace{i_l - i_u}_{-i_s} \right) + \frac{R}{2}\left(\underbrace{i_l - i_u}_{-i_s} \right) \tag{2.10}$$

$$\frac{L}{2}\frac{di_s}{dt} = v_s - v_a - \frac{R}{2}i_s \tag{2.11}$$

Based on equation (2.11) it can be seen that the output current i_s is driven by the output voltage, which is the sum of the capacitator voltages divided by two

$$v_s = \frac{v_{cl} - v_{cu}}{2} \tag{2.12}$$

Based on equation (2.12), the maximum and minimum voltage can be achieved by bypassing and inserting the submodules in a proper manner. The maximum output voltage is achieved when bypassing all the upper arm submodules and inserting all the lower arm submodules. Similarly, the minimum voltage is achieved by inserting all the upper arm submodules and bypassing the lower arm submodules. The respective mathematical expression for the maximum and minimum voltage yields

$$v_{cu} = 0 \text{ and } v_{cl} = v_{cl}^{\Sigma} \rightarrow v_s^{max} = \frac{v_{cl}^{\Sigma}}{2} \tag{2.13}$$

$$v_{cl} = 0 \text{ and } v_{cu} = v_{cu}^{\Sigma} \rightarrow v_s^{max} = -\frac{v_{cu}^{\Sigma}}{2} \tag{2.14}$$

The rate of change of the circulating current is found by subtracting (2.8) by (2.9) the rate of change of circulating current can be obtained

$$0 = \frac{v_d}{2} - \frac{L}{2}\frac{d}{dt}\left(\underbrace{i_u + i_l}_{2i_{circ}}\right) + \frac{R}{2}\left(\underbrace{i_u + i_l}_{2i_{circ}}\right) - \underbrace{\frac{1}{2}(v_{cu} + v_{cl})}_{v_c} \tag{2.15}$$

$$L\frac{di_{circ}}{dt} = \frac{v_d}{2} - Ri_{circ} - v_c \tag{2.16}$$

Based on (2.16), the internal voltage v_c drives the circulating current. To have a pure dc circulating current, the controller must regulate the internal voltage to approximately $v_c = v_d/2 - Ri_{circ}$. The switching losses R can be neglected, and the internal voltage must be approximately $v_c \approx v_d/2$. If the closed-loop voltage controller is operated correctly, the circulating current will become a pure dc-component as the rate of change is zero. It is desirable to have a pure dc-component as the MMC becomes easier to control and to have lower switching losses.

2.2.2 Basic Voltage Control Methods

INTERNAL CONTROL
As seen in (2.16), ac parts of the circulating currents occur when the voltage between the upper and lower arm are unequal. The circulating currents cause the overall efficiency to decrease. The arm voltages are equal to the sum of each the capacitors, and the following equation

$$v_{cu,l} = \sum_{i=1}^{N} n_{u,l}^i v_{cu,l}^i \tag{2.17}$$

where $n_{u,l}^i = 1$ represents the inserted state, and $n_{u,l}^i = 0$ represents the bypass-state. An average value of the submodule insertion indices can further be developed by

$$n_{u,l} = \frac{1}{N}\sum_{i=1}^{N} n_{u,l}^i \tag{2.18}$$

where $n_{u,l} = 1$ indicates that all submodules are inserted, while $n_u = 0$ indicates that all submodules are bypassed. Information from equation (2.17) and (2.18) yields an expression for the inserted arm voltage in terms of insertion index to become

$$v_{u,l} = n_{u,l} v_{cu,l}^{\Sigma}$$
(2.19)

An average dynamic expression for the circulating current is found by substituting equation (2.19) is substituted into (2.11) and (2.16), and the following expressions are found

$$\frac{L}{2}\frac{di_s}{dt} = \underbrace{\frac{-n_u v_{cu}^{\Sigma} + n_l v_{cl}^{\Sigma}}{2}}_{v_s} - v_a - \frac{R}{2}i_s$$
(2.20)

$$L\frac{di_{circ}}{dt} = \frac{v_d}{2} - \underbrace{\frac{n_u v_{cu}^{\Sigma} + n_l v_{cl}^{\Sigma}}{2}}_{v_c} - Ri_{circ}$$
(2.21)

In the two above equations, it is seen that the output current and circulating current are dependent on the switching of the upper and lower arm capacitors. The primary goal is to maintain and operate the upper and lower arm to an equal voltage by controlling each switch. In a high-power MMC, there may be hundreds of submodules per arm, and the complexity of controlling the switches in a dynamic model may be immense. A more straightforward method of controlling the capacitator voltages are desired, and by focusing on the average voltage of the capacitors simplifies the model. Remembering that the current through a capacitator is expressed by $i = C\,dv/dt$, the equations can be further simplified. The circulating current is then reformulated to

$$i_{circ} = \sum_{k=1}^{N} C\underbrace{\frac{dv_{u,l}^k}{dt}}_{dv_{u,l}^{\Sigma}/dt} = \sum_{k=1}^{N} n_{u,l}^k i_{u,l} = i_{u,l}\underbrace{\sum_{k=1}^{N} n_{u,l}^k}_{N\cdot n_{u,l}}$$
(2.22)

By rearranging (2.22) it becomes

$$\frac{C}{N}\frac{dv_{cu,l}^{\Sigma}}{dt} = n_{u,l}i_{u,l}$$
(2.23)

By inserting for the upper and lower current using equation (2.5), the following two equations are formulated for the upper and lower capacitator voltages

$$\frac{C}{N}\frac{dv_{cu}^{\Sigma}}{dt} = n_u\left(\frac{i_s}{2} + i_c\right)$$
(2.24)

$$\frac{C}{N}\frac{dv_{cl}^{\Sigma}}{dt} = n_l\left(-\frac{i_s}{2} + i_c\right)$$
(2.25)

Equations for the output and circulating current, governed by (2.20) and (2.21), and equations for the upper and lower arm currents, governed by (2.24) and (2.25), adequately describe the average dynamic model of the modular multilevel converter. By proper mathematical manipulations, these

four equations lay the foundation for defining new, informative equations about the converter's dynamics. For example, describing the difference and sum of the leg voltages can be achieved by proper analytical derivation [13]. By multiplying $v_{cu,l}^{\Sigma}$ respectively to both sides of (2.24) and (2.25)

$$\frac{dW_u}{dt} = \left(v_c^* - v_s^*\right)\left(\frac{i_s}{2} + i_c\right) \tag{2.26}$$

$$\frac{dW_u}{dt} = \left(v_c^* + v_s^*\right)\left(-\frac{i_s}{2} + i_c\right) \tag{2.27}$$

By introducing the imbalanced energies $W_{\Sigma} = W_u + W_l$ and $W_{\Delta} = W_u - W_l$, the energy equations are derived by respectively adding and subtracting equations (2.26) and (2.27)

$$\frac{dW_{\Sigma}}{dt} = 2v_c^* i_c - v_s^* i_s \quad \text{and} \quad \frac{dW_{\Delta}}{dt} = v_c^* i_s - 2v_s^* i_c \tag{2.28}$$

Assuming that v_c^* and i_c are purely dc, and considering the output voltage and current to be sinusoidal, equation (2.28) is deducted to

$$\frac{dW_{\Sigma}}{dt} = v_d I_c - \frac{\hat{V}_s \hat{I}_s}{2}\cos\varphi - \frac{\hat{V}_s \hat{I}_s}{2}\cos\left(2\omega_0 t - \varphi\right) \tag{2.29}$$

$$\frac{dW_{\Delta}}{dt} = \frac{v_d \hat{I}_s}{2}\cos\left(\omega_0 t - \varphi\right) - 2\hat{V}_s i_c \cos\left(\omega_0 t\right) \tag{2.30}$$

During balanced conditions, the phase output energy $1/2\hat{V}_s\hat{I}_s\cos\varphi$, must equal the dc input energy $v_d^* i_d$. Integration of equations (2.29) and (2.30) gives the sum and energy change

$$W_{\Sigma} = \underbrace{\frac{Cv_d^2}{N}}_{W_{\Sigma 0}} - \underbrace{\frac{\hat{V}_s \hat{I}_s}{4\omega_0}\sin\left(2\omega_0 t - \varphi\right)}_{\Delta W_{\Sigma}} \tag{2.31}$$

$$W_{\Delta} = W_{\Delta 0} + \underbrace{\frac{v_d \hat{I}_s}{2\omega_0}\sin\left(\omega_0 t - \varphi\right) - \frac{2\hat{V}_s i_c}{\omega_0}\sin\left(\omega_0 t\right)}_{\Delta W_{\Delta}} \tag{2.32}$$

where $W_{\Sigma 0}$ and $W_{\Delta 0}$ are the resulting mean values found by the integration. Under balanced conditions, the mean value of the energy ripple in (2.32) must be zero. Consequently, the energy ripple and imbalance energy are governed by the twice and fundamental frequency respectively.

The energy within one capacitor is calculated using the formula for the energy within one capacitor $W = 1/2\,CV^2$. The initial energy, the first term in equation (2.31), within the arm is found by using the average voltage and capacitance of the arm. The capacitors are in series, and hence the total equivalent capacitance within one arm is expressed by C/N. Using that the average voltage across the two respective arms are expressed by $\bar{v}^{\Sigma}_{cu,l} = v_d/2$, the initial energy can be calculated by summing the energy within both arms

$$W_{\Sigma 0} = \frac{C v_d^2}{N} \tag{2.33}$$

Similarly, the energy sum and change within one arm can be found using W_u and W_l.

Expressing the change and sum of voltage capacitors can be done by use of mathematical manipulations of the equations governing the dynamics of the MMC. The simplified equations yield

$$v_c^{\Sigma} = v_{cu}^{\Sigma} + v_{cl}^{\Sigma} \approx 2v_d + \frac{N}{C v_d}\Delta W_{\Sigma} \tag{2.34}$$

$$v_c^{\Delta} = v_{cu}^{\Sigma} - v_{cl}^{\Sigma} = \frac{N}{C v_d}\Delta W_{\Delta} \tag{2.35}$$

Based on the equations (2.31) and (2.32), both equations are governed by the fundamental and twice the fundamental frequency. Both equations are also inversely proportional to the capacitance.

2.2.3   Insertion Indices – The Ideal Selection

As discussed and seen in Figure 2.4, the output voltage is dependent on the summation of the upper and lower voltages. These voltages are controlled by the switches, which either cause the submodule to bypass or insert the capacitator. Selection of the ideal insertion indices n_u and n_l are calculated using the reference values of the internal and output voltage, v_c^* and v_s^*. By subtracting and adding the expression for v_s and v_c given in equations (2.20) and (2.21), the following expression of the insertion indices for the lower and upper arm are calculated

$$n_u = \frac{v_c^* - v_s^*}{v_{cu}^{\Sigma}} \qquad\qquad n_l = \frac{v_c^* + v_s^*}{v_{cl}^{\Sigma}} \tag{2.36}$$

The equations governing the insertion indices in (2.36) are used in a technique named *Closed-loop voltage*. Out of the many other voltage control methods, this master thesis uses this method as it gives no parasitic components ω_0 and $2\omega_0$ in the circulating current [14]. This method gives an asymptotically stable system. However, the internal dynamics will be marginally stable as the insertion indices in (2.36) may cancel the capacitor voltages in the equations governing the dynamics of the converter in equation (2.20) and (2.21).
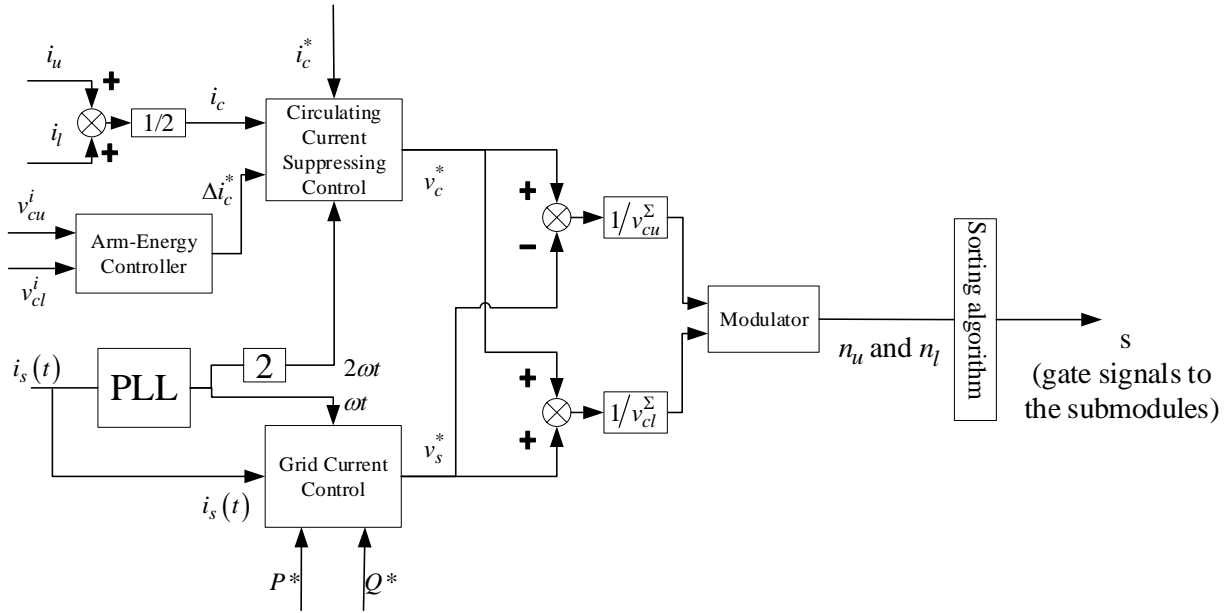
Figure 2.6 Schematic overview of the closed-loop voltage control method [13].

The disadvantage of the closed-loop voltage control method is that it requires measurement of all submodule capacitors, which is used to calculate the energy in the submodules. In a modular multilevel converter containing up to 200 submodules in one arm, this method requires significant computational processing power. In addition, the voltage measurements require space. In applications where space is limited, such as electrification of off-shore oil rigs or HVDC power conversion from offshore wind power, it is desired to keep the space as small as possible. The *open-loop voltage control* requires less space as it does not use voltmeters to measure the voltage. However, the open-loop voltage control method requires high computational power as it estimates the energy level with use of mathematical equations. The open-loop voltage control will not be further used in this thesis as the closed-loop energy control works sufficiently in simulations.

Another method, which requires less computational power is the *direct-voltage control.* It also achieves low asymptotically stable system, though with some parasitic components of the ω_0 and $2\omega_0$ in the circulating current. Thus, the disadvantages of direct-voltage control are the parasitic components which contribute to harmonics in the output and internal voltage. However, these components can be suppressed using the *closed-loop voltage control* mentioned above. A typical control structure for a one-phase modular multilevel converter using the direct voltage control is shown in Figure 2.7.
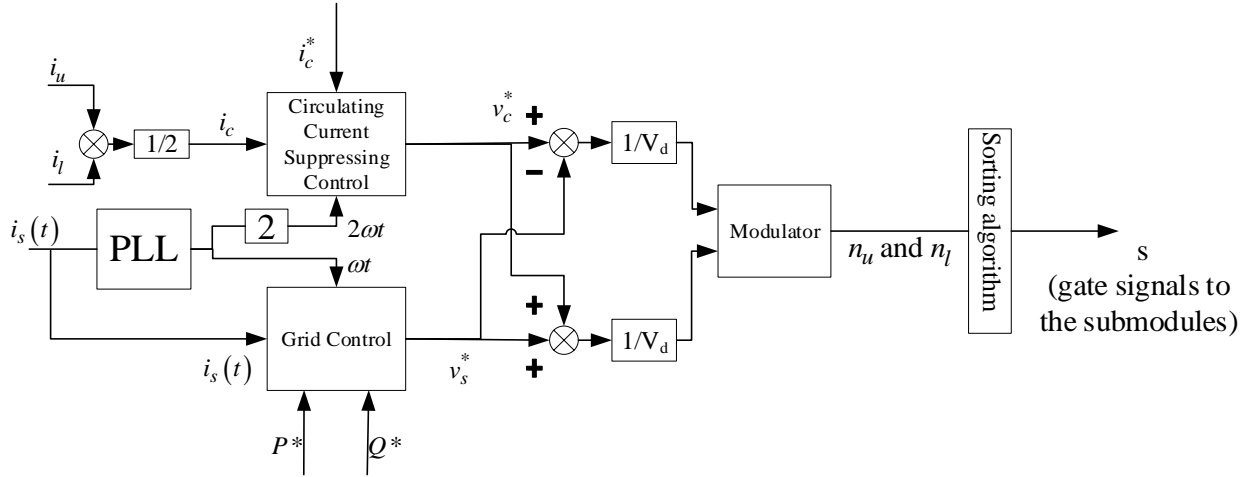
Figure 2.7 Schematic overview of the direct voltage control method [13].

Figure 2.7 illustrates that the internal reference voltage is obtained from the circulating current controller which is fed by the measured upper and lower arm voltages, which forms the circulating current. Similarly, the output reference voltage is found. Using the signals fed from the controller, the PWM modulator manipulates the signal to generate the submodule insertion indices for the upper and lower arm.

This thesis will use both the *direct-voltage* and *closed-loop voltage control* as the scope of this thesis is to investigate the adaptive circulating current controller.

2.2.4   Submodule Capacitor Voltage Balancing

Each modular multilevel converter topology needs an active capacitor voltage balancing algorithm to maintain the submodule capacitor voltage at V_{dc}/N [6]. Having an equally charged capacitors help to lower the circulating current as there is no voltage potential drop between the submodules. One of the critical technical problems associated with submodule capacitor voltage balancing is to carry out the switching without imposing unnecessary switching transitions among the submodule capacitors. There are many different types of voltage balancing methods, and this subsection will briefly mention: *Basic Sorting, Predictive Control*, *Reduced sorting switching* and *Capacitor Tolerance Band.*

BASIC SORTING ALGORITHM

One of the most widely accepted balancing algorithms is based on a PWM and sorting strategy [6]. The method used in [15] demonstrates this methodology, and it is a simple yet efficient method. It is based on measuring all the capacitor voltages and sorts the capacitor voltages in descending order. Depending on the current direction, the choice of switching is based on the most extreme capacitor voltages and whether the switching counteracts the deviation from the average submodule voltage. The four most basic cases for submodule switching are shown below.

   1.   Positive arm current and a submodule should be inserted

- The least charged bypassed submodule is inserted to be charged, whereby the voltage will start to approach the average voltage.

2. Negative arm current and submodule should be inserted

- The highest charged bypassed submodule is inserted to be discharged, whereby the voltage will decrease the average voltage

3. Positive arm current and submodule to be bypassed

- The highest charged submodule is bypassed as the charging will stop. Consequently, the capacitor voltage will not further deviate from the average voltage.

4. Negative arm current and submodule to be bypassed

- The least charged submodule capacitor is bypassed as discharging will stop. Consequently, the voltage will not further deviate from the average voltage.

Figure 2.8 demonstrates the four above stages using a flowchart.
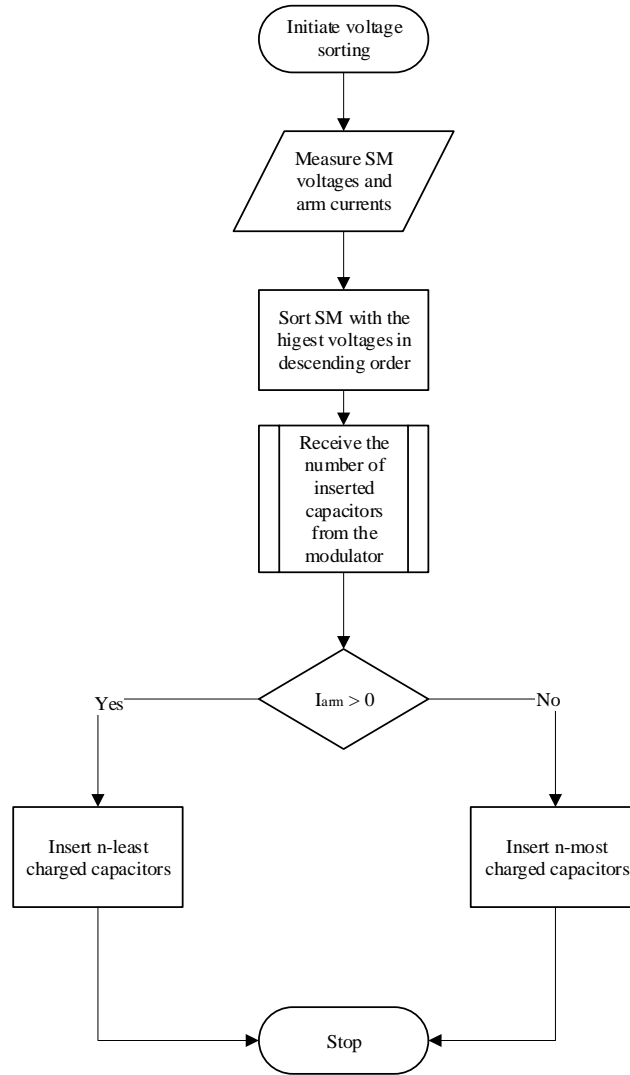
Figure 2.8 Step-by-step representation of the balancing algorithm [6].

The main advantage of this method is its simplicity. The only mathematical operation is a comparison of the capacitor voltages. The computational power is low, and the sorting algorithm can be deployed in simple hardware such as an FPGA.
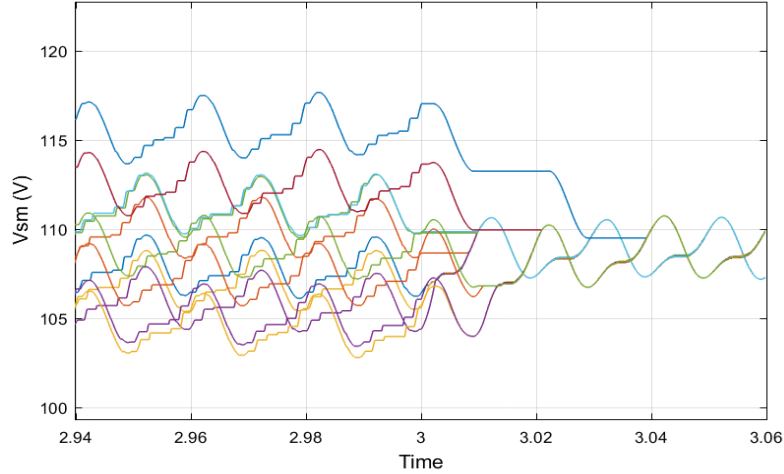
Figure 2.9 Sorting algorithm activated at t=3.0 s.

Figure 2.9 demonstrates the effectiveness of the sorting algorithm as it is activated at t = 3.0 s. Shortly after activation, the voltage narrows down to the average value. Though, the effectiveness of the sorting algorithm is strongly dependent on the switching frequency. A higher switching frequency allows for faster sorting of the capacitors. The disadvantage of higher switching frequency is the high switching losses caused by the on-/off-switching of the semiconductor device.

In the following two subsections, more efficient and complex methods focusing on reducing the switching losses are described.

PREDICTIVE CONTROL

Recent papers suggest using predictive control of the submodule voltages [15-18]. The capacitor voltage balancing proposed in [16] utilises a discrete-time predictive model of the MMC system. The proposed *model predictive strategy* (MPC) predicts the next step of the variables of the MMC utilising a cost function associated with the control objectives. All possible switching states are evaluated, and the control system chooses the selection which results in the minimum costs. The following equation describes the cost function

$$J'_{jk} = J_{jk} + \lambda_{Ck} \left(\sum_i \left| V_{cijk}(t+T_s) - \frac{V_{dc}}{N} \right| \right) \tag{2.37}$$

where λ is the weighing factor to achieve the lowest possible voltage deviations and j is the phase. The predictive voltages for the inserted and bypassed submodules are shown below

$$V_{Cijk}(t+T_s) = V_{Cijk}(t) + \frac{i_m(t)}{C} T_s \tag{2.38}$$

$$V_{Cijk}(t+T_s) = V_{Cijk}(t) \tag{2.39}$$

The predictive model used in [18] approaches the problems differently. Instead of defining a specific cost function, this method combines a predictive error sorting method and a conventional sorting algorithm. By defining an acceptable range of capacitor voltage ripple, the discharging and charging of the capacitors may last longer as long as the voltage level is within the acceptable voltage range. This allows for a lower switching frequency, and consequently lower switching conduction losses inside the MMC. The method utilises the same predictive voltage equations (2.38) and (2.39) with a combination of the predicted error

$$V_{err,ij} = \left| V_{cij}\left(t + T_s\right) - V_{c,ref} \right| \tag{2.40}$$

The predicted deviation from the nominal value is compared to a prespecified voltage ΔV_c. If the error voltage is higher than ΔV_c the conventional sorting algorithm is done. If the error voltage is smaller than ΔV_c a predictive sorting algorithm is applied. Figure 2.10 demonstrates the method.
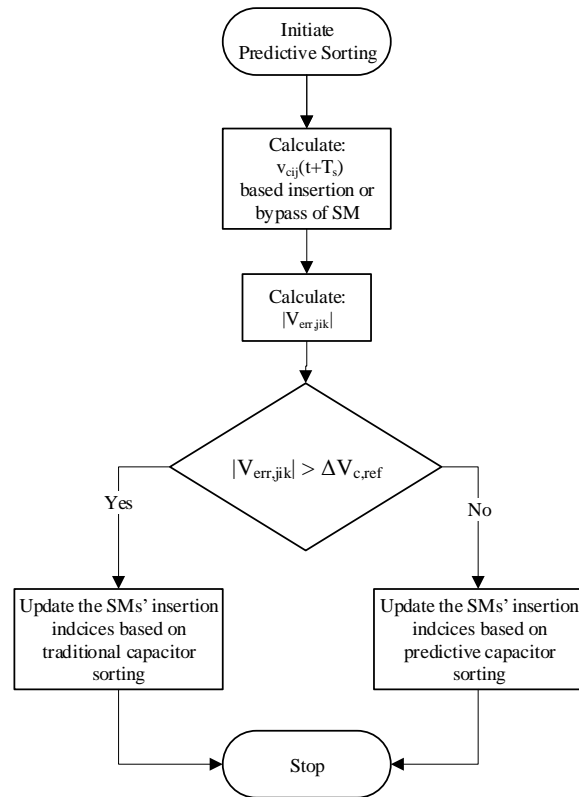
Figure 2.10 The flowchart demonstrates the predictive sorting algorithm [18].

To summarise, the predictive capacitor voltage balancing algorithms mentioned above reduces the switching losses by lowering the switching frequency. In terms of computational complexity, the predictive algorithm requires a fast-computing digital controller in order to run the algorithm in each defined time cycle.

CAPACITOR TOLERANCE BAND (CTB)

Another approach to effectively reduce the switching losses is the capacitor tolerance band (CTB) [19]. This method defines a specific tolerance band where the voltages must stay within. The tolerance band is defined by the maximum allowable voltage ripple δ deviation from the mean average voltage, and hence the tolerance band $v_{cu,l} - \delta \leq v_{cu,l}^{i} \leq v_{cu,l} + \delta$. There is no need for sorting the capacitor voltages if the voltages are within the specified interval. However, if the voltage exceeds the band, the sorting of the capacitors must be performed according to the four cases shown in section *Basic Sorting Algorithm*. A flowchart demonstrating this method is shown below
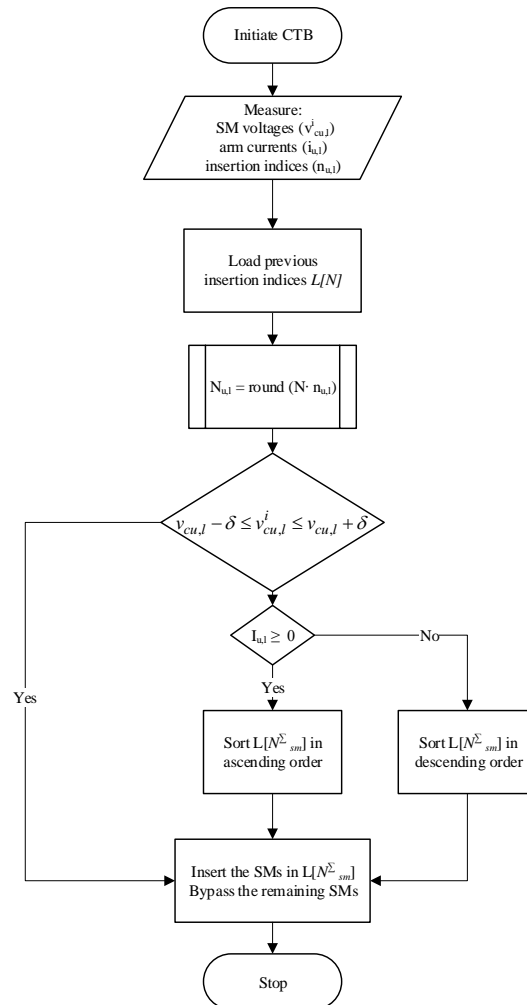
Figure 2.11 The Flowchart demonstrates the capacitor tolerance band [19].

This method utilises the whole available voltage band, thus switching is only done when it is necessary. This method dramatically reduces the number of switching made to balance the capacitors.

2.3 Pulse Width Modulation – Carrier Based Modulation

There are two different main techniques for modulation signals to the MMC, namely the *Carrier-based* and *Non-carriers based.* There is also a third category, the hybrid method, which is a combination of the two methods. However, this thesis will use the carrier- method as the concept is easier to grasp and overall it has shown good performance. Explanations and simulations of the method are provided, and Simulink Models are derived and put in Appendix C.

The carrier-based technique is the traditional method of modulating PWM signals. This method compares triangular carriers to a reference sinusoidal wave. If the reference value is higher than the triangular carrier, this generates an "on"-signal. Throughout a sinusoidal reference wave, the pulse will alternate between "on" and "off", and that is how gate signals are generated. By adding all the average values of each on/off duty cycle, a sinusoidal wave is created.

This subsection will provide examples and simulations for the *Phase Disposition PWM (PD-PWM)*, *Phase Opposition Disposition PWM* (*POD-PWM*), *Alternate Phase Opposition Disposition PWM* (*APOD-PWM*) and *Phase-Shift PWM (PS-PWM).*

2.3.1 Phase Disposition-PWM (PD-PWM)

This method is called the *Phase Disposition PWM*, which is one of the most widely used strategies for MMC due to its superior harmonic performance compared to the APOD [20]. By performing an FFT analysis on the phase legs, it can be confirmed that most of the distributed harmonics in the phase legs cancel each other. Hence, the output line-to-line voltage contains low harmonic distortion [20-22].
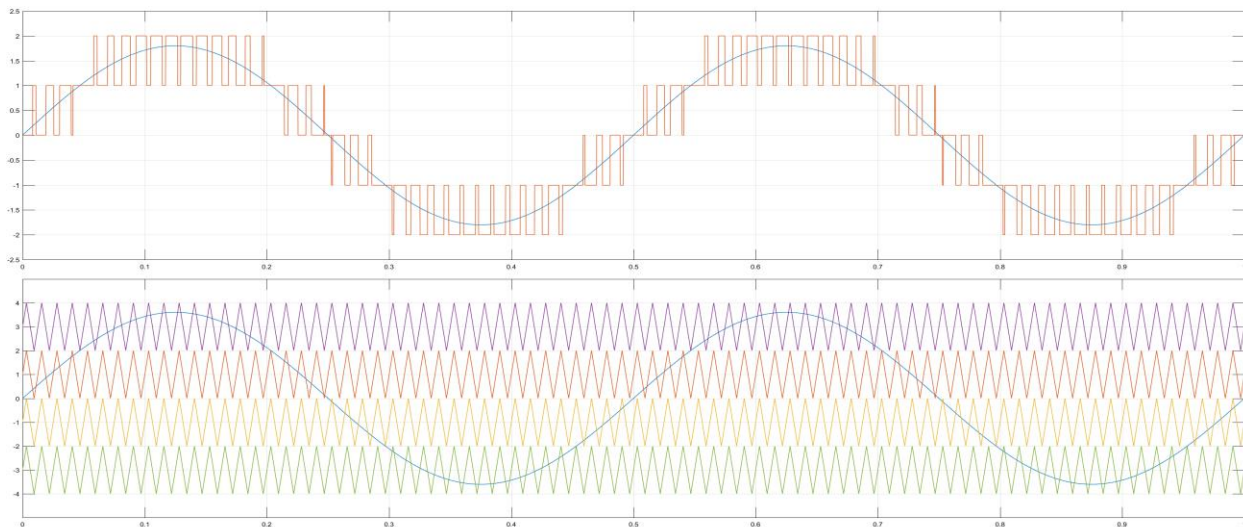
Figure 2.12 Modulation signals using PD-PWM with m_a = 0.9 and m_f =40.

The number of triangular carriers is equal to the amount of SMs, and they have the same phase and magnitude. The magnitude of each carrier is equal to the maximum dc voltage divided by the number of submodules; V_{dc}/n. Thus, the different voltage levels of the converter are 0V, $\pm V_{dc}/2$

and $\pm V_{dc}/4$. The different voltage levels occur as the sinusoidal reference signal is either higher or lower than two upper or lower carriers. To achieve a smoother output waveform with more voltage levels, simply more capacitors can be added.

2.3.2 Phase Opposition Disposition PWM (POD-PWM)

In the POD-PWM, the upper carriers are in phase, and the lower carriers are in opposition, meaning they are 180° phase shifted. The frequencies of the carriers are the same, but the amplitude of the carriers may differ from each other. As in the PD-PWM, each submodule has its carrier wave. The modulation is shown below.
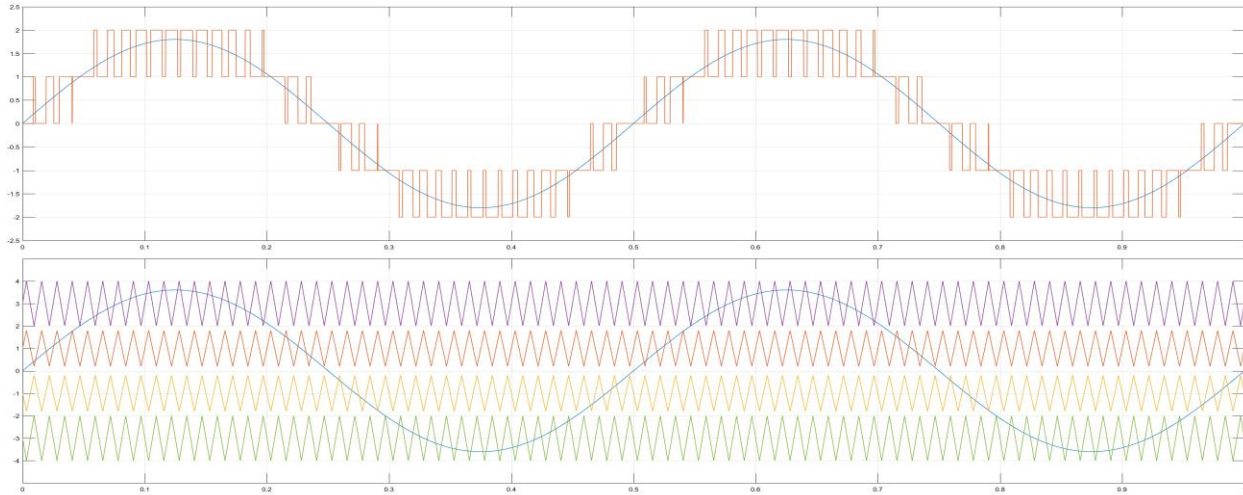
Figure 2.13 Modulation signal using POD-PWM with m_a = 0.9 and m_f =40.

The POD-PWM technique ensures that n-number of submodules are inserted at all times. Hence, the voltage across the inductor will become zero [23]. Remembering from equation (2.16), the rate of change for the differential current was based on the inductor voltage.

$$L\frac{di_{circ}}{dt} = \frac{v_d}{2} - \underbrace{\frac{n_u v_{cu}^\Sigma + n_l v_{cl}^\Sigma}{2}}_{v_c} - Ri_{circ} \qquad (2.41)$$

If the inductor voltage is zero, the circulating current will become a pure dc-component.

The POD-PWM has one distinct disadvantage compared to the PD-PWM; the poor THD performance[20]. In the PD-PWM, most of the harmonics were cancelled in the common-node due to the symmetrical signal. The POD-PWM lacks this feature, and a filter is required to ensure low harmonics.

2.3.3 Alternate Phase Opposition Disposition PWM (APOD-PWM)

In the APOD-PWM all carriers have the same frequency but are phase shifted by 180 degrees to the neighbouring carrier.
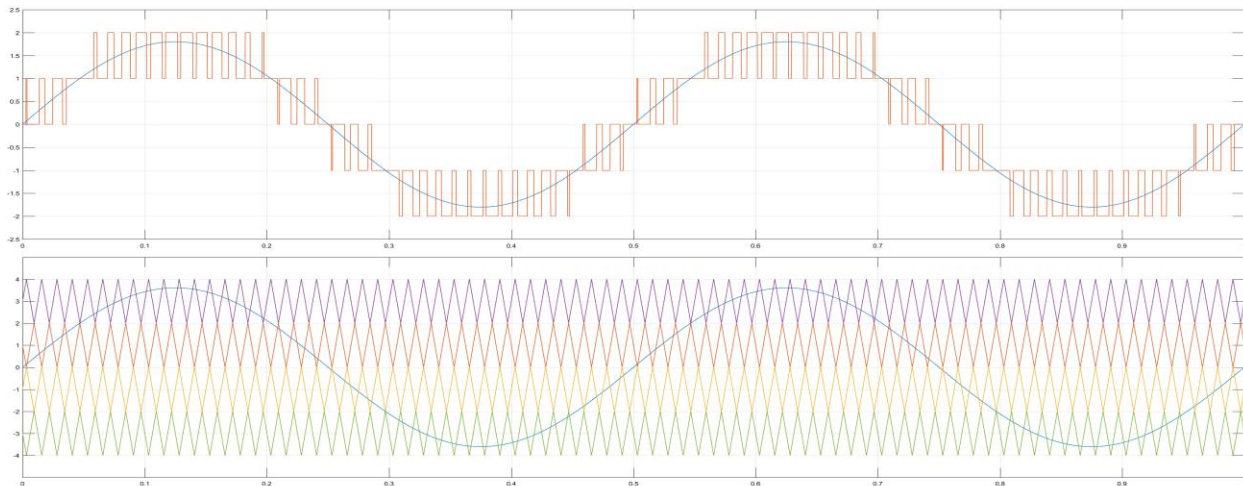
Figure 2.14 Modulation signal using APOD-PWM with $m_a = 0.9$ and $m_f = 40$.

The operation of the APOD-PWM is very similar to the POD-PWM, and they have the same exact operation in the three-level converter [20]. Hence, the same advantages for the POD-PWM can be mentioned here as well.

2.3.4   Phase-Shifted PWM (PSC-PWM)

The PS-PWM is a widely used PWM strategy for the MMC [24]. The carrier frequencies are the same, but every carrier is phase shifted by 90 degrees compared to its neighbour. Figure 2.15 shows the result. The performance of the PSC-PWM is very close to the PD-PWM [21].
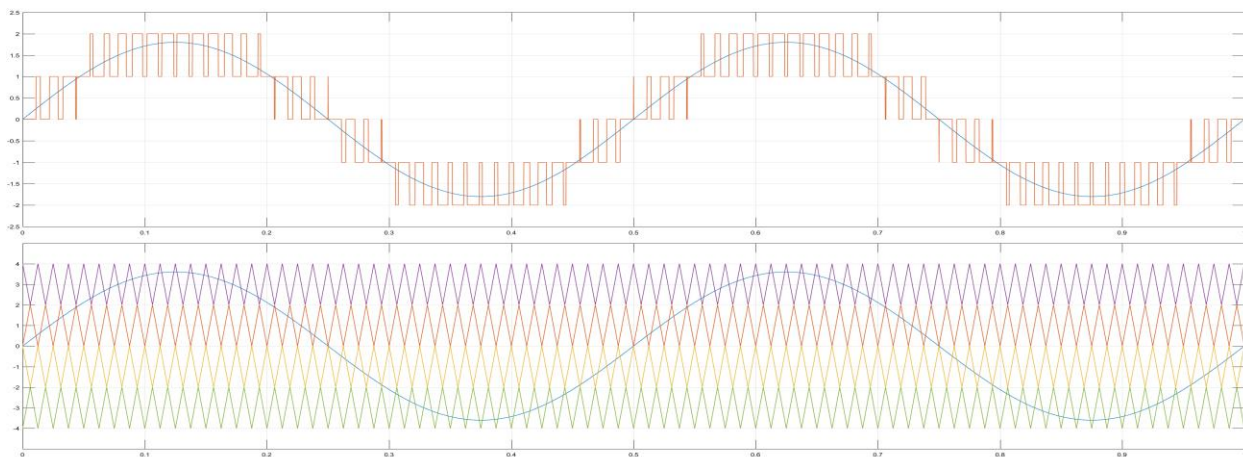
Figure 2.15 Modulation signal using the PS-PWM with $m_a = 0.9$ and $m_f = 40$.

In terms of THD, the PD-PWM performs better during normal and over-modulated carriers, but at the cost of higher switching frequencies [21]. Consequently, higher losses are inevitable in the PD-PWM technique. Thus, this thesis will use the PS-PWM for generation of gate pulses. This is based on the good THD performance at low switching frequency.

Chapter 3

In this section, utilisation of *a proportional-resonant regulator to control the output current and the circulating current to operate the MMC satisfyingly. The controller investigated and used in this section is the proportional-resonant (PR) controller due to its superior ability to track a sinusoidal signal accurately* [25]. *Also, it is shown how the circulating current can be used to balance the submodule capacitor voltages using the closed-loop voltage control. Also, discretising and parametrisation of the PR controller is done to realise its properties in an infinite impulse response filter.*

3 Current Control Methods

Current regulators play a vital role in the modular multilevel converter. The primary goals of the current regulators are summarised to the following three points [26]: 1) avoiding overloading conditions by limiting the peak current, 2) accurately track a reference signal during transient and steady-state conditions to minimise the steady-state magnitude and phase error, resulting in a high-efficiency converter, 3) compensate for low-order harmonics associated with voltage ripples on dc-link and ac-side, converter dead time delays and semiconductor voltage drops.

There are two alternatives for regulating the current; *nonlinear current regulators* and *linear current regulators* [26]. The nonlinear current regulator uses either of the following three methods for regulating the current: 1) Model predictive control, 2) Hysteresis current control and 3) Fuzzy logic control. Of the nonlinear current regulators, the hysteresis current control is the preferred nonlinear current regulator in fast switching VSIs due to its very rapid dynamic response. The hysteresis current control predefines an "error-hysteresis" boundary which the error current must operate within. If the error current exceeds the boundary, the phase legs are switched to compensate for the error. This instantaneous operation is advantageous as it enables rapid regulation of peak currents and limiting second order distortion effects. The disadvantage is the variable switching frequency that may occur, and thus it must be matched with a specific load system. The linear current regulator focuses on minimising the current error by controlling the pulses generated in the PWM. The most used strategies are synchronous reference *dq*-frame [27], stationary frame proportional-integer (PI) controller, and the proportional resonant controller (PR) [28].

3.1 Current Controllers and Tuning

As shown in Chapter 2, the equation governing the dynamics of circulating current was derived in (2.21). The plant model is found by applying Laplace transformation to the s-domain, and equation (3.1) shows the equivalent expression

$$G_p(s) = \frac{1}{sL_{arm} + R_{arm}} \left(\frac{v_d}{2} - v_c \right) \qquad (3.1)$$

The controller must account for the plant dynamics as well as disturbances such as dc-voltage. The schematics of the circulating current control scheme is drawn in Figure 3.1.
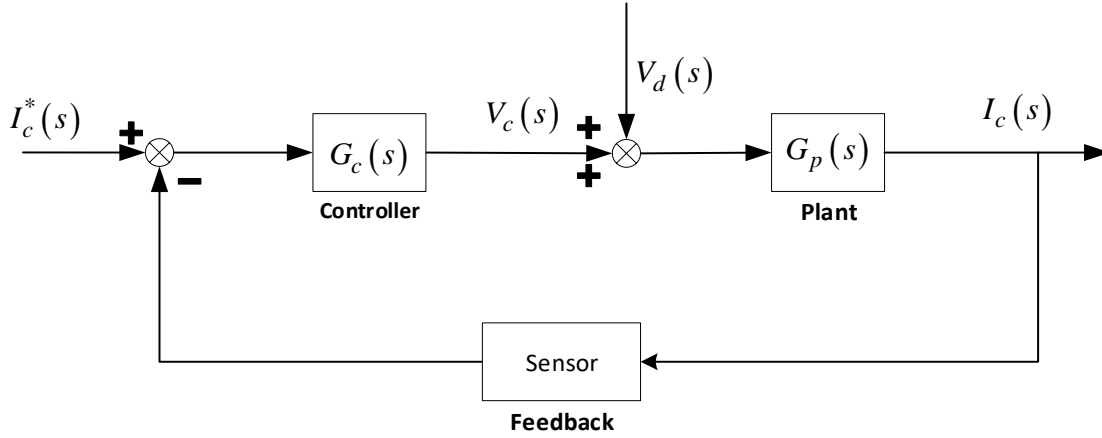
Figure 3.1 Block diagram of the circulating current controller [29].

In a real system, the output from the circulating current controller, $V_c(s)$ is fed to a pulse-width modulator to generate gate signals to the plant. In terms of analysing the dynamic properties of the circulating and output current, the time delay which is caused by the sampling rate when generating PWM signals is neglected.

Using superposition on Figure 3.1, the closed-loop transfer function is given by

$$I_c(s) = \frac{G_c(s)G_p(s)}{1 + G_c(s)G_p(s)} I_c^*(s) - \frac{G_p(s)}{1 + G_c(s)G_p(s)} V_d(s) \qquad (3.2)$$

The $G_c(s)$ is designed to minimise the steady-state error between the I_c and I_c^*, and at the same time minimising the error caused by disturbance V_d [29]. In principle, this is achieved by tuning the gain of $G_c(s)$ to the maximum. To get a higher understanding of the dynamics of the system, a transfer function for the error current consists of the following two elements

$$\Delta I_c(s) = \underbrace{\frac{1}{1 + G_c(s)G_p(s)} I_c^*(s)}_{\Delta I_T(s)} + \underbrace{\frac{G_p(s)}{1 + G_c(s)G_p(s)} V_d(s)}_{\Delta I_D(s)} \qquad (3.3)$$

which identifies the *closed-loop tracking error sensitivity* and *closed-loop disturbance rejection error*, respectively. Both of the above terms can be expressed as a ratio of the reference and disturbance, and hence the following expression

$$E_T(s) = \frac{\Delta I_T(s)}{I_c^*} = \frac{1}{1 + G_c(s)G_p(s)} \tag{3.4}$$

$$E_D(s) = \frac{\Delta I_D(s)}{V_d(s)} = \frac{G_p(s)}{1 + G_c(s)G_p(s)} \tag{3.5}$$

The minimal steady-state error is achieved by minimising the ratios of $E_T(s)$ and $E_D(s)$. It is done by maximising the gain of the controller.

The ratio of the disturbance to the tracking sensitivity is given by

$$\frac{E_D}{E_T}(s) = G_p(s) = \frac{1}{sL_{arm} + R_{arm}} \tag{3.6}$$

Interestingly, equation (3.6) implies that the ratio of disturbance to tracking sensitivity is independent of the controller but dependent on the plant's parameters; R_{arm}, L_{arm} and frequency. To simplify (3.6), the plant time constant is introduced $\tau_p = L_{arm}/R_{arm}$. Equation (3.6) yield to

$$G_p(s) = \frac{1}{R_{arm}(1 + s\tau_p)} \tag{3.7}$$

3.1.1   Introducing the Proportional Resonant (PR) Controller

LIMITATIONS OF THE PI CONTROLLER

The most widely used controllers are the variations of the proportional integer derivative (PID) controller, and it is used in more than 90 % of control loops used in the process industry [13]. A simple method to check the suitability of a PI controller for the MMC is to consider a sinusoidal current flowing through an inductor in a closed-loop system with negligible resistance. Figure 3.2 demonstrates the system. The output reference voltage, v^*, from the PI controller is the applied voltage across the inductor, and i is the current flowing through the inductor.
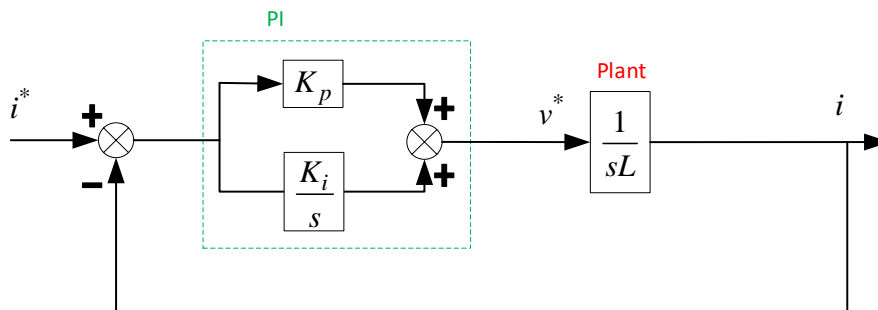
Figure 3.2 A PI controller used to regulate the current flowing through an inductor.

The closed-loop transfer function of the system illustrated in Figure 3.2 is given by

$$G_{cl}(s) = \frac{G_{PI}(s)G_p(s)}{1 + G_{PI}(s)G_p(s)} = \frac{sK_p + K_i}{s^2 L + sK_p + K_i} \tag{3.8}$$

Furthermore, the zero steady-state error is found when the closed-loop transfer function $G_{cl}(s = j\omega) = 1$:

$$G_{cl}(s = j\omega) = \frac{j\omega K_p + K_i}{-\omega L + Ki + j\omega K_p} \tag{3.9}$$

By analysing the transfer function in (3.9), zero static gain is only achieved when $\omega=0$. In all other cases where $\omega > 0$, the tracking capability and phase error of the closed-loop system will always be $|G_{cl}(j\omega)| \neq 1$ and $\angle G_{cl}(j\omega) \neq 0$. In conclusion, the PI controller is not suitable for an MMC as it can't track sinusoidal signals. Consequently, another controller is necessary.

Though, the above conclusion is only the case when considering a controller to regulate a one-phase converter. In a three-phase converter, the currents can be transformed to the *dq*-synchronous reference frame using *Park's transformation*. In such a case, the currents will appear as two constants in a balanced system, and therefore two PI controllers, for the *d*- and *q*-component respectively, are needed to control the currents. For unbalanced conditions, a positive and negative-sequence component will occur in the current, and hence additionally two PI controllers are needed for the two respective sequences [30]. Consequently, the total amount of PI controllers needed to control the current sums up to four. However, this thesis will only consider a one-phase controller, and therefore the synchronous reference frame will not be further studied in this thesis.

PROPORTIONAL RESONANT (PR) CONTROLLER

In response to PI controller's lack of ability to track an alternating current, the proportional resonant controller was introduced to achieve zero steady-state error [31]. Evidently from its name, the PR controller consists of a proportional part and resonant part. The resonant part of the PR controller is based on a bandpass filter (BPF) with the following transfer function [13]:

$$G_R(s) = \frac{K_R(s\cos\phi_R - h\omega_0 \sin\phi_R)}{s^2 + \alpha_R s + (h\omega_0)^2} \tag{3.10}$$

where α_R is the resonant passband bandwidth, K_R is the resonant gain, and ϕ_R is the compensation angle. By setting the passband of the bandwidth to zero, $\alpha_R=0$, and compensation angle to zero, $\phi_R= 0$, the resonant filter yields an infinity gain at the resonant frequency $h\omega_0$. This results in an ideal resonant controller. Together with its proportional part, the *ideal PR controller* is formed. The transfer function of the ideal PR controller is shown in the below function.

$$G_c(s) = K_P + \frac{K_R s}{s^2 + (h\omega_0)^2} \qquad (3.11)$$

where ω_0 is the fundamental frequency and h is the harmonic order of the tracked frequency. For fixed-point digital implementation of the PR controller, it is preferred to introduce a damping factor ω_c in the denominator [29]. The damping factor limits the infinity gain of equation (3.11) to a finite value. The finite gain gives a finite precision for digital systems, and hence, the controller requires less computing power for processing the signal [28, 32]. The new PR controller yields to [28, 32]

$$G_{PR}(s) = K_P + \frac{K_R s}{s^2 + \omega_c s + (h\omega_0)^2} \qquad (3.12)$$

where ω_c is the resonant cut-off frequency, also known as a *damping factor*. Depending on the size of the cut-off frequency, the new PR controller in (3.12) has approximately the same bandwidth compared to the ideal (3.11), but it enables the PR controller to track input values with higher precision. However, this newly introduced parameter limits the gain at $s = jh\omega_0$ to $G(s = jh\omega_0) = K_P + K_R$.

Tuning of the non-ideal PR controller in (3.12) are done in the below subsection *3.1.2 Tuning the PR Controller*. The tuning is done for any given PR controller, arbitrarily if it is either a circulating current or output current controller. Therefore, the resistance and inductance are not denoted by a specific identifier, such as arm or load. Proper tuning of the output current and circulating current controller is done in 3.2 and 3.3, respectively.

3.1.2 Tuning the PR Controller

TUNING THE PROPORTIONAL (P) GAIN

The PR controller is tuned according to the method shown in [13]. The proportional (P) gain of the PR-controller reacts, in contrast to the resonant gain, reacts on all of the system's transients. Therefore, K_P is tuned by decoupling the resonant gain. Using the plant in Figure 3.2 with negligible resistance and $K_R = 0$, the closed-loop transfer function yields

$$G_{cl}(s) = \frac{K_P}{sL + K_P} \qquad (3.13)$$

The first order system's cut-off frequency occurs at $s = K_P/L$, and hence the system's bandwidth yields

$$\alpha_c = \frac{K_P}{L} \qquad (3.14)$$

The convergence rate beyond the bandwidth becomes $\left|G_{cl}\left(K_P/L\right)\right| = 1/\sqrt{2}$. This rate is important as it explains how fast the input values converge beyond the system's bandwidth. Ideally, this parameter should be infinite small to mitigate the input value as quickly as possible.

MAXIMUM BANDWIDTH

The calculation of (3.13) and (3.14) is done without considering the time delay in the system. By considering a time delay in the system, the bandwidth α_c has an upper limit to ensure the system will remain stable with sufficiently large gains. As a rule of thumb, the system's bandwidth should be $\alpha_c \leq \omega_{sw}/10$ to remain stable [33]. The maximum bandwidth α_c can be calculated using *Bodes Stability Criteria* for the phase margin

$$\varphi_m = \pi + \angle\left\{G_{ol}\left(j\alpha_c\right)\right\} \tag{3.15}$$

where the open loop transfer function is $G_{ol}\left(s\right) = K_P/\left(sL\right)e^{-sT_d} = \left(\alpha_c\,e^{-sT_d}\right)/s$. In a typical PWM converter, the total time delay is considered to be 1.5 greater than the sampling time; $T_d = 1.5T_s$ [13]. The time delay is a function of the delay in the DSP's communication delay and PWM delay. Typically, the DPS's time delay is of the same order as the sampling time, while the PWM delay results in a half-cycle switch delay. The total time delay becomes $T_d = \underset{DSP}{T_s} + \underset{PWM}{0.5T_s}$.

Hence, the phase margin at the crossover frequency is derived to

$$\varphi_m = \pi + \left(-\frac{\pi}{2} + \underbrace{\tan^{-1}\left(\alpha_c\right)}_{\approx 0} - 1.5\alpha_c T_d\right) \tag{3.16}$$

As seen in (3.16), the inductor contributes with a phase delay of 90°, the proportional gain is considered a real integer and results thus in a 0 degrees phase angle, and the total time delay contributes to $-1.5\alpha_c T_d$. The resulting phase margin becomes

$$\varphi_m = \frac{\pi}{2} - 1.5\alpha_c T_d \tag{3.17}$$

Solving for the bandwidth yields the following expression for the system's bandwidth

$$\alpha_c = \frac{\pi/2 - \varphi_m}{1.5T_d} \tag{3.18}$$

The phase margin in (3.17) is calculated by applying the rule of thumb; $\alpha_c \leq \omega_s/10$ [33]. This results in a phase margin of $\varphi_m = \pi/5$, and consequently yields a maximum bandwidth of $\alpha_c = 4071.5$ with a switching frequency of $f_{sw} = 3240$ Hz. The switching frequency is calculated based on the number of submodules and carrier frequency of the PWM generator.

$$f_{sw} = N \cdot f_c \tag{3.19}$$

The sampling frequency is based on Nyquist's rule, and it says that the sampling time should be equal to half the switching time; $f_s = 2f_{sw}$.

When the maximum bandwidth is calculated, the proportional gain can be found using equation (3.14).

TUNING OF THE RESONANT (R) GAIN

The goal of this section is to maximise the resonant gain, K_R. It is necessary to optimise the gain to develop a controller that works with low-steady state error and with high bandwidth. Even though the tuning of the proportional gain was done without considering the resonant term's impact on the stability, K_P effects all system harmonics, and as a result tuning of the resonant gain must consider the proportional gain. The closed-loop transfer function for the PR-controller yields

$$G_{ol,PR}(s) = \frac{K_P\left(s^2 + \omega_c s + (h\omega_0)^2\right) + K_R s}{(sL + K_P)\left(s^2 + \omega_c s + (h\omega_0)^2\right) + K_R s} \tag{3.20}$$

It is assumed that ω_c is much smaller than $h\omega_0$; $\omega_c \ll h\omega_0$. Thus, the damping factor ω_c is neglected when tuning the converter in this section.

By analysing the dimensions of the resonant gain, the resonant gain consists of a squared angular frequency times the inductance. The following parametrisation for the resonant gain gives the correct dimension

$$K_R = 2\alpha_r \alpha_c L = 2\alpha_r K_P \tag{3.21}$$

where α_r is the resonant bandwidth that determines the convergence rate from the resonant part. By inserting the parametrisation in (3.21) into (3.20), the equation can be deducted to

$$G_{cl,PR}(s) = \frac{\alpha_c\left(s^2 + 2\alpha_r s + (h\omega_0)^2\right) + 2\alpha_r \alpha_c s}{(s + \alpha_c)\left(s^2 + 2\alpha_r s + (h\omega_0)^2\right) - 2\alpha_r s^2} \approx \frac{\alpha_c}{s + \alpha_c} \tag{3.22}$$

The simplified closed-loop transfer function in (3.22) is only valid provided that the resonant bandwidth is much smaller than the cross-frequency; $\alpha_r \ll \alpha_c$. Clearly, the conclusion of (3.22) is that, if the parametrisation used in (3.21) is used, the closed-loop dynamics of the ideal PR controller will be dominated around the cut-off frequency α_c.

To further determine the mathematical expression of the resonant gain, the procedure followed presented in [29] is followed. Firstly, the ideal PR transfer function is manipulated to one polynomial by introducing the time constant $\tau_R = K_P / K_R$.

$$G_{ol,PR} = K_P \left(1 + \frac{s}{\tau_R \left(s^2 + (h\omega_0)^2 \right)} \right) \tag{3.23}$$

The derivations in the abovementioned reference, which will also be shown in the below subsection, concludes that the resonant time constant can be expressed as follows

$$\tau_R = \frac{10}{\alpha_c} \tag{3.24}$$

By combining (3.24) and (3.21), the expression determining the resonant bandwidth is reduced to

$$\alpha_r = \frac{1}{2\tau_r} = \frac{\alpha_c}{20} \tag{3.25}$$

To summarise, equation (3.22) shows that the system's stability has the same cut-off frequency α_c when $\alpha_r \ll \alpha_c$. Therefore, the conclusion of α_r does not impact the stability of the system. Hence, mitigating several harmonics using several resonant controllers can be done without interfering with the system's stability.

3.1.3   Ideal vs Non-Ideal PR Controller

This subsection is going to compare the Bode Plots of an ideal and a non-ideal PR controller. Therefore, the non-ideal PR controller is tested with several different resonant dampers to check which value would reproduce the most accurate result.
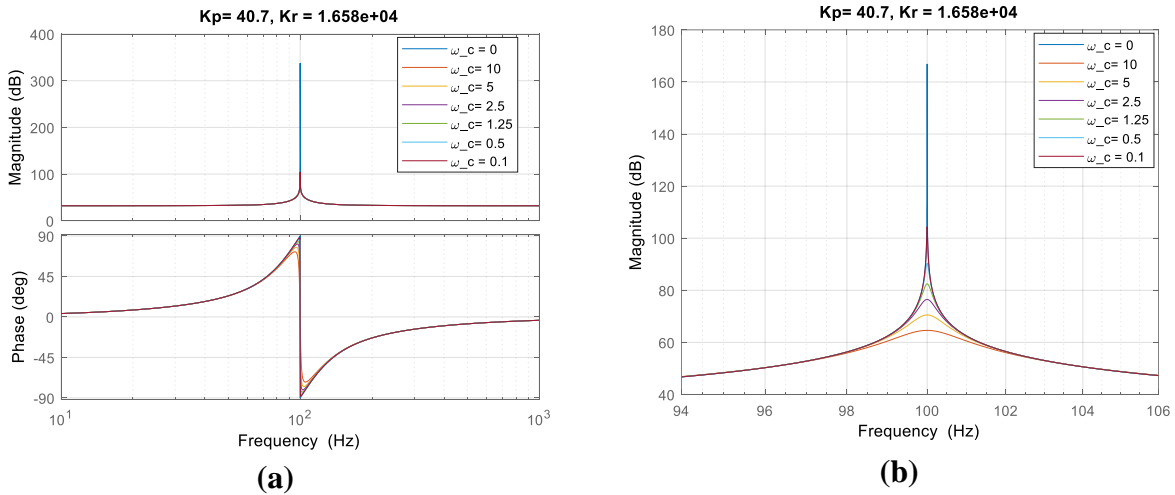
Figure 3.3 Bode plots of the non-ideal PR controller with variable ω_c.

Figure 3.3 shows that a lower damping factor ω_c results in similar behaviour to the ideal PR controller. The use of $\omega_c = 0.1$ has qualities very close the actual ideal PR controller, and it gives a sufficiently high gain. To further investigate the non-ideal PR controller, the transfer function is discretised using the Tustin's pre-warped frequency approximation. A proper explanation of

Tustin's pre-warped frequency approximation is shown in section 3.5. Bode plot of the ideal and non-ideal discretised PR controller is shown in Figure 3.4.

(a)

(b)

(c)
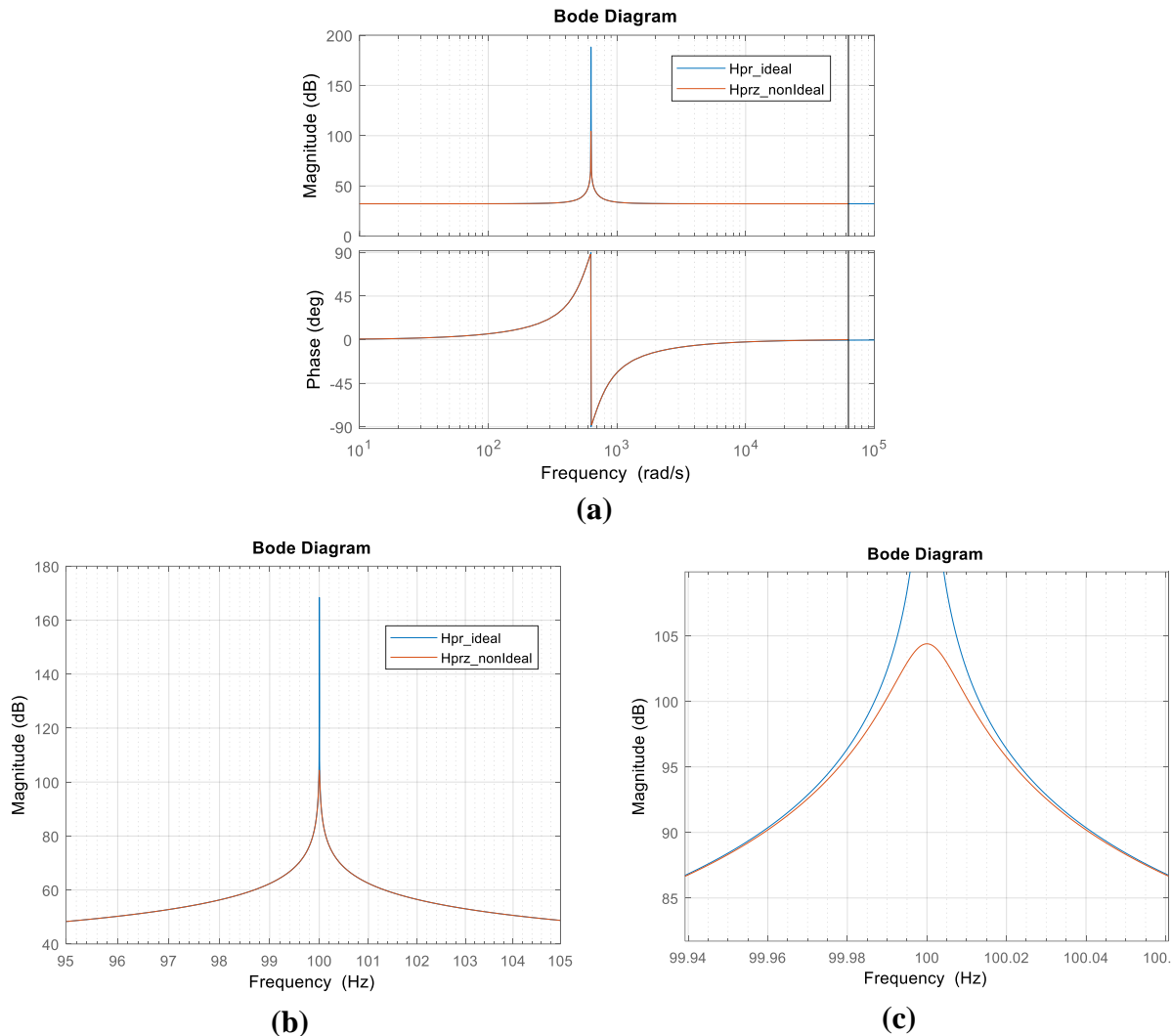
Figure 3.4 Bode plots of the continuous ideal PR controller in blue and discretised non-ideal PR controller in red. **(a)** shows the overview, while **(b)** and **(c)** show the same Bode plot just with zoom.

In Figure 3.4 (a) the Nyquist frequency, which marks the minimum rate at which a signal can be sampled without errors, is marked by the vertical line. Both (b) and (c) show the accuracy of the pre-warped frequency and DFIIt transformation. At 99.95 Hz, the error between the ideal and non-ideal discretised PR controller was measured to less than 0.1 %. The error diminishes as the frequency deviates more from the resonant peak, and the characteristic behaviour of the non-ideal PR controller and the ideal PR controller narrows down to the same behaviour. Therefore, the conclusion of further use of ω_c =0.1 is acceptable.

3.2   Tuning of the Output Current Control

The purpose of the output current control is to ensure a sinusoidal output current with minimum distortion. As the output current, i_s, is a sinusoid with fundamental frequency, the utilisation of a PR controller is used to control the current.

$$V_s(t) \qquad R_{arm}/2 + R_{grid} \qquad L_{arm}/2 + L_{grid} \qquad V_a(t)$$

$$I_s(t)$$
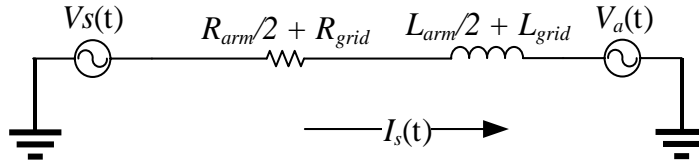
Figure 3.5 Equivalent single line diagram of the output current controller.

Laplace transformation of equation (2.20) yields the plant transfer function of the model shown in Figure 3.5

$$i_s(s) = \frac{2}{sL + R}(v_s - v_a) \tag{3.26}$$

Clearly, the output current is driven by the voltage and the angle difference between the output and grid voltage, $v_s\text{-}v_a$. Ideally, and in most cases, the grid voltage is sinusoidal with a constant fundamental frequency. However, some events may change the grid frequency, e.g. short-circuit faults, sudden load connections or load outages, sags, and angle jumps. These events can cause the output voltage reference, v_s^*, to exceed its nominal value, and consequently distort the output current. Therefore, the grid voltage must be feed-forwarded to the controller in order to compensate for undesired situations. In addition, a resonant bandpass filter should be added to avoid high-frequency transients into the control system.

As mentioned in section 2.2.3, the output reference voltage, v_s^*, is used to calculate the insertion indices. However, as mentioned in the above paragraph, the output voltage may exceed its limit due to frequency fluctuations. Having a too high output reference fed to the insertion indices may cause overmodulation in the PWM-modulator. Hence, to ensure proper gate signals to the PWM, it is desired to have a saturation block to ensure correct calculation of the insertion indices. However, inserting a saturation block introduces non-linearity in the system. This phenomenon is called windup of the resonant part as the non-linearity causes the error to accumulate in the unsaturated operation. A method called *back calculation* can be used to prevent windup of the R-part [34]. As the name suggests, the modified error is obtained by subtracting the reference output voltage with the voltage reference after the saturation block. The modified error becomes

$$e' = e + \frac{1}{K_P}\left(v_s^* - v_s^{*0}\right) \tag{3.27}$$

The modified error, e', is fed back to the resonant part.

A block diagram of the output current controller is shown in the below figure.
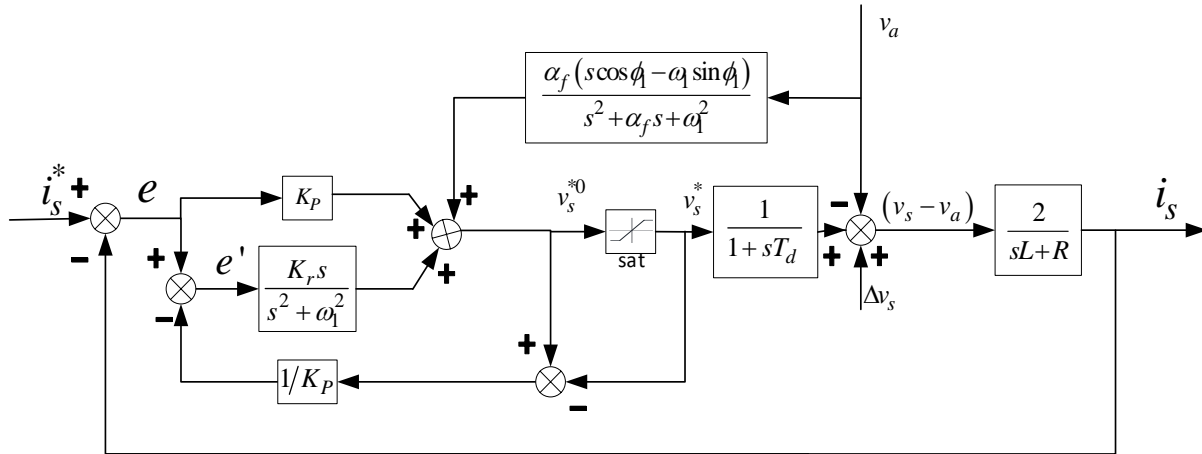
Figure 3.6 Block representation of the output current controller [13].

The tuning of control parameters K_P and K_R in Figure 3.6 is done according to the method shown in section 3.1.2.

$$\alpha_c = 4,071.5 \qquad \alpha_R = 203.58$$
$$K_P = 24.43 \qquad K_R = 9,946.3 \tag{3.28}$$

The simulation model is realised in Simulink and shown in Appendix A - Matlab and Simulink Model.

3.3 Circulating Current Control

3.3.1 Tuning of the Circulating Current Suppressing Controller

As mentioned in Chapter 2, one of the most concerning problems in the MMC was the circulating current as it could trigger unsuccessful operation of the converter and contribute to higher ohmic losses. Some of the unwanted properties of the MMC without circulating current controller is the high risk of resonances inside the converter. The resonances are caused by the MMC's resonant circuit consisting of the arm inductances and the variable inserted number of capacitors. Therefore, having an uncontrolled circulating current could trigger these if operating at the resonance frequencies. Therefore, the thought of having an uncontrolled current inside the converter is very frightening as it could trigger unsuccessful operation. With the use of a circulating controller, this variable circulating current can be used as an additional degree of freedom when designing the control system. For example, it can be used to balance the MMC's average arm energies.
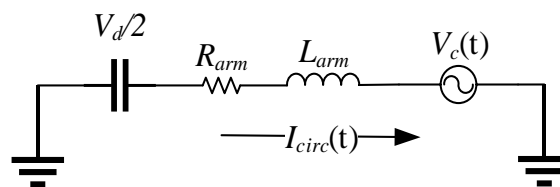
Figure 3.7 Equivalent single line diagram of the one-phase circulating current.

To properly tune the controller as shown in Figure 3.7, let's remember the equation and corresponding transfer function governing the circulating current given by (2.21)

$$L\frac{di_{circ}}{dt} = \frac{v_d}{2} - \underbrace{\frac{n_u v_{cu}^{\Sigma} + n_l v_{cl}^{\Sigma}}{2}}_{v_c} - Ri_{circ} \tag{3.29}$$

$$\omega_{rn} = \sqrt{\frac{N}{LC}}\sqrt{\frac{2\left(n^2-1\right)+\hat{m}n^2}{4n^2\left(n^2-1\right)}}, n = 3k \pm 1 \tag{3.30}$$

Clearly, the circulating current is a non-linear component as the variable intern voltage actively changes the derivative of the circulating current. In fact, the circulating current predominantly consists of a 2nd order transient component, but also of multiples of other multiple harmonics such as the 4th, 7th etc [35]. To further analyse the circulating current, equation (2.29) is repeated in equation (3.31).

$$\frac{dW_{\Sigma}}{dt} = V_d I_c - \frac{\hat{V}_s \hat{I}_s}{2}\cos\varphi - \frac{\hat{V}_s \hat{I}_s}{2}\cos\left(2\omega_0 t - \varphi\right) \tag{3.31}$$

In equation (3.31), the first term is responsible for the power transfer between dc-side to the internal capacitors of the MMC. The last term shows how a parasitic cosine component containing the second order harmonic contributes with a mean power transfer of zero. In other words, the last term acts as a disturbance to the power transfer inside the converter. As energy is transferred from the dc-side, it is expected that the circulating current will carry a component of the same second order. Hence, an expression for the circulating current becomes

$$i_{circ}\left(t\right) = I_{circ,0} + \hat{I}_{circ}\sin\left(2\omega_0 t + \phi_{circ}\right) \tag{3.32}$$

As governed by the energy equation in (3.31), the circulating current must contain a dc-component to transfer energy to its capacitors. The ac component, in opposition to the dc, does not bring any benefit to the converter. It contributes with a mean power of zero, gives higher ohmic losses, increases the rating of the converter components as the peak current flowing inside the converter becomes higher, and to avoid any resonance frequencies inside the converter. Consequently, it is desired to suppress the circulating current converter. Therefore, to accurately track this current the utilisation of the PR controller must be done- as was the conclusion of section 3.1.1. The realisation of an ideal PR controller targeting the 2nd order harmonic should be implemented, and the ideal PR transfer function becomes

$$G_{PR,ideal}\left(s\right) = K_P + \frac{K_r s}{s^2 + \left(2\omega_0\right)^2} \tag{3.33}$$

Figure 3.8 shows a block representation of the PR controller and the plant
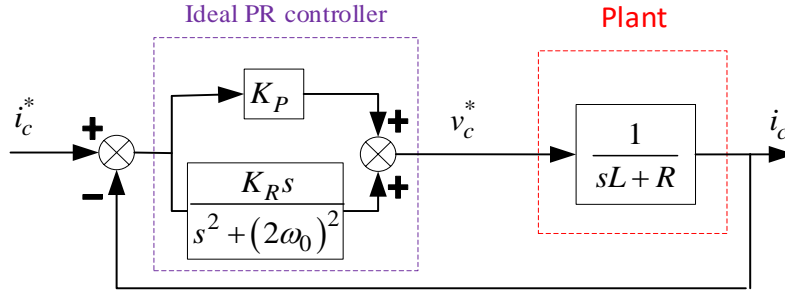
Figure 3.8 Block representation of the ideal PR controller.

Tuning of (3.33) is done according to the derivation shown in section 3.1.1. Thus, the following parameter selection

$$\alpha_c = \frac{\omega_s}{10} = 4071.50 \qquad \alpha_R = \frac{\alpha_c}{20} = 203.58$$

$$K_P = \alpha_c L_{arm} = 40.72 \qquad K_R = 2\alpha_R K_P = 16577.15 \qquad (3.34)$$

$$\varphi_m = \pi/2 - 1.5\alpha_c T_d = 36°$$

To further suppress harmonic components inside the converter, resonant filters can be added in parallel to the resonant gain of the PR controller [36].
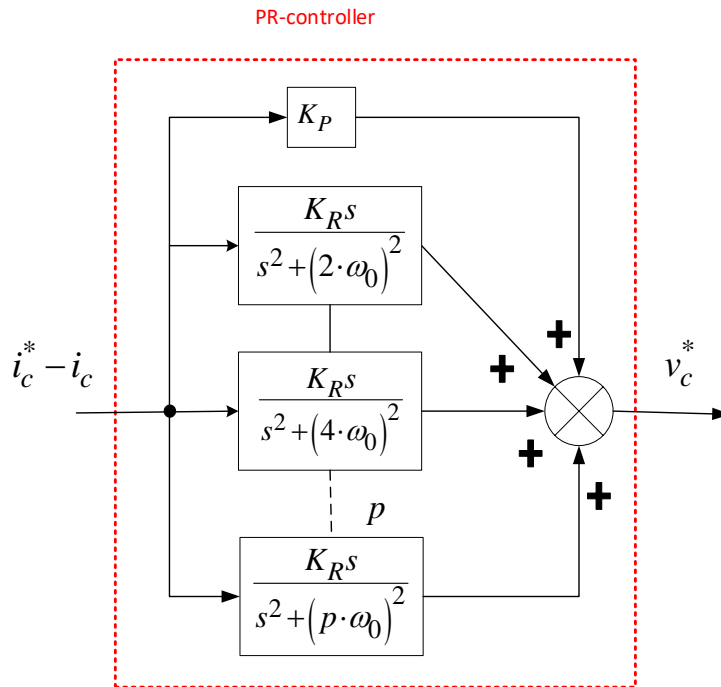
Figure 3.9 PR controller with harmonic compensator similar to the one used in [36].

The harmonics to be suppressed are based on the equation governing the resonant frequencies inside the converter. The equation for determining the resonant frequencies was found in (3.35)

$$\omega_{rn} = \sqrt{\frac{N}{LC}} \sqrt{\frac{2\left(n^2 - 1\right) + \hat{m}n^2}{4n^2\left(n^2 - 1\right)}}, n = 3k \pm 1 \tag{3.35}$$

According to (3.35), the harmonic filters in Figure 3.9 are not always necessary to operate the MMC safely. Proper parameter design can also avoid the resonant frequencies. If it is impossible to avoid the resonant frequencies, the following two methods of suppressing the currents can be used. First, pre-tuned harmonic filters can be used to suppress harmonics[36]. Second, repetitive control can be used to suppress multi-frequency harmonics in a system effectively [37].

Oscillating harmonic distortion inside the MMC contributes to higher peak currents, and consequently higher resistive losses and a higher rating of the power electronics. By minimising the total harmonic distortion, the lower losses are the losses. The total harmonic distortion in a sinusoidal current is calculating by the following formula

$$\mathrm{THD} = \frac{\sqrt{I_2^2 + I_3^2 + I_4^2 + \dots + I_n^2}}{I_1} \tag{3.36}$$

where the subscript indicates the harmonic number.

3.3.2   Simulation Results

This section illustrates the effectiveness of the circulating current controller. The model simulation is a direct-voltage control with no arm energy balancer. The peak-to-peak circulating current in Figure 3.10 was cropped in the figure to get a clear picture of steady-state, but the maximum and minimum value was measured to 62.14A and -42.26A, respectively.
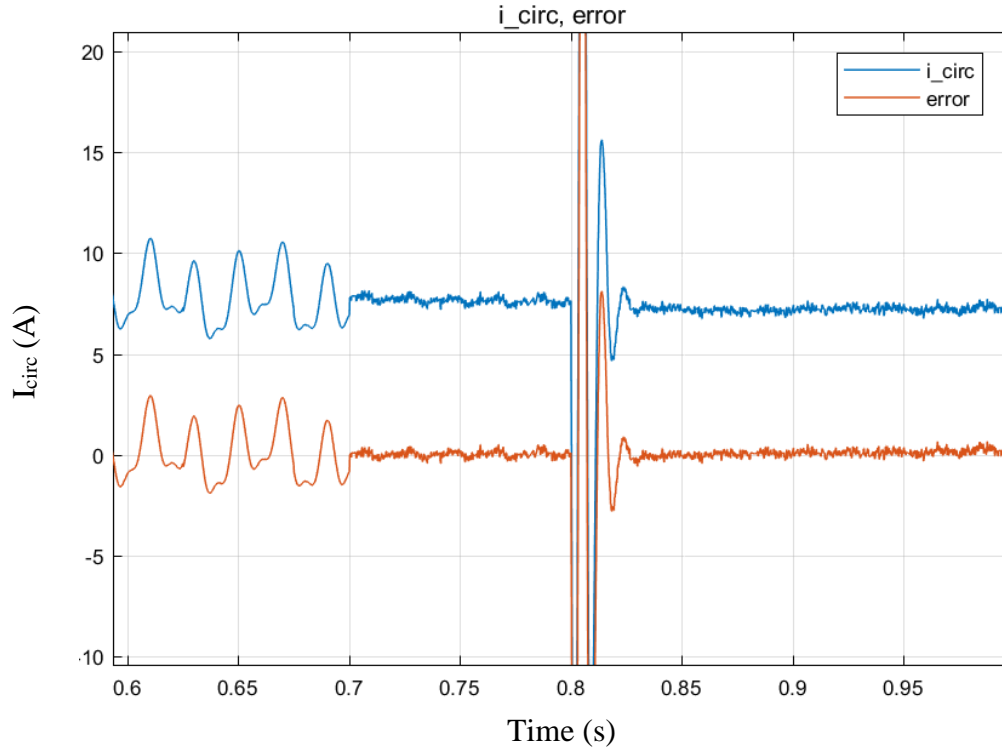
Figure 3.10 Circulating current and coherent error with activation of K_P and K_R at t=0.7 and t=0.8, respectively.

The numerical results from the simulation in Figure 3.9 are shown in Table 3.1.

Table 3.1 Numerical results with and without circulating current controller

| | | \multicolumn{4}{c}{$0.7 < t < 0.8$} | \multicolumn{4}{c}{$0.9 < t < 1.0$} |
| Time of activation (s) | | \multicolumn{4}{c}{FFT (%$_{mag}$ relative to 50Hz)} | \multicolumn{4}{c}{FFT (%$_{mag}$ relative to 50Hz)} |
K_P	K_R	I_{rms} (A)	Error (%)	DC	100 Hz	I_{rms} (A)	Error (%)	DC	100 Hz
-	-	7.93	16.63	482.1	40.2	7.92	16.41	479.3	39.6
0.7	0.8	7.66	2.06	5947.7	55.4	7.23	2.66	8534.2	3.91

Interestingly, activation of the resonant filter at t=1.0 increases the error of circulating current. The bandwidth of the proportional gain manages to suppress most of the transients in the simulated system effectively. Hence, the introduction of the R-part acts as a disturbance to the system. Though, it is noted that the resonant controller suppresses the 100Hz component from 55.4 % to 3.91 % compared to the fundamental frequency of 50 Hz. It is also seen that the 50 Hz component in the circulating current is significantly high. This must be seen in correlation with the derivate of the power transfer between the arms, governed by equation (2.30), which is naturally governed by a 50Hz. It is believed that a closed-loop voltage control system with arm energy balancer will remove the 50Hz from the circulating current. This will be shown in section 3.4.

3.4   Arm Energy Loop Control

3.4.1   Circulating Current – A Flexible Tool

As concluded in the above section, the need for arm-energy loop controller is needed to suppress the fundamental frequency responsible for energy transfer between the upper and lower arm. The energy-contributing current flowing between the two arms is undesired as it contributes to higher internal resistive losses. Thus, it is desired to control the mean values of W_Σ and W_Δ to their initial values; $W_{\Sigma 0}$ and 0. This ensures no energy transfer between the arms, which would inevitably consist of the fundamental frequency. This phenomenon was mathematically derived in section 2.2.2, and the equations describing the energy transfer is repeated in (3.37) and (3.38)

$$\frac{dW_\Sigma}{dt} = 2v_c^* i_c - v_s^* i_s = \left(v_d - 2v_c\right) i_{circ} - v_s i_s$$

$$\Rightarrow W_\Sigma = \underbrace{\frac{Cv_d^2}{N}}_{W_{\Sigma 0}} - \underbrace{\frac{\hat{V}_s \hat{I}_s}{4\omega_0} \sin\left(2\omega_0 t - \varphi\right)}_{\Delta W_\Sigma}$$

(3.37)

$$\frac{dW_\Delta}{dt} = v_c^* i_s - 2v_s^* i_{circ} = -2v_s i_{circ} + \left(v_d/2 - v_c\right) i_s$$

$$\Rightarrow W_\Delta = \underbrace{W_{\Delta 0}}_{\approx 0} + \underbrace{\frac{v_d \hat{I}_s}{2\omega_0} \sin\left(\omega_0 t - \varphi\right) - \frac{2\hat{V}_s i_{circ}}{\omega_0} \sin\left(\omega_0 t\right)}_{\Delta W_\Delta}$$

(3.38)

Equation (3.37) shows that the circulating current plays a significant role when controlling the sum of energy controllers. The required power needed for the ac-side and internal resistive losses is found by multiplying the dc-component of the circulating current with the dc-link voltage. The power from the dc-link is proportional to the circulating current, and hence the increased power from the dc-link is used to increase the submodules' voltages. However, this power does not impact the energy balance of the submodules as long as there are no dc-components in the output current and voltage.

Balancing the submodule voltages are done using the delta-energy controller. Equation (3.38), governing the internal energy transfer, shows that the circulating current must be in phase with the output voltage to balance the submodules. If the circulating current is in phase with the output voltage, a dc-component will be present in the $v_s \cdot i_{circ}$ expression. The dc-component increases the amplitude of the ac signal in the corresponding two arms and therefore forcing the energy level to change. Use of a PLL at the output ac-voltage terminal can be used to synchronise the circulating current with the output voltage, and hence the submodule voltages converge to the same voltage level.

Equation (3.38) shows the rate of energy transfer in the capacitors, and the derivative term in equation (2.21) may be regulated to zero with proper circulating current control. Thus, adding an

increment in the circulating current reference signal to suppress the energy ramp caused by the integration is desired. The increment, as proposed in [13], yields

$$\Delta i_c^* = K_\Sigma \left(W_{\Sigma 0} - \mathrm{LPF}(W_\Sigma) \right) - K_\Delta \mathrm{LPF}(W_\Delta) \cos(\omega_0 t) \tag{3.39}$$

where two P-controllers are used to regulate the circulating current to suppress the energy transfer between the arms.

The lowpass-filter is needed to suppress the arm-energy ripples caused by the energy transfer, and the bandwidth should be lower than the fundamental frequency carrying the energy between the arms. Presence of the term $\cos(\omega_0 t)$ is needed to counteract the energy unbalance between the two terms, and the circulating current carrying this energy should be in synchronisation with the output current v_s, and hence should be fed from a phase-locked loop. The two gains proportional gains K_Σ and K_Δ determine the convergence rate of the energy-arm controller. Therefore, accurate tuning of the proportional gains is not investigated in this thesis. Illustration of (3.39) is done in Figure 3.11.
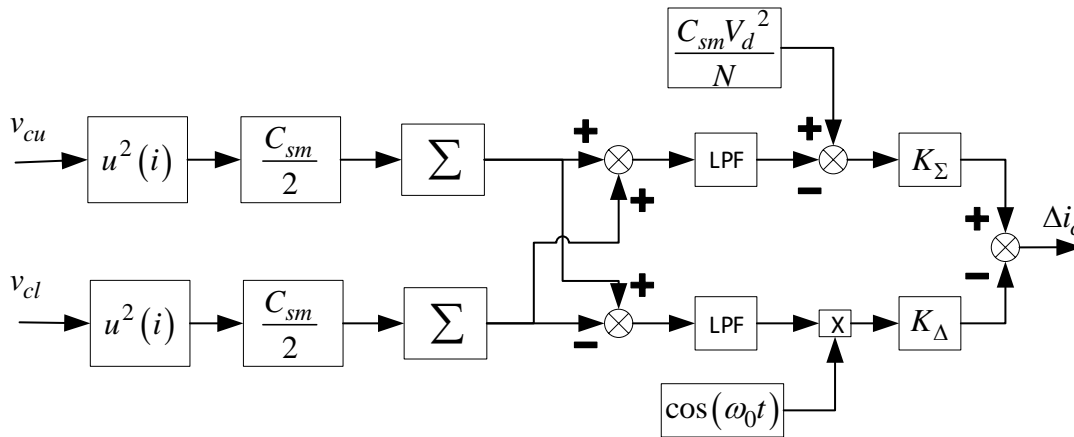
Figure 3.11 Schematic diagram of the arm-energy controller.

The problems associated with this technique is the required measurements of all the submodule capacitors, and this ensures feed-back delay [38]. In an MMC with hundreds of submodules, the resulting feedback delay may cause the phase lag in the measured components, and hence misplace the compensation. This results in an unstable converter with high losses. One method to solve this issue is the proposal of the open-loop voltage control [39]. The open-loop voltage control method does not require measurements of the submodule voltages as it is estimating the capacitor voltage ripples to create the gate pulses. The method is much more elegant is it lowers the computational power as well as achieving excellent numerical results. However, this method will not be more investigated in this thesis as it is more complex and is not the scope of this thesis. The closed-loop voltage control works as supposed in the simulated system.

3.4.2   Simulation Results

Figure 3.11 shows that the arm energy controller consists of two separate controllers; the sum energy controller and the delta energy controller. To illustrate their working principles and effect on the submodules capacitor voltages, the energy sum and energy change is activated at t=0.4 and t=0.6, respectively.
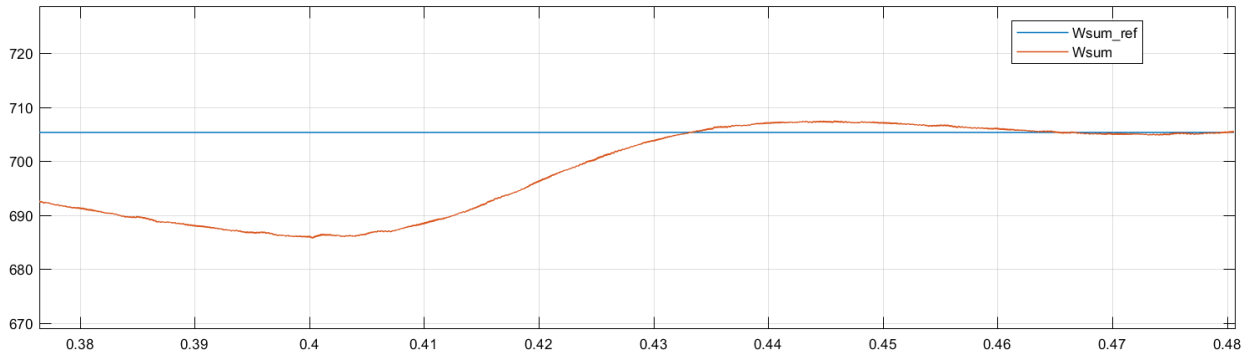
Figure 3.12 Activation of the sum energy controller at t=0.4 Y-axis and x-axis show the energy in joule and time in seconds, respectively. The reference value is shown in blue, and the submodules' measured energy is shown in red.
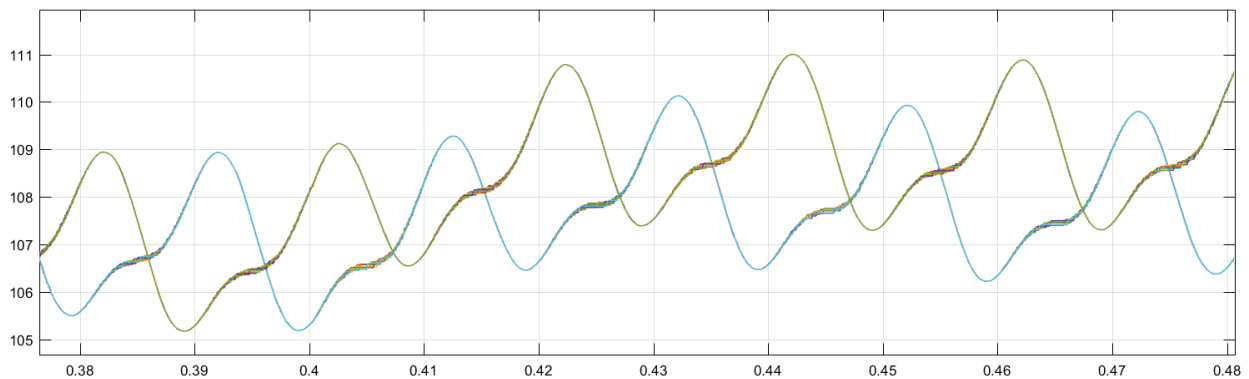
Figure 3.13 Submodule capacitor voltages in the upper arm (green) and lower arm (blue) as the sum energy controller is activated at t=0.4s.

Figure 3.12 and Figure 3.13 show the resulting capacitor voltage levels when the energy sum controller is activated. At activation, the sum energy in the capacitors jumps to the reference value due to the injected charging current into the circulating reference current. Resultingly, the capacitor voltages charge up to the sum energy reference value. However, the sum energy controller is not able to ensure equal voltage between the upper and lower submodules as it is only focusing on the mean sum energy sum of the upper and lower arm together. Consequently, the delta energy controller is needed to balance the upper and lower submodule arm voltages to the same voltage level. By doing so, the current transferring energy with the fundamental frequency is suppressed.
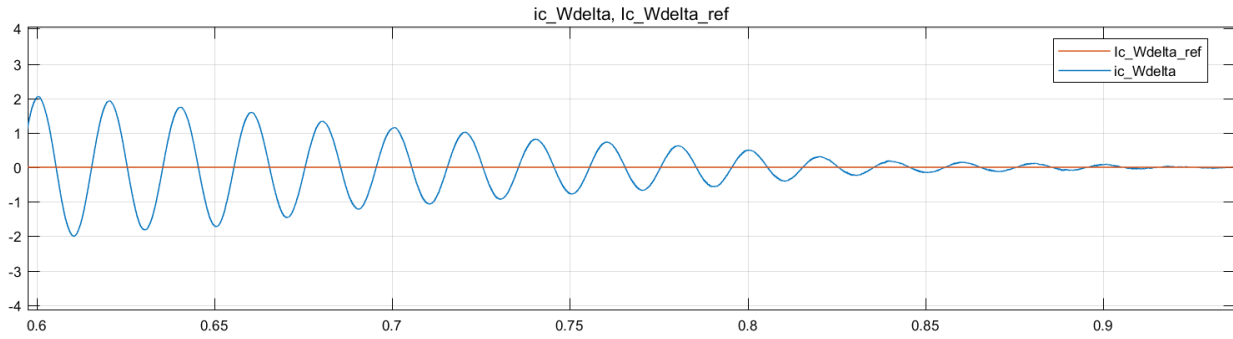
Figure 3.14 The delta energy current, in blue, converges to the reference value of zero in red. Y-axis shows the energy in J and the x-axis shows the time in seconds.

(a)   **(b)**
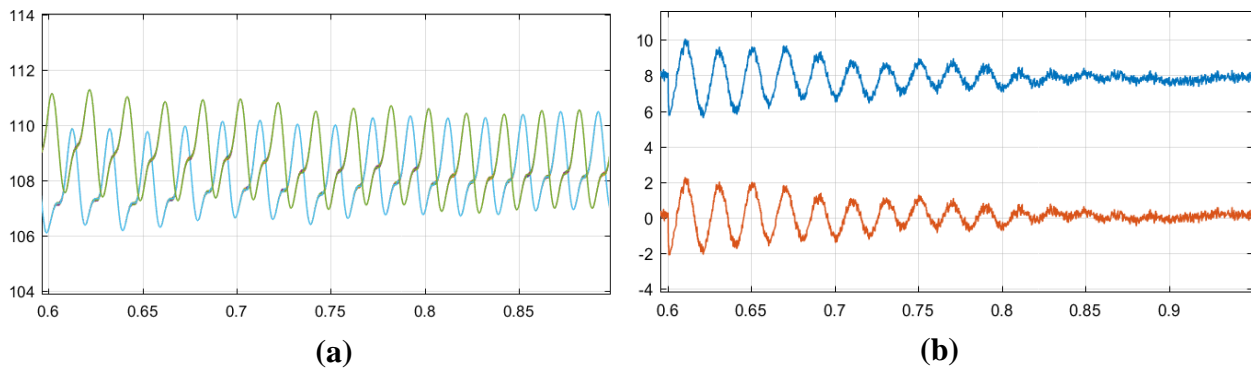
Figure 3.15 Energy change controller activated at t=0.6s. In **(a)** the submodule voltages balances, and in **(b)** the circulating current and error are shown in blue and red respectively.

The delta energy controller is activated at t=0.6, and simultaneously an energy balancer current as shown in Figure 3.14. The energy balancer current is injected into the circulating current, as seen in Figure 3.15 (b), to even the voltages between the upper and lower arm. As seen in Figure 3.15 (a) the average submodule capacitor voltages converge towards the mean value of V_d/N which equals to 108.42 V.

Choosing a more aggressive value of K_Σ and K_Δ gives a faster responding energy control system.

3.5 Discrete-Time Realisation – Tustin's Pre-warped Approximation

Microcontrollers operate within the discrete time domain, and to physically implement a PR controller a transformation from the continuous time domain to the discrete must be done. A well-known method to discretise the R part from the continuous time domain to the discrete is the *Tustin Approximation* [2]. The drawback of using the Tustin approximation is that the continuous time domain is compressed into the finite frequency range from 0 to 1 in discrete form. Consequently, the non-linear transformation causes the phase and frequency transformation to no longer match the corresponding frequency in *s*-domain. Therefore, the Tustin approximation with pre-warping around the desired resonant frequency can be done. This method is much more accurate around the desired frequency. The approximation of *s* in the discrete domain becomes

$$s = \frac{\omega}{\tan\left(\dfrac{\omega T}{2}\right)} \frac{z-1}{z+1} \tag{3.40}$$

where ω is the pre-warping frequency, and T is the sampling period based on the numerical integration step used in the trapezoidal rule. In the circulating current controller, the pre-warping frequency can be set to the resonant frequency to be suppressed, and thus the following parametrisation $\omega = h\omega_0$ is valid.

3.5.1 Discrete Z-domain

Implementation of the PR controller is done in the discrete time domain because DSPs and FPGAs calculate with discrete values. Representation of the PR controller is therefore done through the use of an IIR-filter, which has the structure as shown in (3.41).

$$H_{PR}(z) = \frac{b_0 + b_1 z^{-1} + b_2 z^{-2}}{1 + a_1 z^{-1} + a_2 z^{-2}} \tag{3.41}$$

Derivation of the parameters b_0, b_1, b_2, a_1 and a_2 is tedious but essential to get a clear understanding of the parameters' dynamics. First, derivation of a_1 and a_2 is found by discretising the resonant controller. Second, b_0, b_1 and b_2 were found by adding the proportional part to the resonant part; P+R.

DISCRETISE R-PART: FINDING A_1 AND A_2

Equation (3.42) shows the continuous transfer function of the non-ideal resonant controller.

$$H_R(s) = K_R \frac{s}{s^2 + \omega_c s + (h\omega_0)^2} \tag{3.42}$$

Discretising of (3.42) is done using the Tustin's pre-warped approximation as shown in (3.40). To ease the calculations, ignored ignoring K_R until the final equation, and the following simplifications are done

$$h\omega_0 = \omega_1$$

$$\frac{h\omega_0 T_s}{2} = \gamma \qquad (3.43)$$

$$\tan(x) = \frac{\sin(x)}{\cos(x)}$$

Using the simplifications in (3.43), Tustin's pre-warped approximation in (3.40) yields

$$s = \frac{\omega_1 \cos \gamma}{\sin \gamma} \frac{z-1}{z+1} \qquad (3.44)$$

Using the simplifications in (3.43) and substituting s with the approximation in (3.44) into (3.42) yields

$$H_R(z) = \frac{\dfrac{\omega_1 \cos \gamma}{\sin \gamma} \dfrac{z-1}{z+1}}{\dfrac{\omega_1^2 \cos^2 \gamma}{\sin^2 \gamma} \dfrac{(z-1)^2}{(z+1)^2} + \dfrac{\omega_1 \cos \gamma}{\sin \gamma} \dfrac{z-1}{z+1} + \omega_1^2} \qquad (3.45)$$

$$H_R(z) = \frac{\omega_1 \cos \gamma \sin \gamma (z+1)(z-1)}{\omega_1^2 \cos^2 \gamma (z-1)^2 + \omega_c \omega_1 \cos \gamma \sin \gamma (z^2-1) + \omega_1^2 \sin^2 \gamma (z+1)^2} \qquad (3.46)$$

$$H_R(z) = \frac{\omega_1 \cos \gamma \sin \gamma (z^2-1)}{\omega_1^2 \cos^2 \gamma (z^2-2z+1) + \omega_c \omega_1 \cos \gamma \sin \gamma (z^2-1) + \omega_1^2 \sin^2 \gamma (z^2+2z+1)} \qquad (3.47)$$

Equation (3.47) is simplified to $H_R(z) = Num(z)/Den(z)$ due to equation length. $Num(z)$ and $Den(z)$ are derived to

$$Num(z) = \omega_1 \cos \gamma \sin(\gamma)(z^2-1) \qquad (3.48)$$

$$\begin{aligned} Den(z) = &\left(\omega_1^2 \sin^2 \gamma + \omega_1^2 \cos^2 \gamma + \omega_c \omega_1 \cos \gamma \sin \gamma\right) z^2 + \\ &\left(2\omega_1^2 \sin^2 \gamma - 2\omega_1^2 \cos^2 \gamma\right) z^1 + \\ &\left(\omega_1^2 \sin^2 \gamma + \omega_1^2 \cos^2 \gamma - \omega_c \omega_1 \cos \gamma \sin \gamma\right) \end{aligned} \qquad (3.49)$$

To further simplify (3.48) and (3.49), the following trigonometric identities were used.

$$\sin(2x) = 2\sin(x)\cos(x) \qquad (3.50)$$

$$1 = \sin^2 x + \cos^2 x \tag{3.51}$$

$$\sin^2 x - \cos^2 x = -\cos(2x) \tag{3.52}$$

Inserting (3.50)-(3.52) into (3.48) and (3.49) results in

$$H_R(z) = \frac{1/2\,\omega_1 \sin(2\gamma)\left(z^2 - 1\right)}{\left(\omega_1^2 + 1/2\,\omega_c\omega_1 \sin(2\gamma)\right)z^2 - 2\omega_1^2 \cos(2x) + \left(\omega_1^2 - 1/2\,\omega_c\omega_1 \sin(2\gamma)\right)} \tag{3.53}$$

To get the desired transfer function where $a_0 = 1$, all terms of (3.53) must be divided by z^2 and $\left(\omega_1^2 + 1/2\,\omega_c\omega_1 \sin(2\gamma)\right)$

$$H_R(z) = \frac{\sin(\omega_1 T_s)}{2\left(h\omega_0 + 1/2\,\omega_c \sin(h\omega_0 T_s)\right)} \cdot$$

$$\left(\frac{1 - z^{-2}}{1 - \dfrac{2\omega_1 \cos(\omega_1 T_s)}{\omega_1 + 1/2\,\omega_c \sin(\omega_1 T_s)}z^{-1} + \dfrac{\omega_1 - 1/2\,\omega_c \sin(\omega_1 T_s)}{\omega_1 + 1/2\,\omega_c \sin(\omega_1 T_s)}z^{-2}}\right) \tag{3.54}$$

Finally, multiplying by the resonant gain K_R and substituting the parameters in (3.43) into (3.54) yields the final discrete transfer function

$$H_R(z) = \frac{a\left(1 - z^{-2}\right)}{1 + a_1 z^{-1} + a_2 z^{-2}} \tag{3.55}$$

where

$$a = \frac{K_R \sin(h\omega_0 T_s)}{2\left(h\omega_0 + 1/2\,\omega_c \sin(h\omega_0 T_s)\right)} \tag{3.56}$$

$$a_1 = -\frac{2h\omega_0 \cos(h\omega_0 T_s)}{h\omega_0 + 1/2\,\omega_c \sin(h\omega_0 T_s)} \tag{3.57}$$

$$a_2 = \frac{h\omega_0 - 1/2\,\omega_c \sin(h\omega_0 T_s)}{h\omega_0 + 1/2\,\omega_c \sin(h\omega_0 T_s)} \tag{3.58}$$

FINDING B_0, B_1 AND B_2

Now, as the parameters of the resonant transfer function have been found, the idea is to find the resulting b_0, b_1 and b_2 which is found by adding the proportional part to the resonant part; $H_{PR}(z) = K_P + H_R(z)$. This subsection shows the derivation of finding b_0, b_1 and b_2. The non-ideal PR transfer function in the continuous time domain is shown in (3.59)

$$H_{PR}(s) = K_P + K_R \frac{s}{s^2 + \omega_c s + (h\omega_0)^2} \tag{3.59}$$

In the discrete time domain this yields

$$H_{PR}(z) = K_P + \frac{a(1 - z^{-2})}{1 + a_1 z^{-1} + a_2 z^{-2}} \tag{3.60}$$

$$H_{PR}(z) = \frac{(K_P + a) + (K_P a_1) z^{-1} + (K_P a_2 - a) z^{-2}}{1 + a_1 z^{-1} + a_2 z^{-2}} \tag{3.61}$$

Clearly, the equation (3.61) has the same structure as the IIR-filter. Therefore, the parameters b_0, b_1 and b_2 is found.

$$H_{PR}(z) = \frac{b_0 + b_1 z^{-1} + b_2 z^{-2}}{1 + a_1 z^{-1} + a_2 z^{-2}} \tag{3.62}$$

where

$$b_0 = K_p + a = K_p + \frac{K_R \sin(h\omega_0 T_s)}{2(h\omega_0 + 1/2\,\omega_c \sin(h\omega_0 T_s))} \tag{3.63}$$

$$b_1 = K_P a_1 = -\frac{2K_P h\omega_0 \cos(h\omega_0 T_s)}{h\omega_0 + 1/2\,\omega_c \sin(h\omega_0 T_s)} \tag{3.64}$$

$$b_2 = K_P a_2 - a = K_p \left(\frac{h\omega_0 - 1/2\,\omega_c \sin(h\omega_0 T_s)}{h\omega_0 + 1/2\,\omega_c \sin(h\omega_0 T_s)} \right) - \frac{K_R \sin(h\omega_0 T_s)}{2(h\omega_0 + 1/2\,\omega_c \sin(h\omega_0 T_s))} \tag{3.65}$$

The parameters a_1, a_2, b_0, b_1 and b_2 derived in this section yields the exact numerical values used for the non-ideal PR controller. The parameters of the non-ideal PR controller are very similar to the ones of the ideal PR controller, which is achieved by inserting $\omega_c = 0$ in the final equations (3.57), (3.58) and (3.63)-(3.65). One term which shows repeatedly is $h\omega_0 \pm 1/2\omega_c\sin(h\omega_0 T_s)$, and analysis shows it is approximately equal to $h\omega_0$. As T_s is usually in the range of microseconds, the discretising sampling time is $T_s \ll h\omega_0$. Hence, the expression $\sin(h\omega_0 T_s) \approx h\omega_0 T_s$. Further, the term $1/2h\omega_c\omega_0 T_s$ becomes even smaller as $1/2\omega_c \ll 1$. In comparison to $h\omega_0$, the term $1/2\omega_c\sin(h\omega_0 T_s)$

can be neglected. Consequently, the term $h\omega_0 \pm 1/2\omega_c \sin(h\omega_0 T_s)$ can be approximated to $h\omega_0$, and hence the parameters become the same as in the ideal PR controller where $\omega_c = 0$.

It is important to remember that the above approximations of the non-ideal to the ideal PR controller will give errors if used in simulations. Figure 3.4 confirms this, as the resonant gain for the non-ideal controller is much lower than the ideal controller, but shortly outside the resonant peak the non-ideal and ideal controller coincides with the same resonant gain. Though, for analytical purposes, such as investigating the dynamic behaviour under frequency deviations, the approximation can be performed to ease the mathematical expression significantly. The above approximations are used when investigating the adaptive qualities of the discretised PR filter in section 4.3.

3.5.2 Delta (δ) Operator

For fixed-point digital implementation, the resonant controller struggles to realise an efficient control at high frequencies beyond the resonant frequency. This is mainly due to the long word length needed to operate with high accuracy, which results in long bit operations [2]. Word length refers to the number of bits which a microcontroller can process in one instant. A low word length algorithm allows for faster operation and a microprocessor with lower computational power. The δ-operator is introduced to give better numerical properties as the word length can be reduced. One approximation of the δ-operator using the *direct form II transposed* (DFIIt) yields excellent numerical properties [40]. The δ-operator yields

$$\delta = \frac{z-1}{\Delta} \tag{3.66}$$

where Δ is an optimisation parameter with a value of $\Delta \leq 1$. Tuning of Δ is a trade-off between sampling frequency and the limit of the minimum word length to be used.

The δ-operator will not be used in this thesis, though it is important to be aware of the possibility to shorten the word length. Thus, the next steps show how to obtain the mathematical equations needed for implementing the algorithm.

By applying (3.66) to the discrete transfer function in (3.62), the PR transfer function can be represented as in [41]. The discretised transfer function using the δ-operator yields

$$G_{PR}(z) = \frac{\beta_0 \delta^2 + \beta_1 \delta + \beta_2}{\alpha_0 \delta^2 + \alpha_1 \delta + \alpha_2} \tag{3.67}$$

where the coefficients are given by

$$\beta_0 = b_0 \tag{3.68}$$

$$\beta_1 = \frac{2b_0 + b_1}{\Delta} \tag{3.69}$$

$$\beta_2 = \frac{b_0 + b_1 + b_2}{\Delta^2} \tag{3.70}$$

$$\alpha_0 = 1 \tag{3.71}$$

$$\alpha_1 = \frac{2 + a_1}{\Delta} \tag{3.72}$$

$$\alpha_2 = \frac{1 + a_1 + a_2}{\Delta^2} \tag{3.73}$$

To deploy the PR transfer function with use of minimal word length, it is desired to represent the discrete PR controller using the δ-operator. Therefore, if the ordinary coefficients a_1, a_2, b_0, b_1 and b_2 were found using the inbuilt $c2d()$- Matlab function, transformation to the δ-operator using the equations (3.68)-(3.73) must be used. Further, these equations are deployed to the microcontroller using the DFIIt-method [41]. Implementation of an IIR-filter using the DFIIt-method is shown in Figure 3.6.
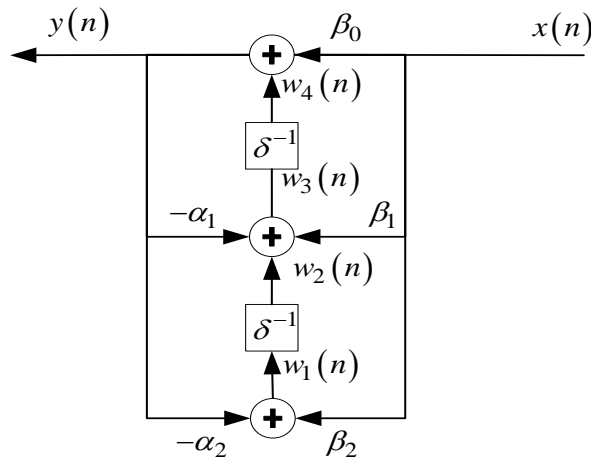
Figure 3.16 Implementation of an IIR filter using the direct form II transposed.

Figure 3.6 shows the digital structure that should be used during implementation of a DFIIt-method. Based on Figure 3.6, the equations that should be coded for the DSP are as follows

$$y(n) = \beta_0 x(n) + w_4(n) \tag{3.74}$$

$$w_1(n) = \beta_2 x(n) - \alpha_2 y(n) \tag{3.75}$$

$$w_2(n) = \Delta w_1(n-1) + w_2(n-1) \tag{3.76}$$

$$w_3(n) = \beta_1 x(n) - \alpha_1 y(n) + w_2(n) \tag{3.77}$$

$$w_4(n) = \Delta w_3(n-1) + w_4(n-1) \tag{3.78}$$

Chapter 4

In this chapter, adaptive controllers under unbalanced conditions are studied. Under unbalanced conditions and frequency fluctuations, it is of high importance to have a controller that can track the current under frequency deviations and contradict the effect of the converter.

4 Proportional Resonant Controllers for Circulating Current Suppression

In recent years, wind turbines and photovoltaic systems are increasing their share of the total energy production. Integrating wind turbines and PV systems into the grid may cause some challenges, and the most challenging may be the predictability of the wind. The varying wind power may cause the fundamental frequency to deviate from its original value, which in Europe is 50Hz, and cause instability to the grid. Most grid operators, such as Statnett in Norway, have therefore imposed strict standards on interconnecting wind turbines and PV systems to the grid. For example, in Norway wind turbines are obliged to stop producing if their frequency is outside the 50 ± 2 Hz limit [42]. In case of the MMC, it is of utmost importance to track the frequency deviation because a change of 2 Hz in the fundamental frequency results in a change of 4 Hz in the circulating current's second harmonic. Remembering from chapter 3, the PR controller has a narrow resonant bandwidth targeted for a specific frequency. A question then arises: "In a low bandwidth system, will the PR controller still be able to suppress the 2nd harmonic components in the circulating current, or is some kind of adaptive controllers needed?".

This chapter demonstrates the effects of a non-adaptive and adaptive PR controllers in a system with varying fundamental frequency using simulations. An approach to an adaptive PR controller with use of an adaptive PLL as used in [1] and [2] will be evaluated to check which of them are most efficient when tracking the circulating current during grid oscillations in high, medium and low bandwidth systems.

4.1 Non-Adaptive Proportional Resonant Controller

For the optimally tuned PR controller, the proportional gain is often enough to suppress most harmonics in a system. In modular multilevel converters with low switching frequency, the bandwidth is limited due to converter dynamics. From section 3.1.2, the rule of thumb governing the bandwidth of the system was given by $\alpha_c \leq \omega_s/10$, and that the bandwidth is proportional to the switching frequency. Hence, in a low switching frequency system, the bandwidth becomes lower. According to (3.14) the bandwidth is governed by $\alpha_c = K_P/L$, which shows that the proportional gain is proportional to the system's bandwidth. By lowering the bandwidth, the proportional gain

decreases to such an extent that the proportional controller becomes less and less effective. Consequently, lower proportional gain results in both a higher second harmonic component and errors as the system is not able to suppress the frequency components in the system.

Several simulations were performed to experimentally investigate if the resonant bandwidth is enough to suppress grid frequency deviations up to 2 Hz from the fundamental frequency. Table 4.1 shows the parameters that were used in the simulation. It is assumed that all parameters, except the frequency, are constant during the simulation.

Table 4.1 Parameters used in the simulation

Parameters	Value	
$V_{s,rms}$	230	V
N	6	
R_{grid}	10	Ω
L_{grid}	1	mH
f_0	50, 52	Hz
R_{arm}	0.1	Ω
L_{arm}	10	mH
f_{sw}	3240	Hz

In this simulation, the non-adaptive PR controller is tuned for the 100 Hz component of the circulating current. The PR controller was activated at t=1.0, and the fundamental grid frequency was changed from 50 Hz to 52 Hz at t=2.0 s.

Various values of K_p were simulated, and Table 4.2 shows the results. The results of interest are the circulating current error compared to its reference value and the second harmonic component in the circulating current. Hence, a bandpass filter targeting the second harmonic was used to filter out other frequency distortions. This is to get a more unobstructed view of the component of interest.

According to (3.25), the resonant bandwidth was calculated to $\alpha_r = \alpha_c/20$ in ideal conditions. This was to ensure ideal combination of both resonant and proportional gain. However, the resonant bandwidth does only affect the bandwidth of the targeted frequency- and not the system stability. Tuning of α_f can be more or less chosen freely, and typically this value will be in the range of a couple of hundred radians per second, and in most cases lower than ω_0 [13]. To cross-check the values calculated equation (3.21) is referred to, and it determines that the resonant gain was given by $K_R=2\alpha_f K_P$. Though, in a low bandwidth system, it is desired to have a slightly higher α_f than ω_0. This is to ensure some tolerance around the targeted frequency. Thus, the chosen resonant gains are held constant when proportional gain $K_P < 10.18$.

Table 4.2 Simulation results with different values of K_P for a varying grid frequency

K_P	K_R	f_0(Hz)	Time (s)	$I_{c,rms}$ (A)	BPF (A)	Error (A)	THD	$2f_0$
							FFT (% of f_0)	
40.72	16,577	50	1.2 ≤ t ≤ 2.0	7.92	7.32E-2	1.56E-1	64.58	0.25
		52	2.2 ≤ t ≤ 3.0	7.91	7.72E-2	1.59E-1	63.17	9.97
20.38	4144.3	50	1.2 ≤ t ≤ 2.0	7.94	1.18E-1	2.09E-1	70.93	0.56
		52	2.2 ≤ t ≤ 3.0	7.94	1.23E-1	2.06E-1	76.11	31.41
10.23	1036.1	50	1.2 ≤ t ≤ 2.0	7.97	1.49E-1	2.50E.1	81.01	0.55
		52	2.2 ≤ t ≤ 3.0	7.95	2.14E-1	2.86E-1	165.40	130.70
5.09	1036.1	50	1.2 ≤ t ≤ 2.0	8.02	2.20E-1	3.62E-1	68.51	0.49
		52	2.2 ≤ t ≤ 3.0	8.00	3.14E-1	4.44E-1	103.09	77.60
2.04	1036.1	50	1.2 ≤ t ≤ 2.0	8.01	3.86E-1	5.22E-1	139.03	12.16
		52	2.2 ≤ t ≤ 3.0	7.98	3.50E-1	5.10E-1	138.32	80.58
1.04	1036.1	50	1.2 ≤ t ≤ 2.0	8.16	1.42	1.56	858.53	64.61
		52	2.2 ≤ t ≤ 3.0	7.98	3.86E-1	5.58E-1	137.94	79.88

The results in Table 4.2 show that lower proportional gain results in a higher circulating current error. The FFT analysis reveals that the second harmonic in the circulating current increases almost linearly as the proportional gain was reduced. Even the original tuned PR controller with K_p = 40.72 has a second harmonic frequency component when the frequency changes from 100Hz to 104 Hz.

There are two values in Table 4.2 which stand out from the results. First, where K_P=10.18. The FFT analysis reveals a second harmonic component which is not proportional to the other values. This confirms that an adaptive controller is necessary in a system with medium bandwidth. Second, where K_P = 1.04. The proportional gain is very low, and hence the activation of the resonant controller at t = 1.0 s acts as a disturbance which the system uses 0.3 seconds to control. Thus, the error was measured to 1.42 A.

Based on the results, the answers imply that another approach is needed to suppress the second harmonic frequency component in the circulating current under varying frequency conditions. Thus, the adaptive PR controller will be introduced and further explained in section 4.2.

4.2 Adaptive Proportional Resonant Controller

4.2.1 The Continuous Second-Order Generalised Integer (SOGI)

Second-order generalised integer is a building-block technique used to represent second-order transfer functions in a state-space representation. This technique is usually found in control systems for internal control and grid synchronisation where stability is focused. SOGI enables adaptive control as the fundamental frequency f_o can be measured from the grid and feed-forwarded into the controller. This results in a fast and efficient control system. The resonant transfer function

for the circulating current for the ideal and non-ideal PR controller was shown in (3.11) and (3.12), respectively. For convenience, they are repeated in (4.1) and (4.2).

$$G_{C,ideal}(s) = K_P + \frac{K_R \omega_0}{s^2 + (h\omega_0)^2} \tag{4.1}$$

$$G_{C,non-ideal}(s) = K_P + \frac{K_R s}{s^2 + \omega_c s + (h\omega_0)^2} \tag{4.2}$$

Equation (4.1) and (4.2) are drawn in SOGI-form in Figure 4.1 and Figure 4.2, respectively.
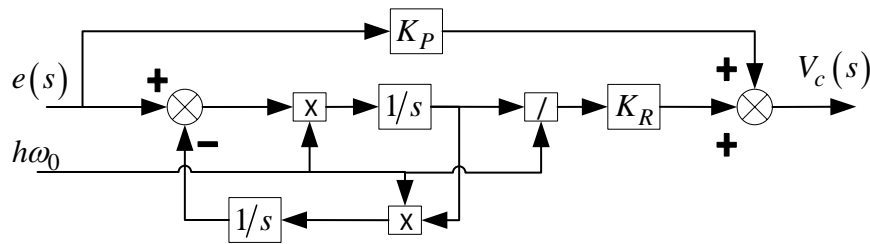
Figure 4.1 SOGI representation of the ideal PR controller [43].
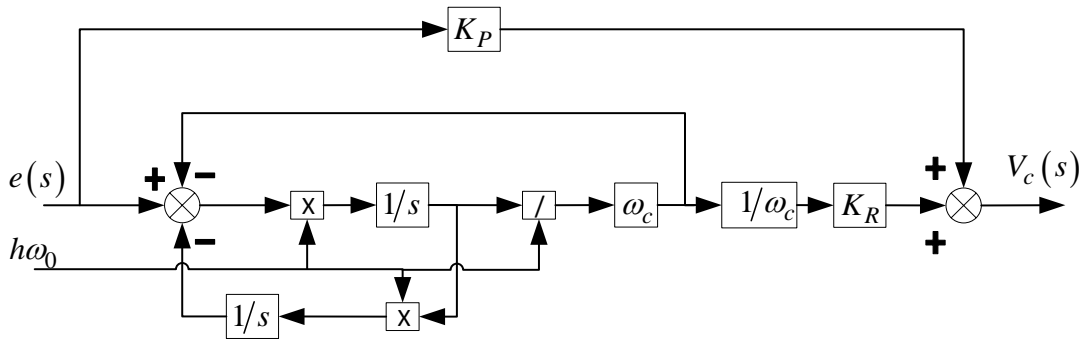
Figure 4.2 SOGI representation of the non-ideal PR controller [43].

4.2.2 Bode Plot Analysis of Adaptive PR Controllers

The results in Table 4.2 show that the resonant controller was not able to suppress the $2\omega_0$ component when the frequency deviated by 2 Hz from the fundamental frequency. This became more apparent when the proportional gain was reduced. Though, it is not very surprising as a 2 Hz step in the fundamental frequency results in a 4 Hz step in the second harmonic component. If the initially targeted second harmonic is 100 Hz, the 2 Hz grid step causes the initially targeted second harmonic to miss by 4 Hz. Consequently, the gain reduces significantly.

Bode plots can be used to get a broader understanding, and the equivalent transfer functions used for the results in Table 4.2 are depicted in Figure 4.3 to Figure 4.8. In addition, transfer functions targeting the $2f_0$ component for a grid current with a fundamental frequency of 48, 50 and 52 Hz are also plotted respectively in blue, red and yellow. The figures are split into two parts; **(a)** shows magnitude and frequency response, and **(b)** shows the magnitude response around the resonant frequencies $2(50\pm2)$Hz.
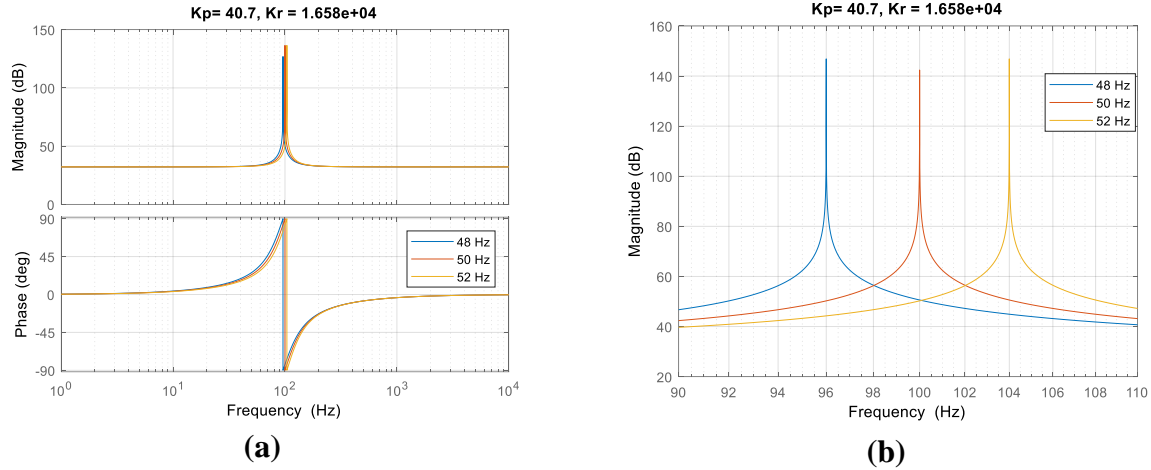
Figure 4.3 Bode plots with K_P=40.7 and K_R=16,5870 where **(a)** shows the magnitude and frequency response of the transfer function, and **(b)** shows the magnitude response around the frequencies at $2(50\pm2)$ Hz.

In Figure 4.3, the original tuning of the converter is shown. The steady-state gain at frequencies far from the resonant peak is measured to 32.2dB, which is not surprisingly the decibel value representing the actual tuned proportional gain K_P =40.7 in the linear representation. More interestingly is the gain around the targeted frequency $2f_0$. In a non-adaptive converter, the controller gain reduces significantly when the frequency deviates further away from the peak. E.g. a grid fluctuation of 2 Hz results in a 4 Hz change in the circulating current, and the gain is then reduced to 50.6 dB. Even this gain is not able to effectively suppress the second harmonic component in the circulating current since the FFT analysis in Table 4.2 revealed that the second harmonic component was measured to 9.97 %.

Plots of the other results are shown in Figure 4.4 to Figure 4.8.
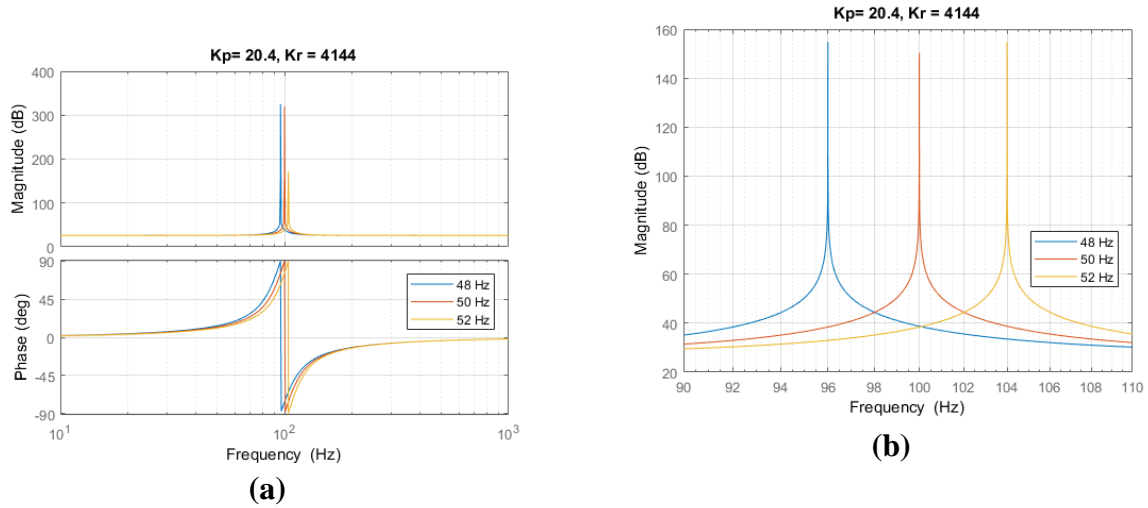
Figure 4.4 Bode plots with K_P=20.4 and K_R=4,144.3 where **(a)** shows the magnitude and frequency response of the transfer function, and **(b)** shows the magnitude response around the frequencies at $2(50\pm2)$Hz.
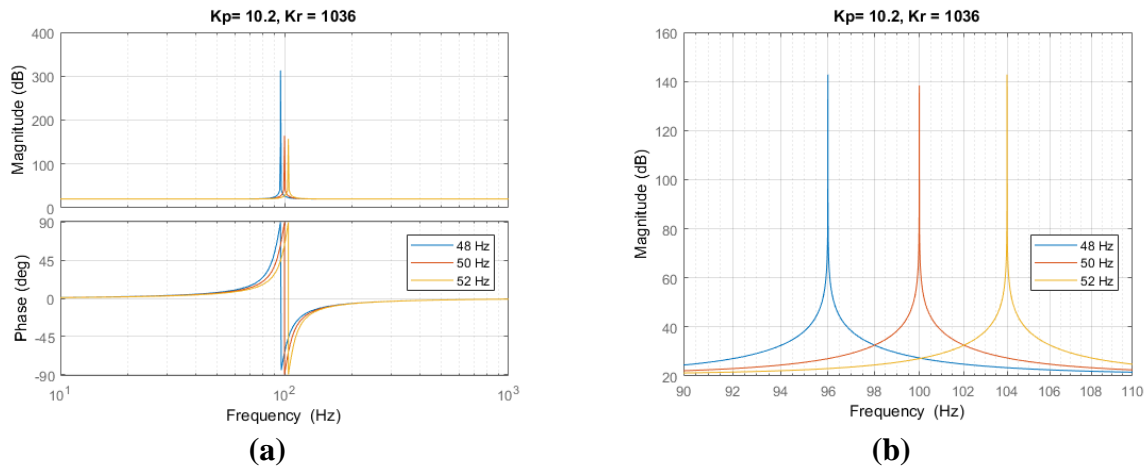
Figure 4.5 Bode plots with K_P=10.2 and K_R=1,036.1 where **(a)** shows the magnitude and frequency response of the transfer function, and **(b)** shows the magnitude response around the frequencies at $2(50\pm2)$Hz.
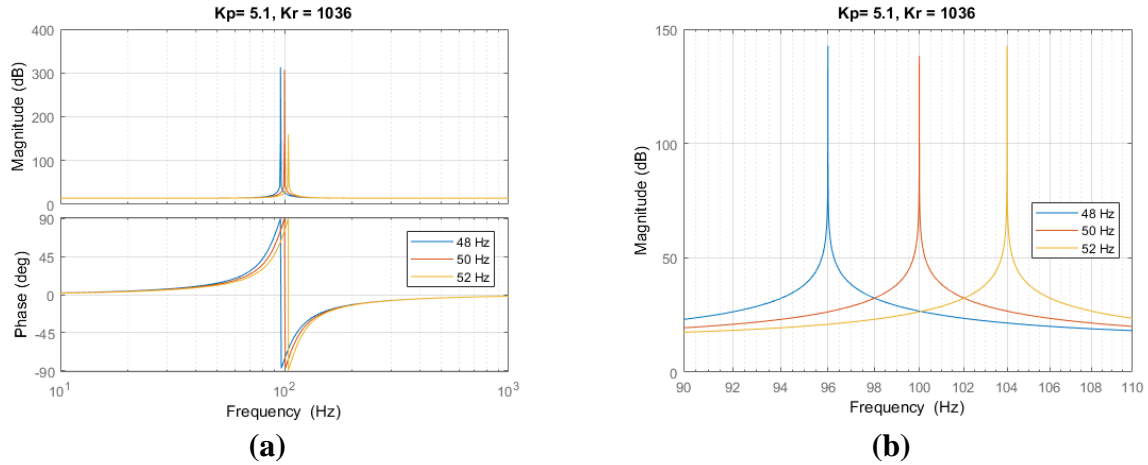
Figure 4.6 Bode plots with K_P=5.1 and K_R=1,036.1 where **(a)** shows the magnitude and frequency response of the transfer function, and **(b)** shows the magnitude response around the frequencies at $2(50\pm2)$Hz.
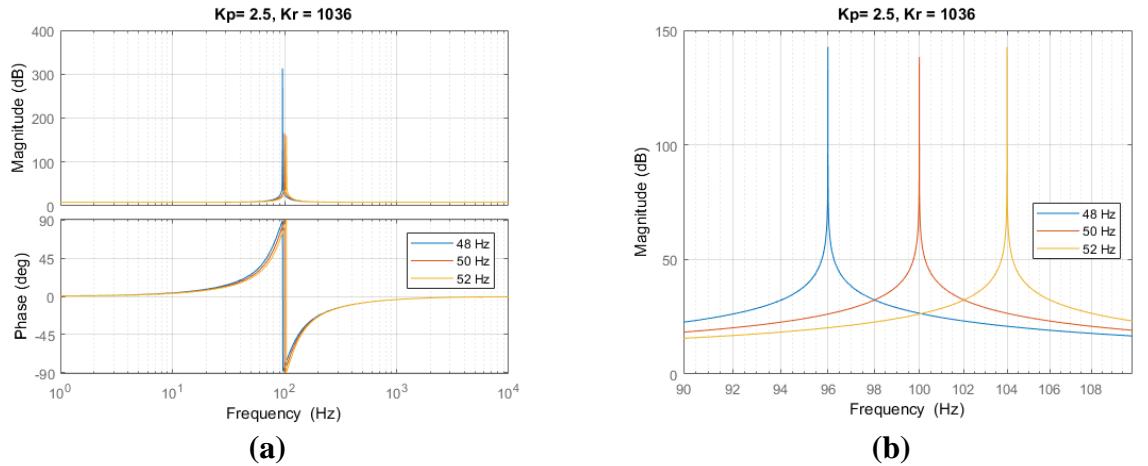
Figure 4.7 Bode plots with K_P=2.5 and K_R=1,036.1 where **(a)** shows the magnitude and frequency response of the transfer function, and **(b)** shows the magnitude response around the frequencies at $2(50\pm2)$Hz.
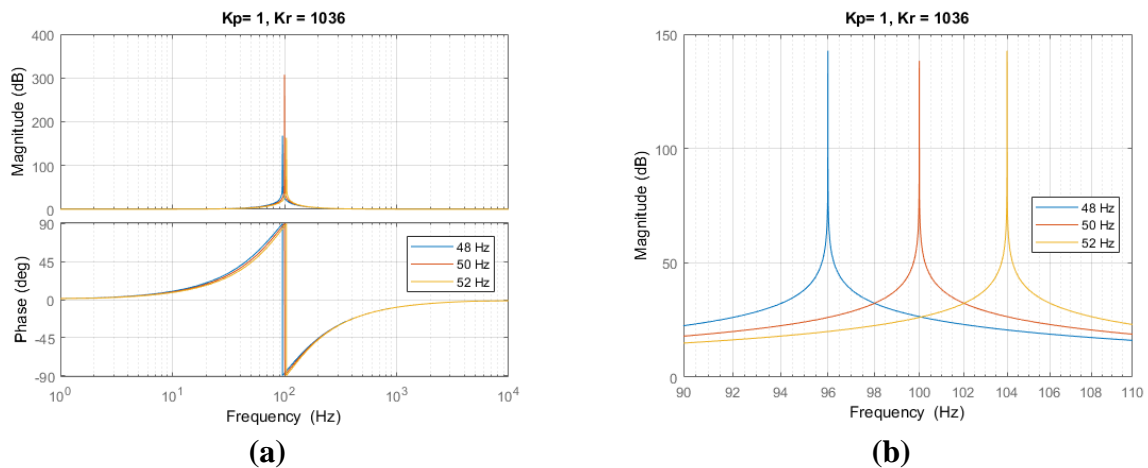
Figure 4.8 Bode plots with K_P=1.04 and K_R=1,036.1 where **(a)** shows the magnitude and frequency response of the transfer function, and **(b)** shows the magnitude response around the frequencies at $2(50\pm2)$Hz.

Figure 4.4 and Figure 4.5 show that decreasing the proportional and resonant bandwidth results in a lower gain at frequencies outside the targeted $2f_0$-component. The gain at 104 Hz for the two plots above was measured to 36.7 dB and 27.4 dB, where the respective second harmonic component was measured to 31.41 % and 130.70 %. In Figure 4.6 to Figure 4.8 the resonant gain was kept at 1,036.1, and hence the suppression gain at 104 Hz is equal to 27.4 dB. Still, the second harmonic component increases as the proportional gain is lowered.

The results show that the error and the second harmonic component increase as the proportional gain is lowered. In a low bandwidth system, where the proportional gain is low, there is a high necessity of an adaptive controller which can suppress harmonic components in case of grid frequency flickering. Section 4.3 shows and demonstrates two methods on how to make a discrete implementation of an adaptive SOGI to a biquad filter. The idea is to make the resonant peak adjust according to the fundamental frequency.

4.3 Discrete Implementation of the Adaptive PR Controller

As stated in 3.1.1, realisation of the non-ideal PR controller to a microcontroller gives better precision as the non-ideal PR controller has a finite gain. Therefore, discretising of the non-ideal PR controller is done. The discretised non-ideal PR controller's transfer function is shown in (4.3), and the parameters were derived in the following equations (3.57), (3.58) and (3.63)-(3.65).

$$H_{PR,d}(z) = \frac{b_0 + b_1 z^{-1} + b_2 z^{-2}}{1 + a_1 z^{-1} + a_2 z^{-2}} \tag{4.3}$$

To achieve a fast and dynamic response of the controller, it is possible to make the filter in (4.3) adaptive. The next two subsections will introduce two adaptive methods which focus on changing parameter a_1 with use of PLL to measure the grid frequency and thus change the resonant peak of the converter. The first method, proposed in [1], focuses on changing ω_0. The second method focuses on changing the sampling time, Ts [2].

Revision of section 3 must be reviewed in order to understand why only changing one of the five parameters is enough to make the filter adaptive. Therefore, investigation of the denominator must be undertaken. As discussed in 3.5.1, parameter a_1 and a_2 was approximated to

$$a_1 = -\frac{2h\omega_0 \cos(h\omega_0 T_s)}{h\omega_0 + 1/2\,\omega_c \sin(h\omega_0 T_s)} \approx -2\cos(h\omega_0 T_s) \tag{4.4}$$

$$a_2 = \frac{h\omega_0 - 1/2\,\omega_c \sin(h\omega_0 T_s)}{h\omega_0 + 1/2\,\omega_c \sin(h\omega_0 T_s)} \approx 1 \tag{4.5}$$

It is important to remember that using these approximations will give inaccurate results, and therefore they can only be applied to get a general understanding of the dynamics. Using the above approximations, the denominator of (4.3) is rewritten to (4.6).

$$Den_R(z) = 1 - 2\cos(h\omega_0 T_s)z^{-1} + z^{-2} \tag{4.6}$$

Factorising is used to show that (4.6) has a zero-point which causes the resonant peak. First, equation (4.6) is multiplied by z^2 which yields

$$Den_R(z) = z^2 - 2\cos(h\omega_0 T_s)z + 1 \tag{4.7}$$

Second, to show that equation (4.7) equals zero, the quadric equation can be used to find the solutions

$$z = \frac{-\left(-2\cos(h\omega_0 T_s)\right) \pm \sqrt{\left(-2\cos(h\omega_0 T_s)\right)^2 - 4}}{2} \tag{4.8}$$

$$z = \cos(h\omega_0 T_s) \pm \sqrt{\cos^2(h\omega_0 T_s) - 1} \tag{4.9}$$

$$z = \cos(h\omega_0 T_s) \pm \sqrt{\cos^2(h\omega_0 T_s) - \left(\cos^2(h\omega_0 T_s) + \sin^2(h\omega_0 T_s)\right)} \tag{4.10}$$

$$z = \cos(h\omega_0 T_s) \pm j\sin(h\omega_0 T_s) = 1e^{\pm jh\omega_0 T_s} \tag{4.11}$$

Last, the denominator is then rewritten to

$$Den_R(z) = \left(z + 1e^{jh\omega_0 T_s}\right)\left(z + 1e^{-jh\omega_0 T_s}\right) \tag{4.12}$$

Drawing (4.12) on the unity circle in in Figure 4.9 helps to visualise the actual solution of the equation. The value $e^{\pm jh\omega_0 T_s}$ decides the angle of a vector where the sign $\pm$ determines if there is a positive or a negative angle. As shown in Figure 4.9, both polynomials have the same value along the real axis. This results in one pole pair on the real axis, and thus the resonant peak is common for both polynomials. Figure 4.9 also shows that a change of either ω_0 or T_s results in the same new resonant peak as the Re(Z) is equal.
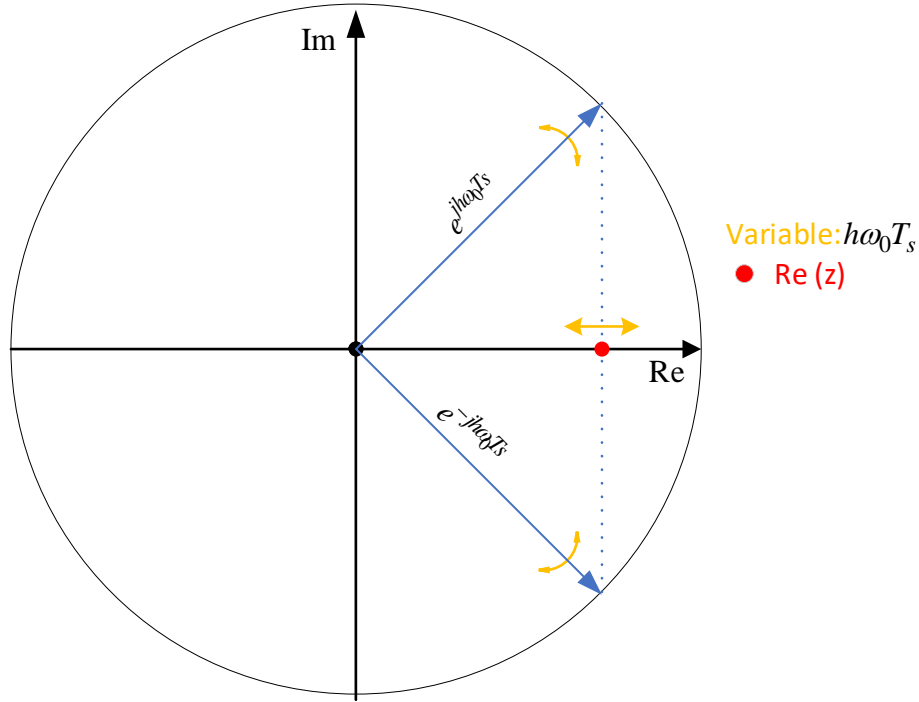
Figure 4.9 The unit circle is showcasing that a change of either ω_0 or T_s changes the resonant peak.

Based on the derivations done for the denominator and the unit circle, a change of either ω_0 or T_s results the same new resonant peak. The approximations and derivations resulting in the unity circle were based on only the variable term of the approximated a_1 parameter. However, looking at the original tuning of a_1, the first part of (4.4), it is evident that changing ω_0 or T_s will result in a different dynamic behaviour. Hence, the two methods will be investigated in 4.3.1 and 4.3.2.

4.3.1   Adaptive Sampling Time

This method is used in [2], where a PR controller is made adaptive by changing the sampling time T_s. The adaptive controller was used for a high sampling frequencies application using a fixed-point implementation. Several simulations with different sampling frequencies to see how it affects the error were run. There was not given a specific explanation on how it is made adaptive, but the PR controller has been discretised using Tustin's pre-warped approximation. Therefore, to explain how changing T_s makes the filter adaptive, the abovementioned explanation using equation (4.12) and the unit circle in Figure 4.9 is referred to.

An interesting observation of the approximated denominator in (4.6), $1-2\cos(2h\omega_0 T_s)z^{-1}+z^{-2}$, is that a change of 1 µs is equivalent to a change of 1 Hz in the fundamental frequency. The following mathematical derivation of the term inside $2\cos(2h\omega_0 T_s)$ confirms the relation.

$$4h\pi\left(f_0+2\text{Hz}\right)T_s\Big|_{\substack{f_0=50\text{Hz}\\T_s=50\mu s}} = 4h\pi f_0\left(T_s+2\mu s\right)\Big|_{\substack{f_0=50\text{Hz}\\T_s=50\mu s}} \tag{4.13}$$

Solving (4.13) gives the same answer. In regards to the resonant peak, there is a one-to-one corre-
lation between the fundamental frequency and sampling time. For simulations in Simulink, the
filter is made adaptive with use of an adaptive phase locked loop (PLL) of the grid frequency and
a look-up table (LUT). The simulation setup is shown in Figure 5.1 and Figure 5.2.

4.3.2   Adaptive IIR Digital PR Controller

Paper [1] proposes a method that is based on discretising the PR controller using Tustin pre-warped
approximation to be implemented in a digital IIR filter. The resonant peak of the filter is made
adaptive by changing ω_0 in a_1. Thus, the unit circle explanation can be used to show how it can be
made adaptive as well. Section 4.3 demonstrated that the denominator of the biquad filter in (4.3)
was made adaptive with the help of equation (4.12) and the unity circle depicted in Figure 4.9.

In contrast to [2], [1] suggests to only change ω_0 and not the sampling time T_s. A closer look at the
parametrised variable a_1 in [1] yields

$$a_1 = -\sqrt{a_2}\,\cos\left(h\omega_0 T_s\right) \tag{4.14}$$

where $a_2 = \left(1 - \zeta \sin\left(h\omega_0 T_s\right)\right)/\left(1 + \zeta \sin\left(h\omega_0 T_s\right)\right)$ and ξ is the damping factor. Thus, the proposed
filter in [1] has the same adaptive behaviour as explained in equation (4.4). As seen in equation
(4.4), parameter a_1 has ω_0 in all terms of the equation. Therefore, it is believed that changing ω_0
to correlate with the measured grid frequency give more accurate suppression than the adaptive T_s.
Though, this remains to be investigated in chapter 5.

Chapter**5**

Now that all the internal dynamics of the adaptive IIR filter have been studied, it is time to analyse their behaviour with the help of simulations. The results in this section are recorded without implementation of the arm energy controller because the fundamental f_0-component would interfere with the total harmonic distortion and the $2f_0$ component.

5 Simulation Results

Simulations of the method proposed by [1] and [2] were done using the simulation model presented in *Appendix A - Matlab and Simulink* Model. Table 5.1 shows the different activation times of the various controllers used in the simulation.

Table 5.1 Overview of time and activation of different controllers

Time (s)	Activation of Controller
1.0	Non-adaptive CCSC biquad filter
2.0	Frequency step to 52Hz
3.0	Adaptive Controller activated

Simulations were run without using the output and arm energy-balancer controller. The MMC demonstrated that it was able to operate in steady-state without an arm energy balancer. To analyse the circulating current without any disturbances, it was decided not to activate the arm energy controller as the f_0 component would interfere with the result. In terms of the output current controller, the output reference signal was set to a constant equal to V_s/R_{grid}, which yields the actual value during optimal operation of the current controller. The reference value is activated at t = 0 seconds. Also, as there is no opposing grid voltage used in the simulations, the need for an output controller is less critical.
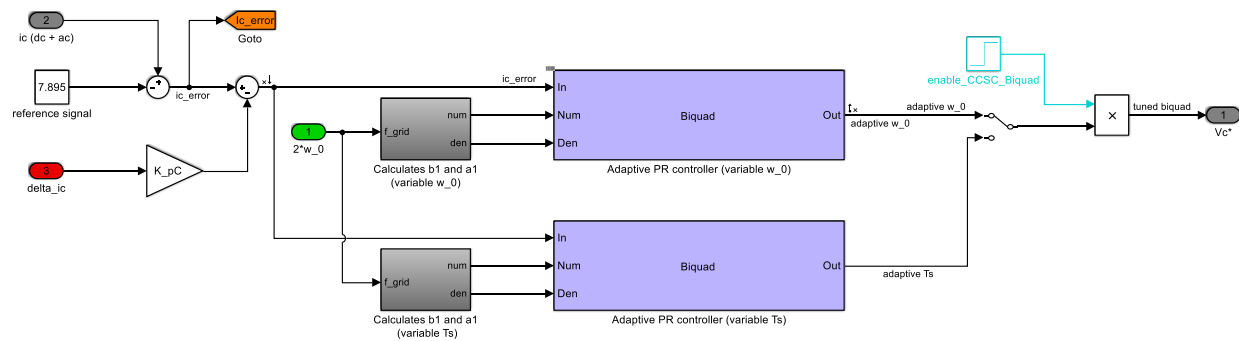
Figure 5.1 Overview of the circulating current controller using the biquad filter.
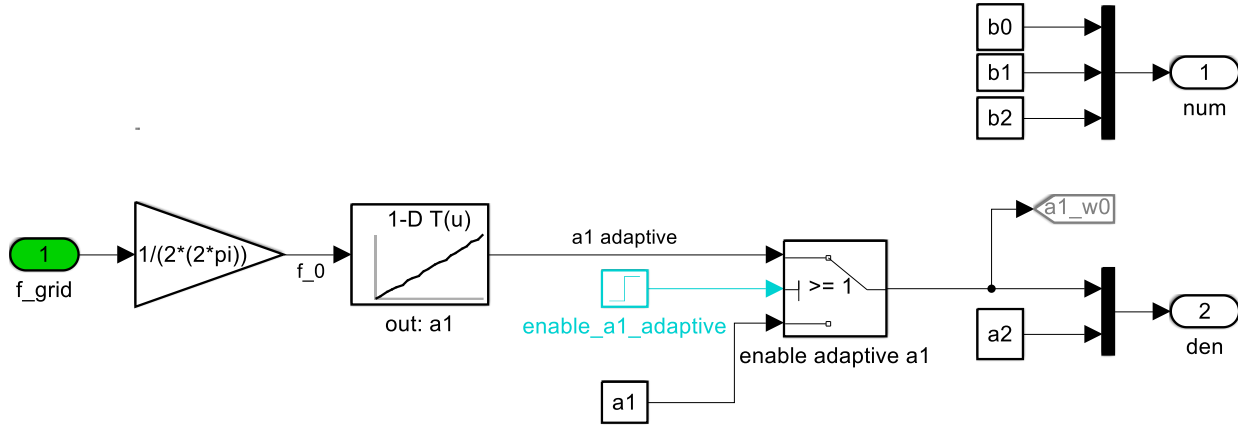
Figure 5.2 The method when making a_1 adaptive for the circulating current. The LUT has the precalculated the values of either T_s or ω_0 corresponding to the grid frequency.

Section 5.1 and 5.2 are dedicated to present the results for the adaptive ω_0 [1]and adaptive T_s [2], respectively. Each subsection is divided into smaller sections to present the scope of waveforms and THD. At the end of each subsection, the numerical results are summarised in one table to get an overview. After both sections have been presented, a table is presented to compare the effectiveness of the adaptive ω_0 and T_s.

In the simulation, a new action occurs every second. The PLL uses 0.2 seconds to catch up with the frequency step activated at t = 2.0 seconds, and hence the results are recorded the last 0.8 seconds before a new action is introduced. This is to get similar measurements of all simulations.

5.1 Adaptive IIR Digital PR Controller

KP = 40.72 AND KR = 16,577

In the time interval of $2.2 \leq t \leq 3.0$ in Figure 5.3, the circulating current was measured to 7.919 A, the bandpass filtered circulating current $\mathrm{BPF}(I_{\mathrm{circ}}) = 7.82\mathrm{E}\text{-}2$ A and the error was measured to 1.59E-1 A. This yields the ratio $\mathrm{BPF}(I_{\mathrm{circ}})/I_{\mathrm{circ}}$ to become 0.987 %.

After activation of the adaptive controller at t = 3.0, the following values were recorded in the period of $3.2 \leq t \leq 4.0$. The circulating current was recorded to 7.923 A, the bandpass filtered circulating current to $\mathrm{BPF}(I_{\mathrm{circ}}) = 7.88\mathrm{E}\text{-}2$ A and the error was measured to 1.61E-1 A. This yields the ratio $\mathrm{BPF}(I_{\mathrm{circ}})/I_{\mathrm{circ}}$ to become 0.994 %.

Figure 5.3 reveals a voltage difference between the upper and lower submodules. According to equation (3.38), the voltage difference should be the source to a fundamental f_0 component carrying energy between the arms. Thus, the total harmonic distortion is very low due to this high fundamental component. However, high suppression of the proportional gain manages to keep the fundamental component low. Implementation of an arm energy controller would even the voltage between the upper and lower arm, and consequently a lower f_0 component could be achieved.
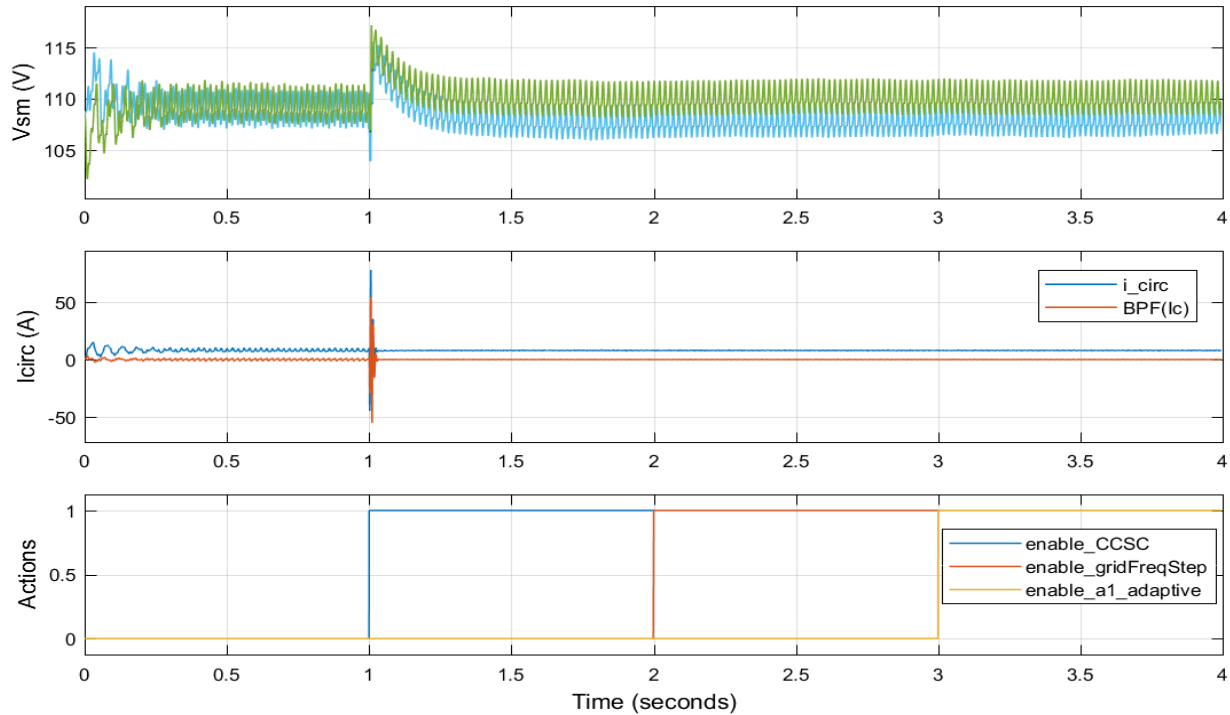
Figure 5.3 Adaptive ω_0 - overview of submodule voltages, the bandpass filtered and ordinary circulating current and actions at different times with the controller gain set to K_P=40.72 and K_R=16,577.

(a)   **(b)**
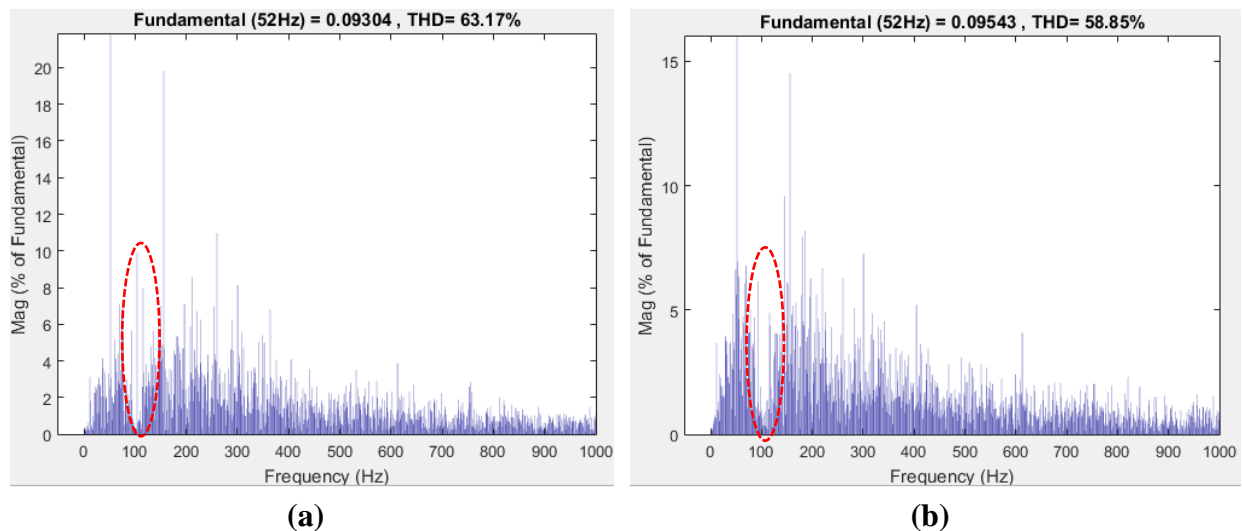
Figure 5.4 Adaptive ω_0 - harmonic spectrum with use of the circulating current, where **(a)** shows the non-adaptive controller in the time period of $2.2 \leq t \leq 3.0$, and **(b)** shows the adaptive controller in the period of $3.2 \leq t \leq 4.0$.

Figure 5.4 shows the total harmonic distortion in the circulating current. The THD decreased from 63.17 % to 58.85 % and the second harmonic component, which is circled in red, decreased from 9.97 % to 0.39 % after the adaptive controller was activated. Even though the spectrum analysis revealed a significant reduction of the second harmonic component, the bandpass filtered BPF(I_{circ}) slightly increased.

KP = 20.4 AND KR = 4,144.3
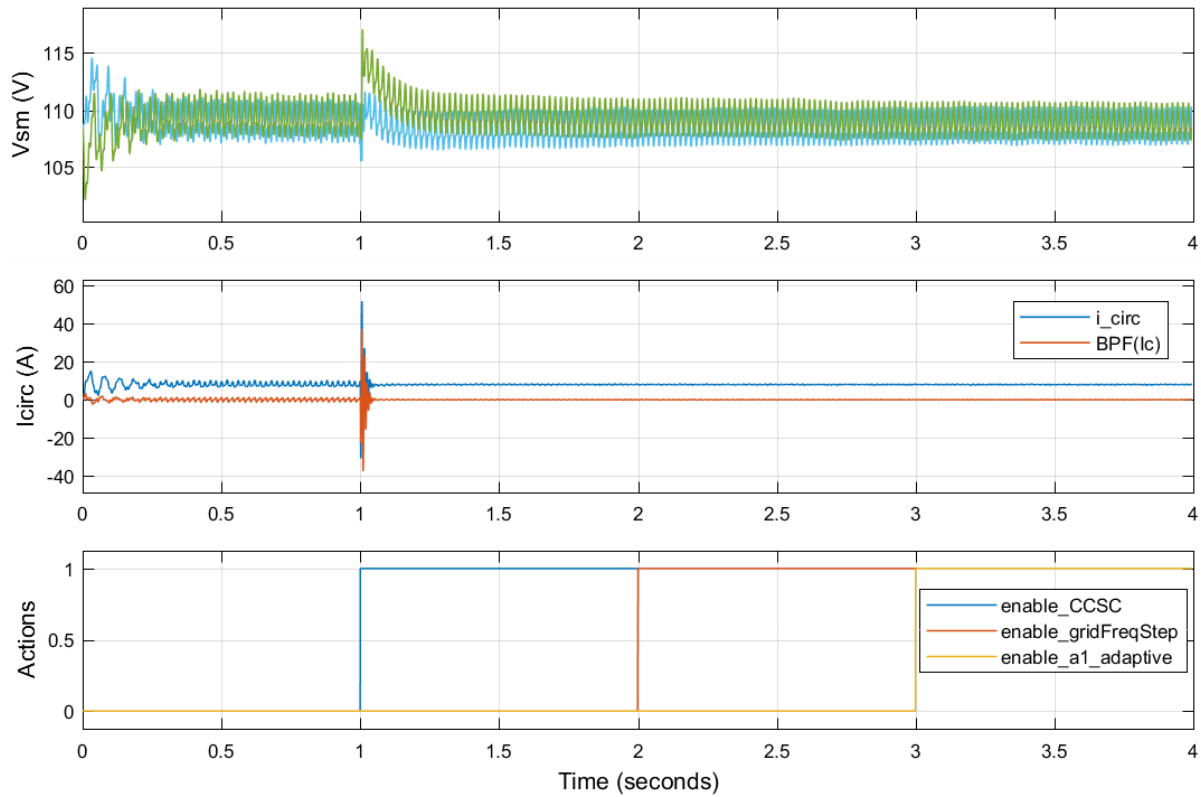
Figure 5.5 Adaptive ω_0 - overview of submodule voltages, the bandpass filtered and ordinary circulating current and actions at different times with the controller gain set to K_P=20.4 and K_R=4,144.3.

In the time interval of $2.2 \leq t \leq 3.0$ in Figure 5.5, the circulating current was measured to 7.94 A, the bandpass filtered circulating current BPF(I_{circ}) = 1.23E-1 A and the error was measured to 2.06E-1 A. This yields the ratio BPF(I_{circ})/I_{circ} to become 1.55 %.

After activation of the adaptive controller at t = 3.0 seconds, the following values were recorded in the period of $3.2 \leq t \leq 4.0$. The circulating current was recorded to 7.95 A, the bandpass filtered circulating current BPF(I_{circ}) = 1.36E-1 A and the error was measured to 2.26E-1 A. This yields the ratio BPF(I_{circ})/I_{circ} to become 1.71 %.
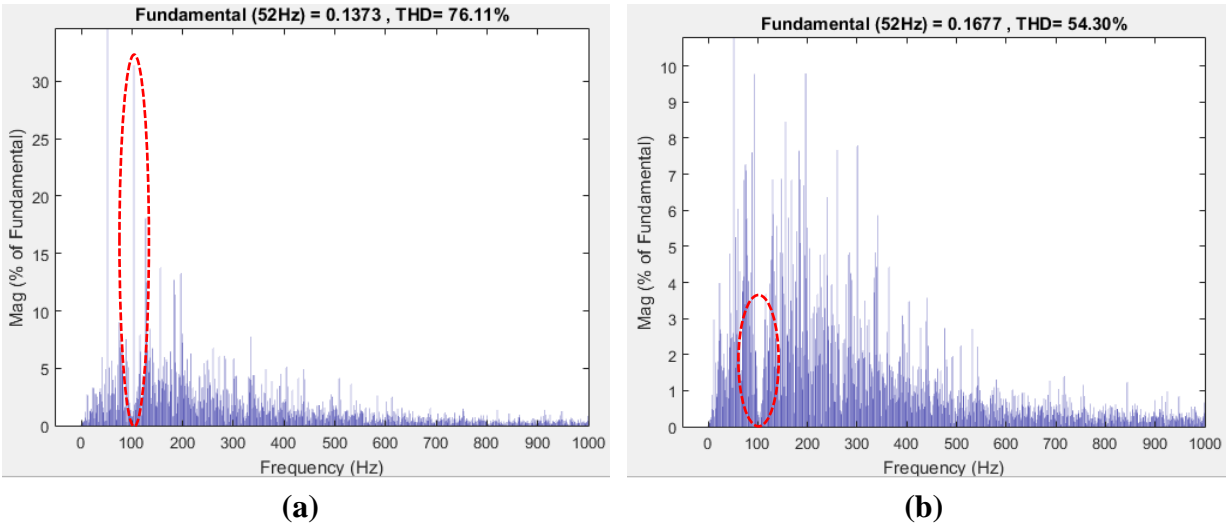
Figure 5.6 Adaptive ω_0 - harmonic spectrum with use of the circulating current, where **(a)** shows the non-adaptive controller in the period of $2.2 \leq t \leq 3.0$, and **(b)** shows the adaptive controller in the period of $3.2 \leq t \leq 4.0$.

Figure 5.6 shows the total harmonic distortion in the circulating current. The THD decreased from 76.11 % to 54.3 % and the second harmonic component, which is circled in red, decreased from 31.41 % to 0.41 % after activation of the adaptive controller. Also, it is seen that the second harmonic component acts as a disturbance until the adaptive controller is activated. At the time of activation, the harmonics are significantly reduced.

K$_P$ = 10.18 AND K$_R$ = 1,036.1
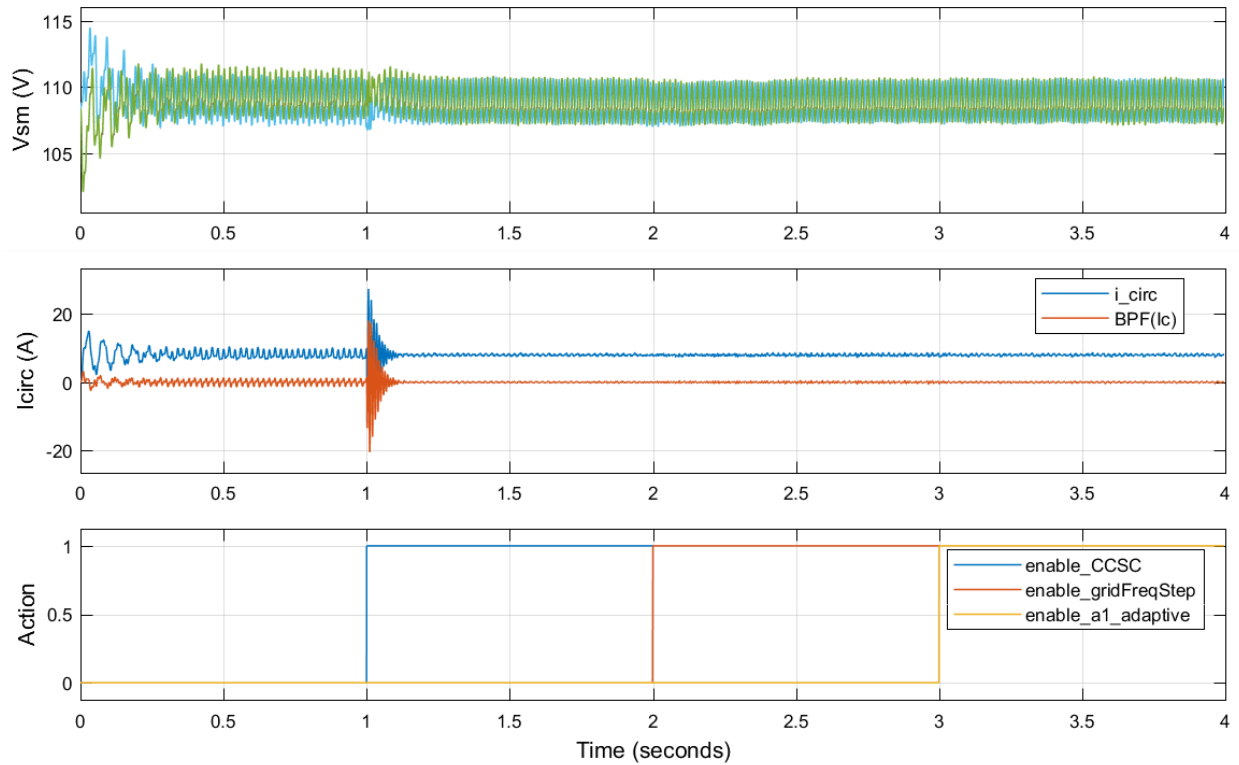
Figure 5.7 Adaptive ω_0 - Overview of submodule voltages, the bandpass filtered and ordinary circulating current and actions at different times with the controller gain set to K_P=10.23 and K_R=1,036.1

In the time interval of $2.2 \leq t \leq 3.0$ in Figure 5.7, the circulating current was measured to 7.953 A, the bandpass filtered circulating current BPF(I_{circ}) = 2.14E-1 A and the error was measured to 2.86E-1 A. This yields the ratio BPF(I_{circ})/I_{circ} to become 2.69 %.

After activation of the adaptive controller at t = 3.0 seconds, the following values were recorded in the period of $3.2 \leq t \leq 4.0$. The circulating current was recorded to 7.96 A, the bandpass filtered circulating current BPF(I_{circ}) = 1.06E-1 A and the error was measured to 2.50E-1 A. This yields the ratio BPF(I_{circ})/I_{circ} to become 1.33 %.
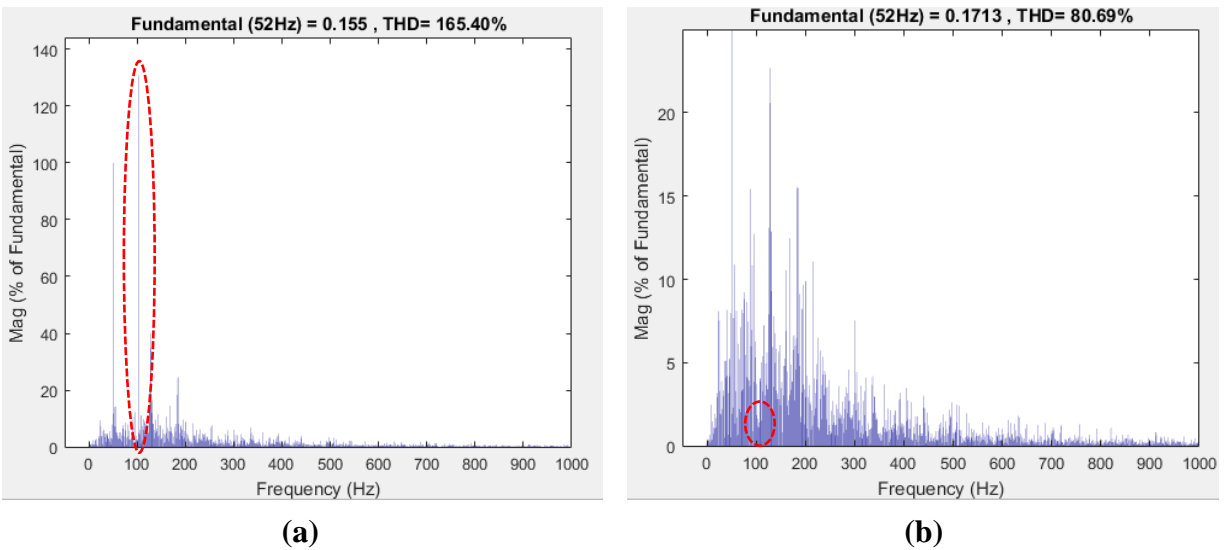
Figure 5.8 Adaptive ω_0 - harmonic spectrum with use of the circulating current, where **(a)** shows the non-adaptive controller in the period of $2.2 \leq t \leq 3.0$, and **(b)** shows the adaptive controller in the period of $3.2 \leq t \leq 4.0$.

Figure 5.8 shows the total harmonic distortion in the circulating current. The THD decreased from 165.40 % to 80.69 % and the second harmonic component, which is circled in red, decreased from 130.70 % to 1.63 % after the adaptive controller was activated.

Figure 5.8 also shows that harmonics outside the targeted $2f_0$ component starts to get a value of significant. As the proportional gain is lowered, the controller's ability to suppress harmonics becomes lower as well. Thus, the harmonics get more predominant in the current. Suppresing these harmonics are not the scope of this thesis, but they can be suppressed by a series resonant controller as shown in [37].

KP = 5.06 AND KR= 1,036.1
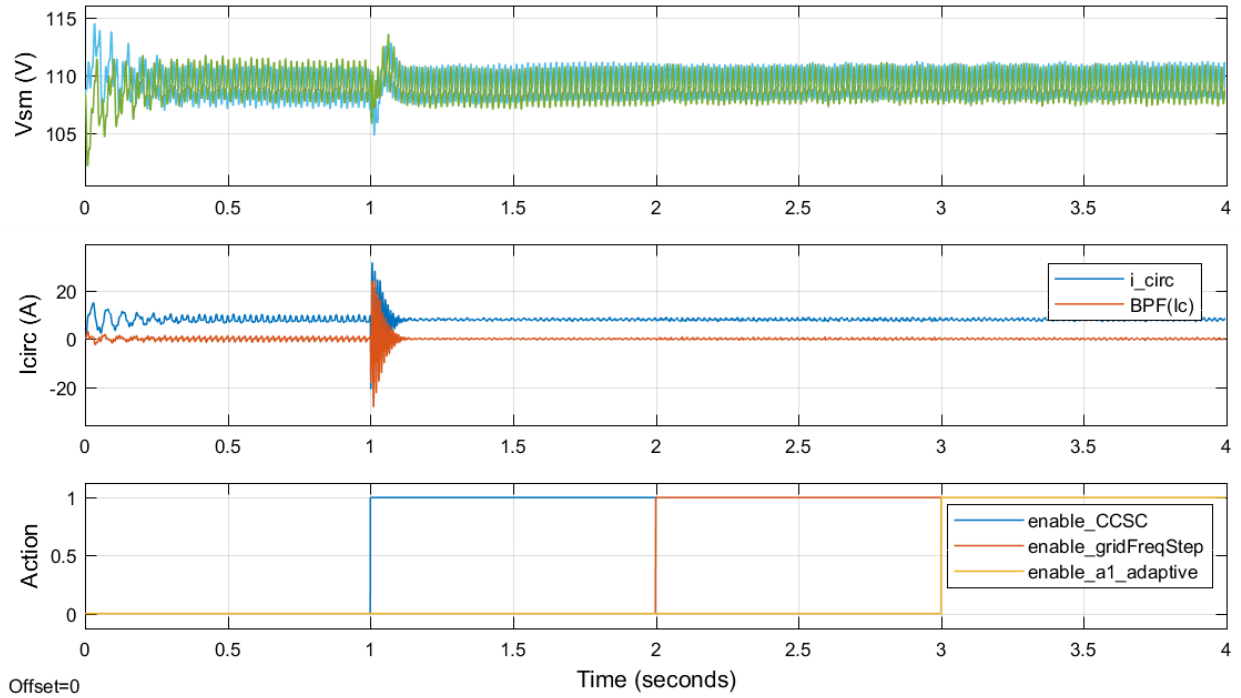
Figure 5.9 Adaptive ω_0 - Overview of submodule voltages, the bandpass filtered and ordinary circulating current and actions at different times with the controller gain set to K_P=5.06 and K_R=1,036.1.

In the time interval of $2.2 \leq t \leq 3.0$ in Figure 5.9, the circulating current was measured to 8.00 A, the bandpass filtered circulating current BPF(I_{circ}) = 3.14E-1 A and the error was measured to 4.44E-1 A. This yields the ratio BPF(I_{circ})/I_{circ} to become 3.93%.

After activation of the adaptive controller at t = 3.0 seconds, the following values were recorded in the period of $3.2 \leq t \leq 4.0$. The circulating current was recorded to 8.01 A, the bandpass filtered circulating current BPF(I_{circ}) = 2.81E-1 A and the error was measured to 4.30-1 A. This yields the ratio BPF(I_{circ})/I_{circ} to become 3.51 %.

According to classical control theory, there is a correlation between proportional gain and settling time. As seen in Figure 5.9, the settling time of the circulating current is higher as the proportional gain becomes lower. The controller's ability to suppress frequencies and other disturbances get lower due to the lowered proportional gain. This is confirmed by looking at the corresponding Bode plots that were drawn in section 4.2.2. Activation of the resonant gain resonant gain at t = 1 second introduces new harmonics into the system which acts as a disturbance. Due to the low proportional gain, the system has some settling time before stable operation.
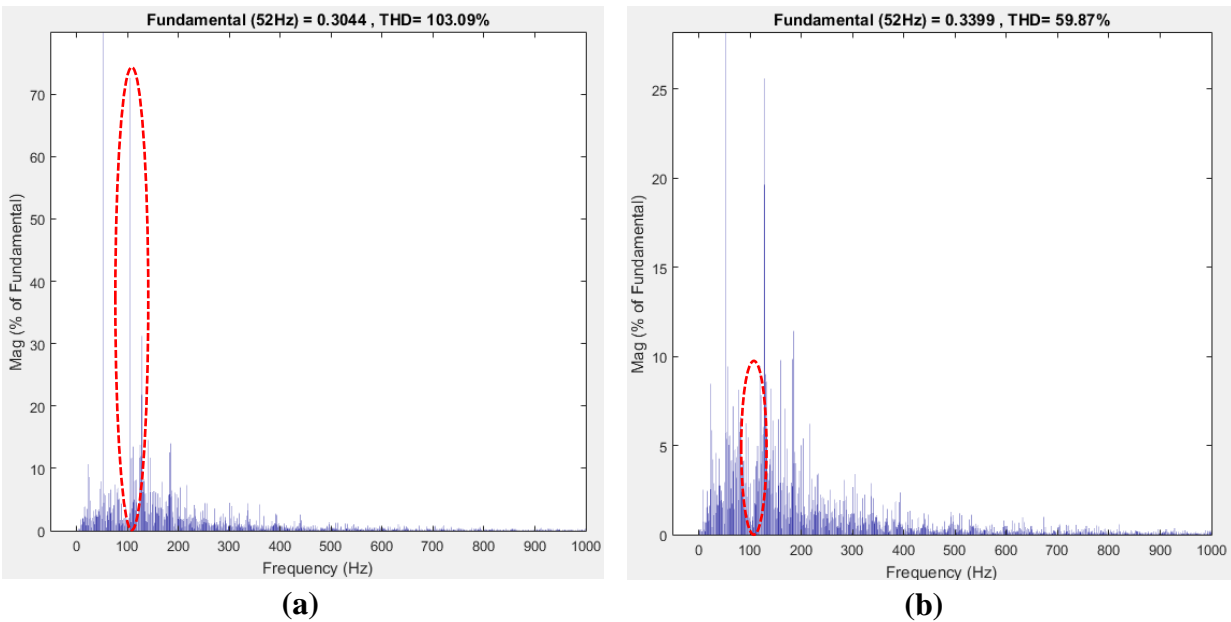
Figure 5.10 Adaptive ω_0 - harmonic spectrum with use of the circulating current, where **(a)** shows the non-adaptive controller in the period of $2.2 \le t \le 3.0$, and **(b)** shows the adaptive controller in the period of $3.2 \le t \le 4.0$.

Figure 5.10 shows the total harmonic distortion in the circulating current. The THD decreased from 103.09 % to 59.87 % and the second harmonic component, which is circled in red, decreased from 72.60 % to 0.78 % after the adaptive controller was activated.
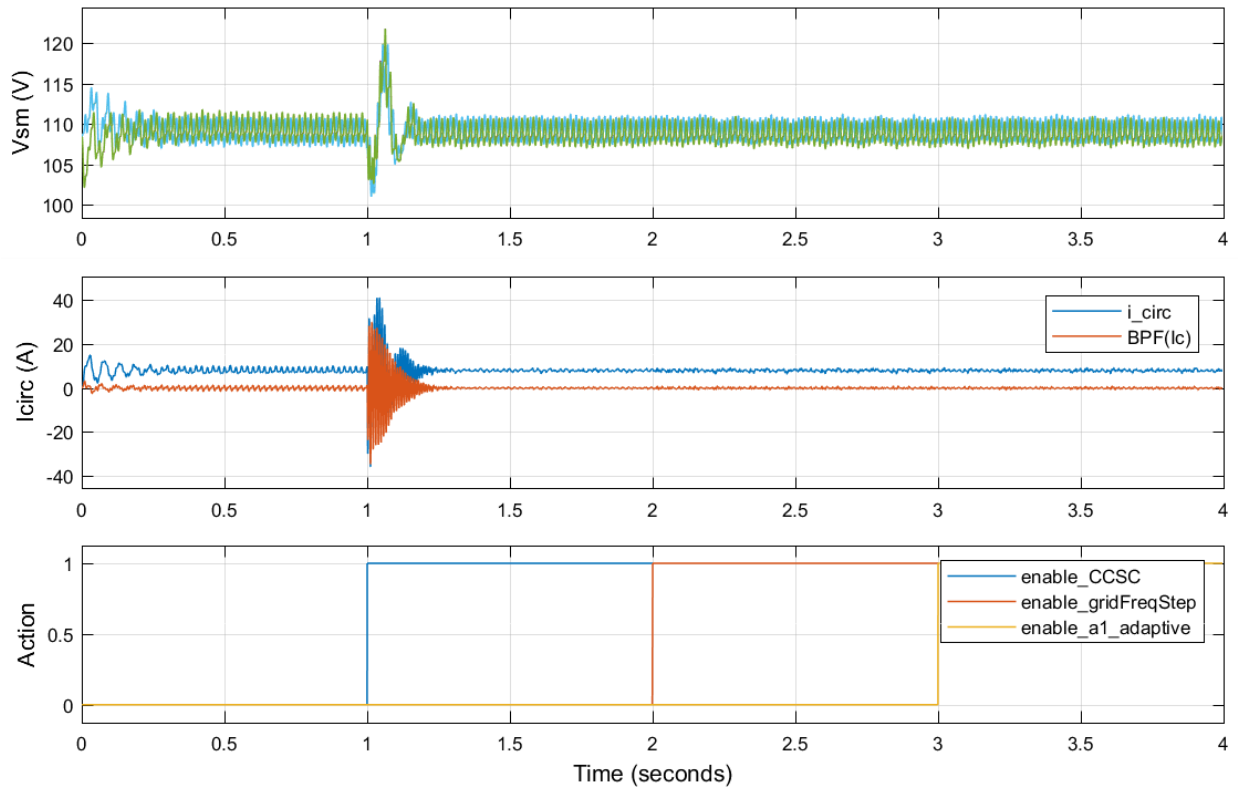
KP = 2.04 AND KR= 1,036.1

Figure 5.11 Adaptive ω_0 - Overview of submodule voltages, the bandpass filtered and ordinary circulating current and actions at different times with the controller gain set to K_P=2.04 and K_R=1,036.1.

In the time interval of $2.2 \leq t \leq 3.0$ in Figure 5.11, the circulating current was measured to 7.982 A, the bandpass filtered circulating current BPF(I_{circ}) = 3.50E-1 A and the error was measured to 5.10E-1 A. This yields the ratio BPF(I_{circ})/I_{circ} to become 4.38 %.

After activation of the adaptive controller at t = 3.0 seconds, the following values were recorded in the period of $3.2 \leq t \leq 4.0$. The circulating current was recorded to 7.975A, the bandpass filtered circulating current BPF(I_{circ}) = 3.21E-1 A and the error was measured to 4.64E-1 A. This yields the ratio BPF(I_{circ})/I_{circ} to become 4.03 %.

The same observation about proportional gain and settling time is also made here.
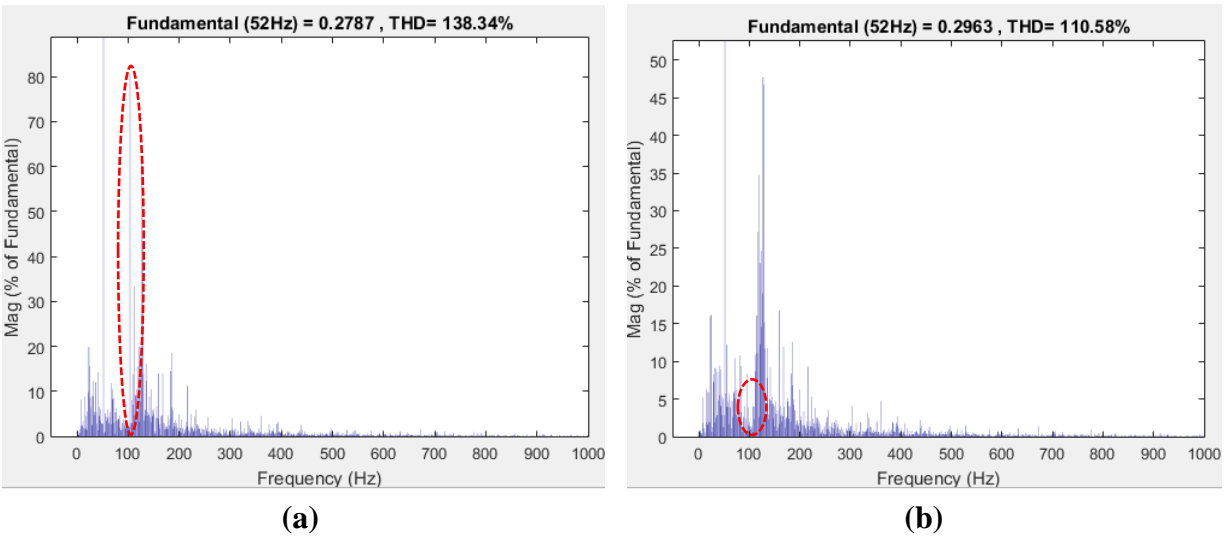
Figure 5.12 Adaptive ω_0 - harmonic spectrum with use of the circulating current, where **(a)** shows the non-adaptive controller in the period of $2.2 \leq t \leq 3.0$, and **(b)** shows the adaptive controller in the period of $3.2 \leq t \leq 4.0$.

Figure 5.12 shows the total harmonic distortion in the circulating current. The THD decreased from 138.34 % to 110.58 % and the second harmonic component, which is circled out in red, decreased from 80.58 % to 1.40 % after activation of the adaptive controller.
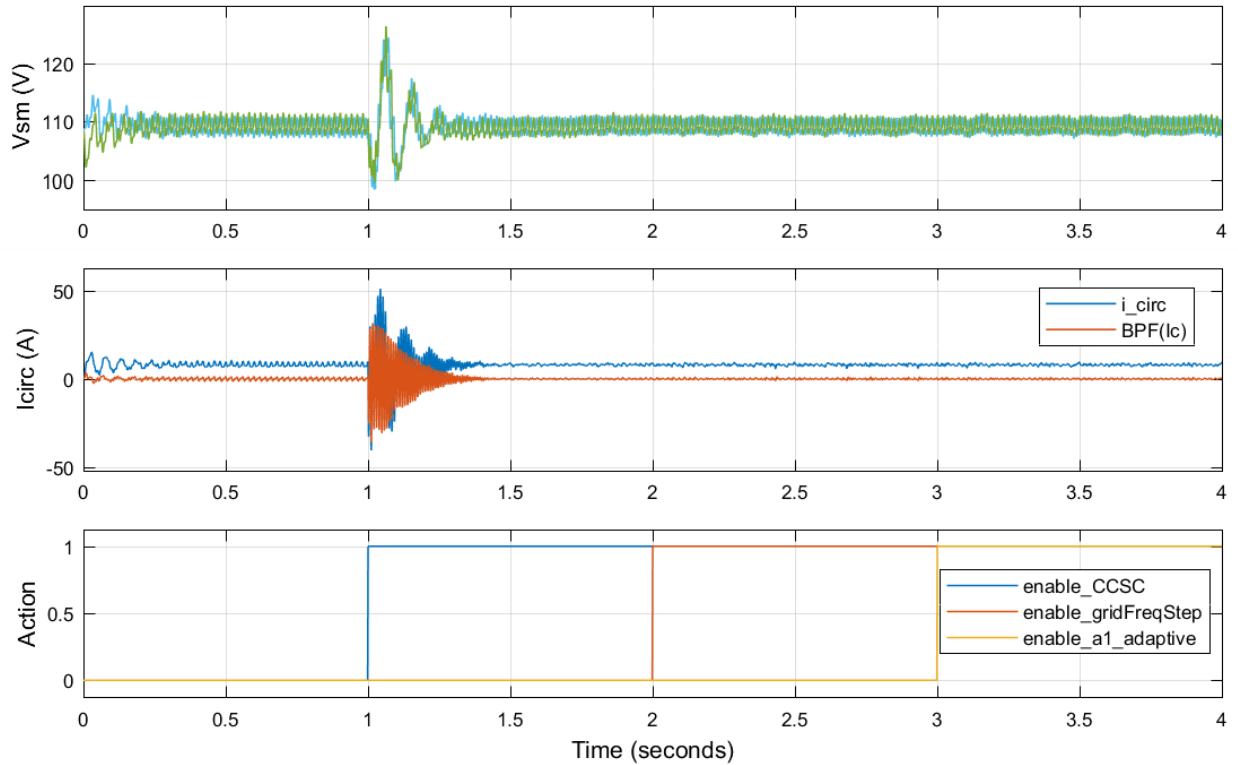
Kp = 1.04 and Kr = 1,036.1

Figure 5.13 Adaptive ω_0 - Overview of submodule voltages, the bandpass filtered and ordinary circulating current and actions at different times with the controller gain set to K_P=1.04 and K_R=1,036.1.

In the time interval of $2.2 \leq t \leq 3.0$ in Figure 5.13, the circulating current was measured to 7.975A, the bandpass filtered circulating current BPF(I_{circ}) = 3.86E-1 A and the error was measured to 5.58E-1 A. This yields the ratio BPF(I_{circ})/I_{circ} to become 4.85 %.

After activation of the adaptive controller at t = 3.0 seconds, the following values were recorded in the period of $3.2 \leq t \leq 4.0$. The circulating current was recorded to 7.981 A, the bandpass filtered circulating current BPF(I_{circ}) = 3.30E-1 A and the error was measured to 4.99E-1 A. This yields the ratio BPF(I_{circ})/I_{circ} to become 4.37 %.

Now, the settling time is almost 0.3 seconds. The system is operating with a low bandwidth, which means that even a small disturbance might get the system unstable. In this simulation, the PLL-block has a ramp equivalent to 0.1s/Hz when measuring the frequency. However, if the grid frequency instantaneously changed, which could originate from a sudden grid outage, the controller could go unstable.

(a)   **(b)**
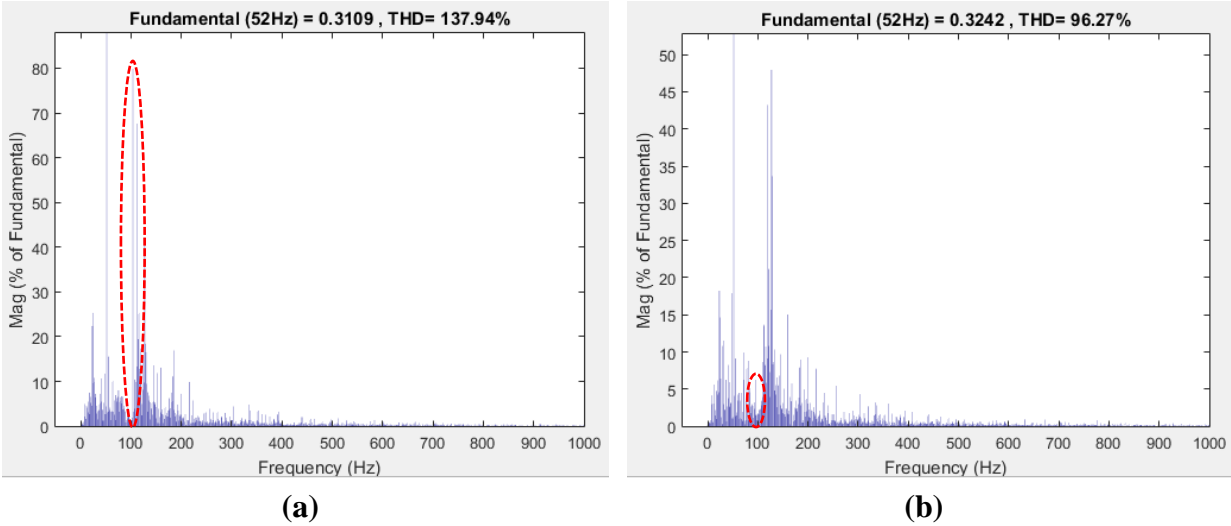
Figure 5.14 Adaptive ω_0 - harmonic spectrum with use of the circulating current, where **(a)** shows the non-adaptive controller in the period of $2.2 \leq t \leq 3.0$, and **(b)** shows the adaptive controller in the period of $3.2 \leq t \leq 4.0$.

Figure 5.14 shows the total harmonic distortion. The THD decreased from 153.09 % to 96.27 % and the second harmonic component, which is circled out in red, decreased from 79.88 % to 2.28 % after the adaptive controller was activated.

SUMMARY OF SIMULATION RESULTS

Suppression of the $2\omega_0$ component of the circulating current using the adaptive ω_0 controller has proven to work with high efficiency. As summarised in Table 5.2, most second harmonics have been suppressed with a percentage ranging from 97.15 to 98.93 % of its original value.

Table 5.2 Adaptive ω_0 - summary of the results when activating the circulating current controller with adaptive ω_0.

K_P	K_R	Time (s)	$I_{c,rms}$			**FFT** (% of f_0)	
			(A)	BPF (A)	Error (A)	THD	$2f_0$
40.72	16,577	$2.2 \leq t \leq 3.0$	7.91	7.72E-2	1.59E-1	63.17	9.97
		$3.2 \leq t \leq 4.0$	7.92	7.88E-2	1.61E-1	58.85	0.39
20.36	4,144.3	$2.2 \leq t \leq 3.0$	7.94	1.23E-1	2.06E-1	76.11	31.41
		$3.2 \leq t \leq 4.0$	7.95	1.36E-1	2.26E-1	54.3	0.41
10.23	1,036.1	$2.2 \leq t \leq 3.0$	7.95	2.14E-1	2.86E-1	165.40	130.70
		$3.2 \leq t \leq 4.0$	7.96	1.58E-1	2.50E-1	80.69	1.63
5.06	1,036.1	$2.2 \leq t \leq 3.0$	8.00	3.14E-1	4.44E-1	103.09	72.60
		$3.2 \leq t \leq 4.0$	8.01	2.81E-1	4.30E-1	59.87	0.78
2.04	1,036.1	$2.2 \leq t \leq 3.0$	7.98	3.50E-1	5.10E-1	138.32	80.58
		$3.2 \leq t \leq 4.0$	7.98	3.21E-1	4.64E-1	110.58	1.40
1.04	1,036.1	$2.2 \leq t \leq 3.0$	7.98	3.86E-1	5.58E-1	137.94	79.88
		$3.2 \leq t \leq 4.0$	7.98	3.30E-1	4.99E-1	96.27	2.28

Based on the summarised results in Table 5.2, the circulating current deviates from its reference value. Also, the submodule voltages deviate from its reference value of V_{dc}/N. This could have been prevented by implementation of an arm energy controller. Section 3.4 demonstrated that both the sum and delta controller was able to counter the effects of unbalanced submodule voltage by injecting a dc and fundamental current into the circulating current controller. Though, this extra fundamental current could influence the circulating current with nebulous effect. The scope of this thesis is the adaptive controller's effect. Therefore, satisfying results were obtained by leaving out the arm energy controller.

5.2   Adaptive Sampling Time

Much of the same argumentation used in section 4.3 to describe the phenomena of the governing dynamics of the converter can also be used in this section.

Most of the graphs shown in this section are very similar to the graphs in section 5.1 as there is only a marginal difference between the two adaptive methods. Though, minor differences are expected to be observed using FFT analysis. Comments will therefore only be given if there are significant exceptions to prevent any prevent any repetitive arguments.

KP = 40.72 AND KR = 16,577
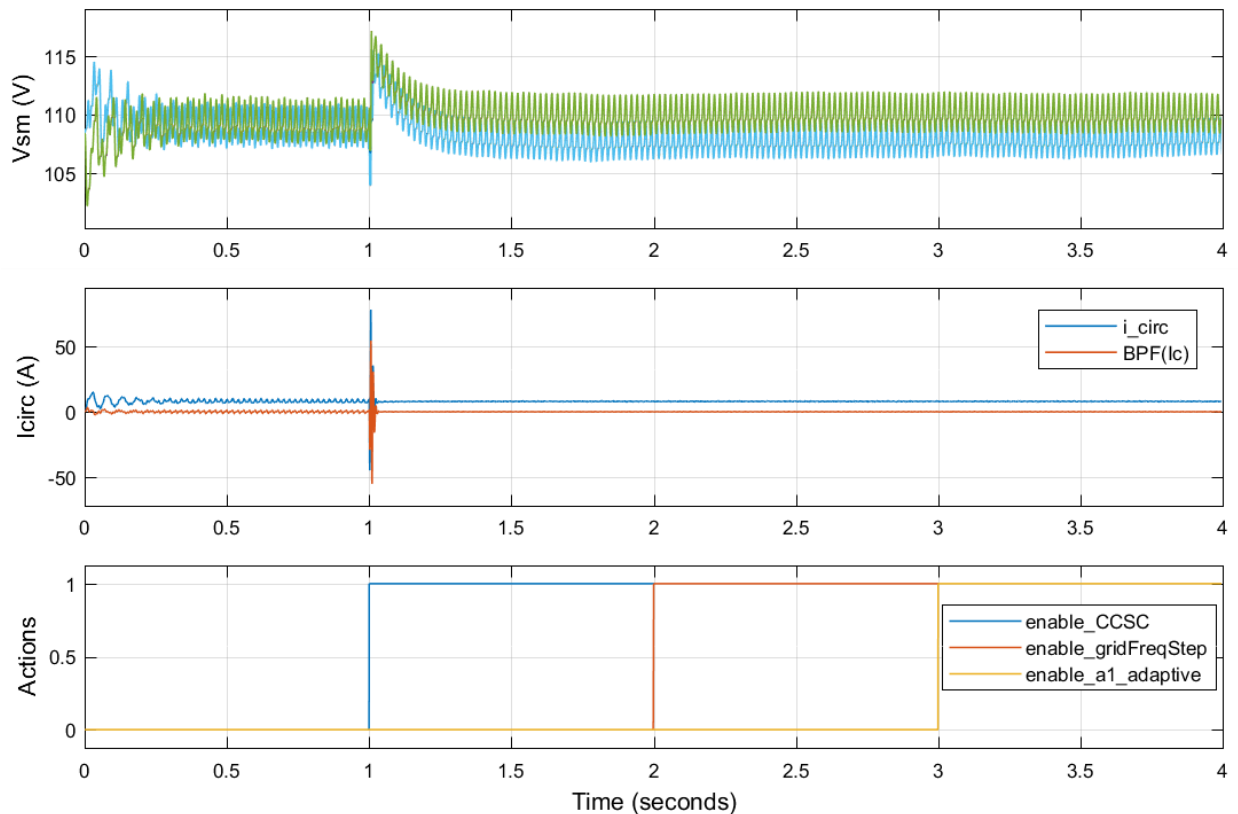
Figure 5.15 Adaptive T_s - overview of submodule voltages, the bandpass filtered and original circulating current and actions at different times with the controller gain set to K_P=40.7 and K_R=16,577

In the time interval of $2.2 \leq t \leq 3.0$ in Figure 5.15, the circulating current was measured to 7.919 A, the bandpass filtered circulating current $BPF(I_{circ}) = 7.82E\text{-}2$ A and the error was measured to 1.59E-1 A. This yields the ratio $BPF(I_{circ})/I_{circ}$ to become 0.987 %.

After activation of the adaptive controller at t = 3.0 seconds, the following values were recorded in the period of $3.2 \leq t \leq 4.0$. The circulating current was recorded to 7.917 A, the bandpass filtered circulating current $BPF(I_{circ}) = 8.95E\text{-}2$ A and the error was measured to 1.61E-1 A. This yields the ratio $BPF(I_{circ})/I_{circ}$ to become 1.13 %.

(a)   (b)
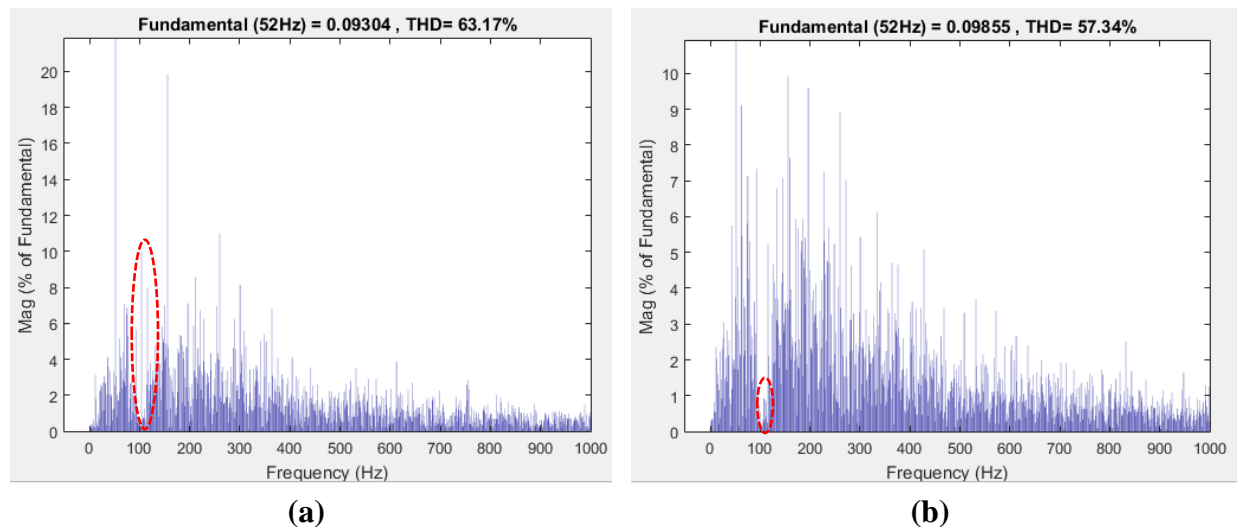
Figure 5.16 Adaptive T_s – harmonic spectrum with use of the circulating current, where **(a)** shows the non-adaptive controller in the period of $2.2 \leq t \leq 3.0$, and **(b)** shows the adaptive controller in the period of $3.2 \leq t \leq 4.0$.

Figure 5.16 shows the total harmonic distortion in the circulating current. The THD decreased from 63.17 % to 57.34 % and the second harmonic component, which is circled in red, decreased from 9.97 % to 0.19 % after activation of the adaptive controller.

KP = 20.4 AND KR = 4144.3
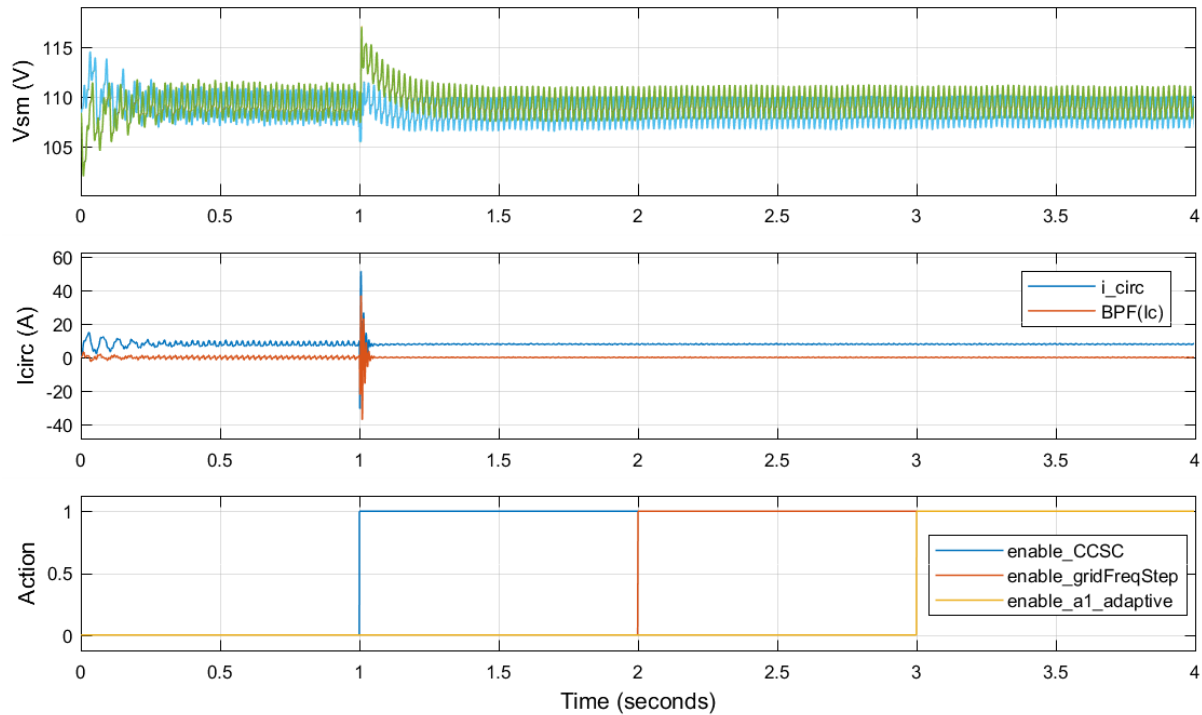
Figure 5.17 Adaptive T_s - overview of submodule voltages, the bandpass filtered and original circulating current and actions at different times with the controller gain set to K_P=20.4 and K_R=4,144.3

In the time interval of $2.2 \leq t \leq 3.0$ in Figure 5.17, the circulating current was measured to 7.938 A, the bandpass filtered circulating current BPF(I_{circ}) = 1.23E-2 A and the error was measured to 2.06E-1 A. This yields the ratio BPF(I_{circ})/I_{circ} to become 1.55 %.

After activation of the adaptive controller at t = 3.0 seconds, the following values were recorded in the period of $3.2 \leq t \leq 4.0$. The circulating current was recorded to 7.945 A, the bandpass filtered circulating current BPF(I_{circ}) = 1.24E-2 A and the error was measured to 2.10E-1 A. This yields the ratio BPF(I_{circ})/I_{circ} to become 1.57 %.
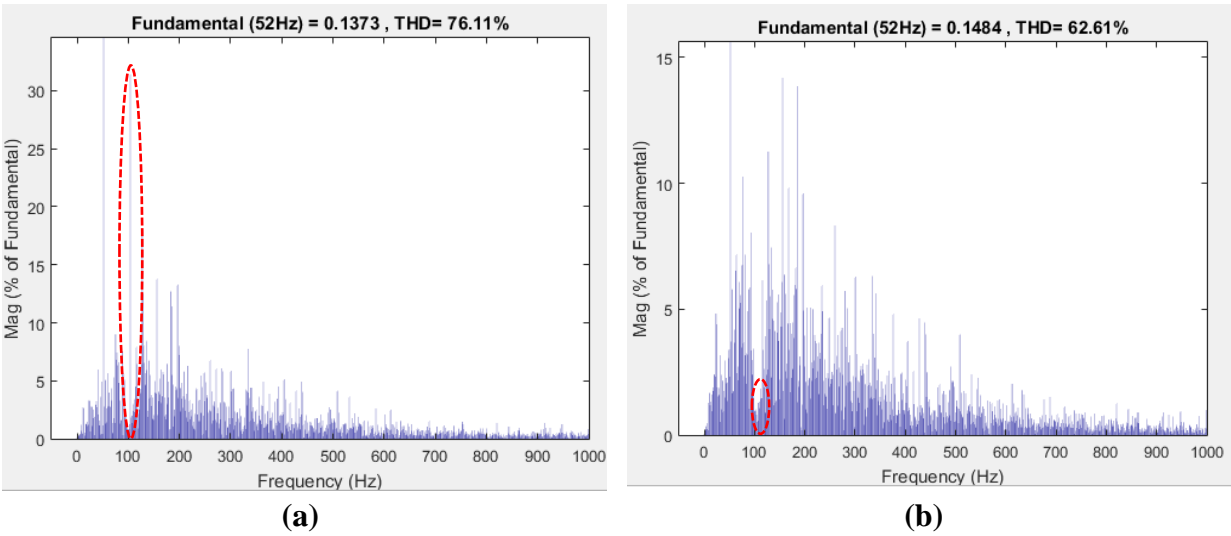
Figure 5.18 Adaptive T_s - harmonic spectrum with use of the circulating current, where **(a)** shows the non-adaptive controller in the period of $2.2 \leq t \leq 3.0$, and **(b)** shows the adaptive controller in the period of $3.2 \leq t \leq 4.0$.

Figure 5.18 shows the total harmonic distortion in the circulating current. The THD decreased from 76.11 % to 62.61 % and the second harmonic component, which is circled in red, decreased from 31.41 % to 0.81 % after the adaptive controller was activated.

K$_P$ = 10.18 AND K$_R$ = 1,036.1
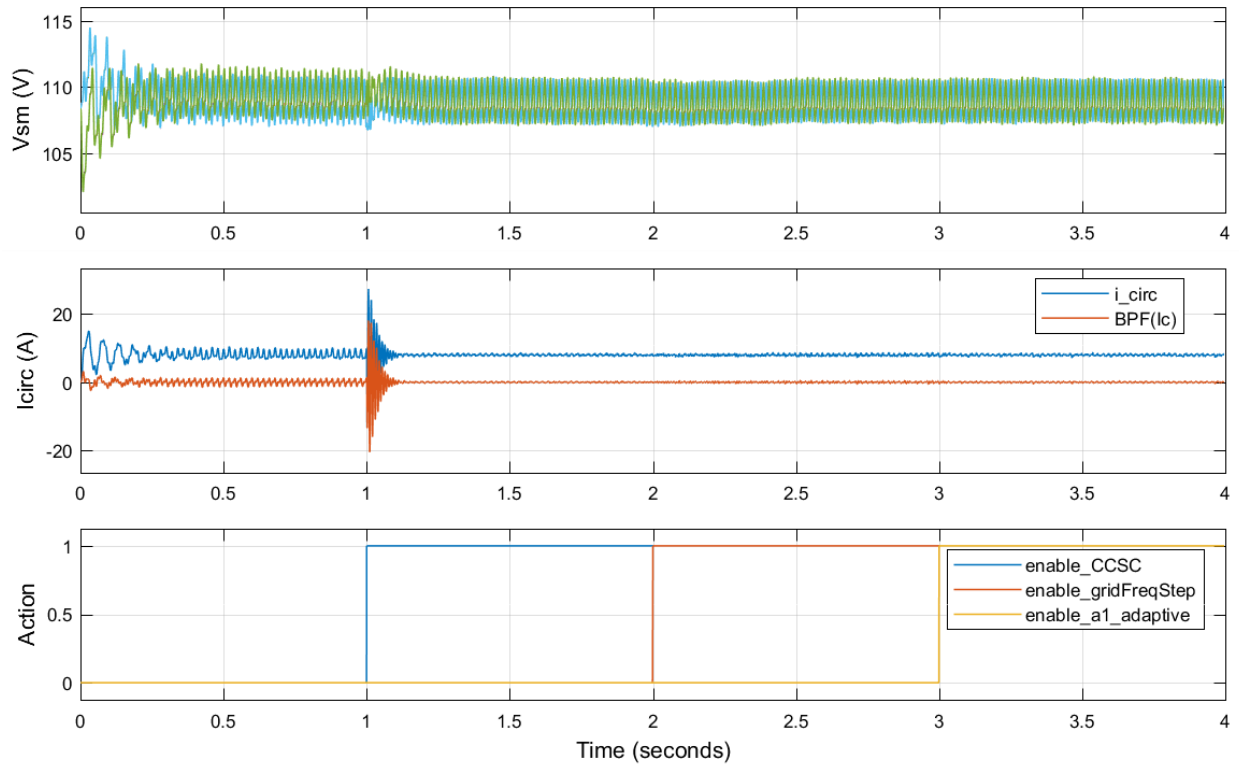
Figure 5.19 Adaptive T_s - overview of submodule voltages, the bandpass filtered and original circulating current and actions at different times with the controller gain set to K_P=10.23 and K_R=1,036.1

In the time interval of $2.2 \leq t \leq 3.0$ in Figure 5.19, the circulating current was measured to 7.953 A, the bandpass filtered circulating current measured to BPF(I_{circ}) = 2.14E-1 A and the error was measured to 2.86E-1 A. This yields the ratio BPF(I_{circ})/I_{circ} to become 2.63 %.

After activation of the adaptive controller at t = 3.0 seconds, the following values were recorded in the period of $3.2 \leq t \leq 4.0$. The circulating current was recorded to 7.954 A, the bandpass filtered circulating current BPF(I_{circ}) = 1.57E-1 A and the error was measured to 2.48E-1 A. This yields the ratio BPF(I_{circ})/I_{circ} to become 1.97 %.
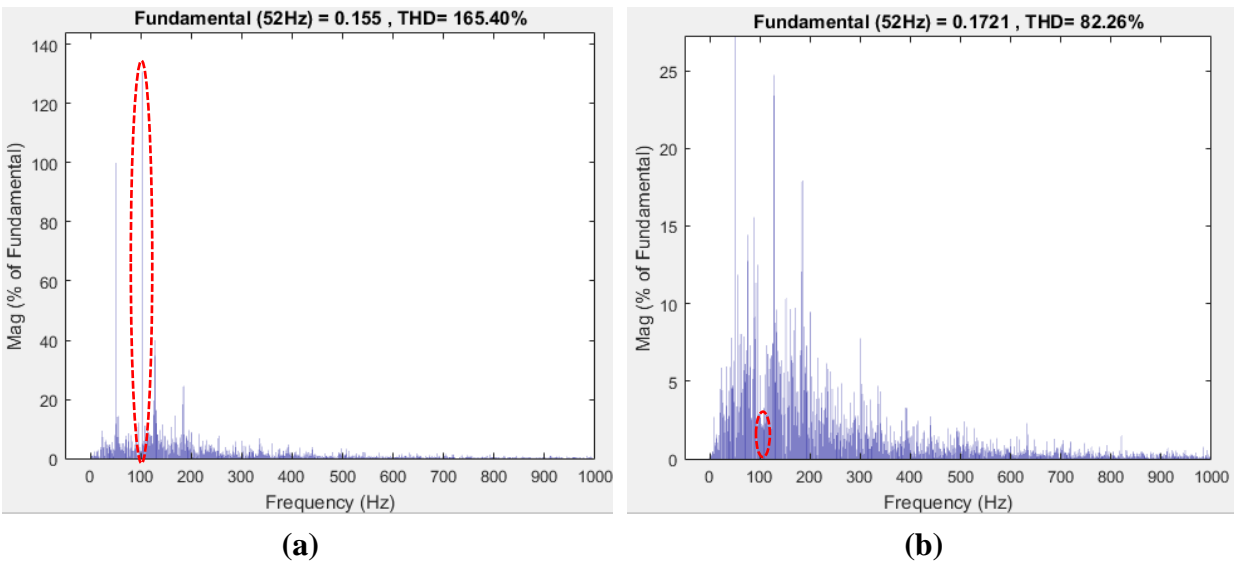
Figure 5.20 Adaptive T_s - harmonic spectrum with use of the circulating current, where **(a)** shows the non-adaptive controller in the period of $2.2 \leq t \leq 3.0$, and **(b)** shows the adaptive controller in the period of $3.2 \leq t \leq 4.0$.

Figure 5.18 shows the total harmonic distortion in the circulating current. The THD decreased from 165.40 % to 82.26 % and the second harmonic component, which is circled in red, decreased from 130.70 % to 2.05 % after activation of the adaptive controller.

K_P = 5.09 AND K_R = 1036.1
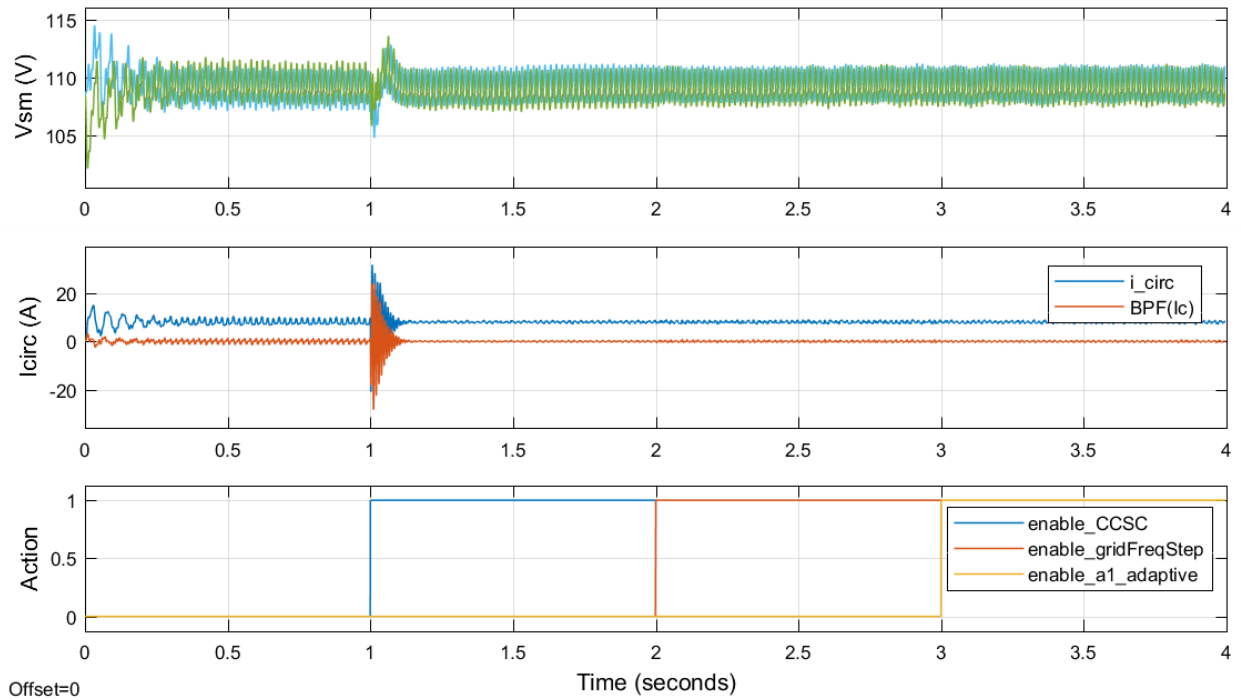
Figure 5.21 Adaptive T_s - overview of submodule voltages, the bandpass filtered and ordinary circulating current and actions at different times with the controller gain set to K_P=5.06 and K_R=1,036.1.

In the time interval of $2.2 \le t \le 3.0$ in Figure 5.21, the circulating current was measured to 8.00 A, the bandpass filtered circulating current BPF(I_{circ}) = 3.14E-1 A and the error was measured to 4.44E-1 A. This yields the ratio BPF(I_{circ})/I_{circ} to become 3.93 %.

After activation of the adaptive controller at t = 3.0 seconds, the following values were recorded in the period of $3.2 \le t \le 4.0$. The circulating current was recorded to 8.00 A, the bandpass filtered circulating current BPF(I_{circ}) = 2.74E-1 A and the error was measured to 4.16E-1 A. This yields the ratio BPF(I_{circ})/I_{circ} to become 3.43 %.
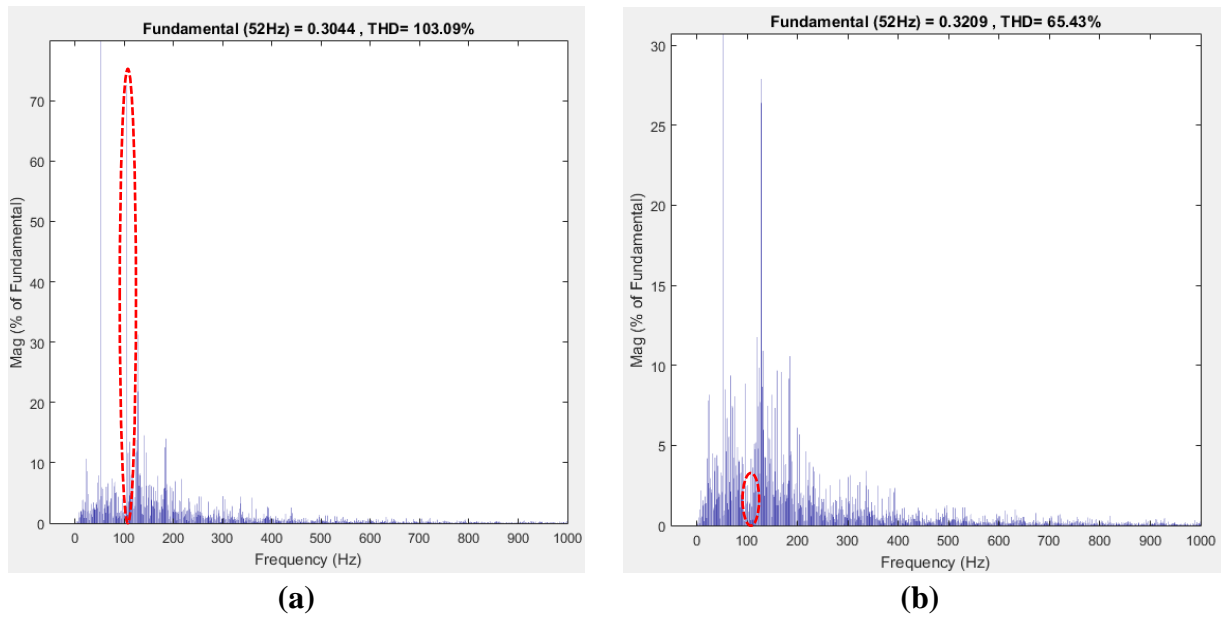
Figure 5.22 Adaptive T_s - harmonic spectrum with use of the circulating current, where **(a)** shows the non-adaptive controller in the period of $2.2 \leq t \leq 3.0$, and **(b)** shows the adaptive controller in the period of $3.2 \leq t \leq 4.0$.

Figure 5.22 shows the total harmonic distortion in the circulating current. The THD decreased from 103.09 % to 59.87 % and the second harmonic component, which is circled in red, decreased from 72.60 % to 0.78 % after the adaptive controller was activated.
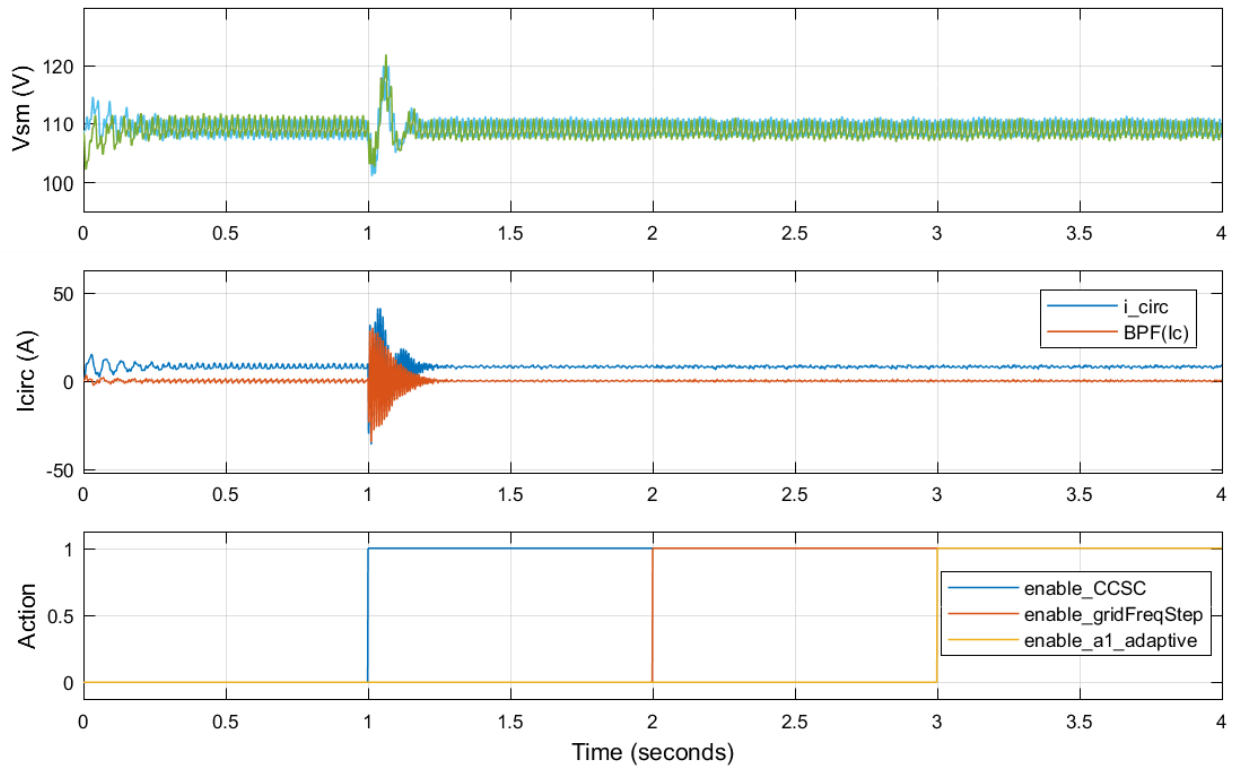
KP = 2.04 AND KR = 1036.1

Figure 5.23 Adaptive T_s - overview of submodule voltages, the bandpass filtered and ordinary circulating current and actions at different times with the controller gain set to K_P=2.04 and K_R=1,036.1.

In the time interval of $2.2 \leq t \leq 3.0$ in Figure 5.23, the circulating current was measured to 7.982A, the bandpass filtered circulating current BPF(I_{circ}) = 3.51E-1 A and the error was measured to 5.10E-1 A. This yields the ratio BPF(I_{circ})/I_{circ} to become 4.38 %.

After activation of the adaptive controller at t = 3.0 seconds, the following values were recorded in the period of $3.2 \leq t \leq 4.0$. The circulating current was recorded to 7.976 A, the bandpass filtered circulating current BPF(I_{circ}) = 3.21E-1 A and the error was measured to 4.70E-1 A. This yields the ratio BPF(I_{circ})/I_{circ} to become 4.03 %.
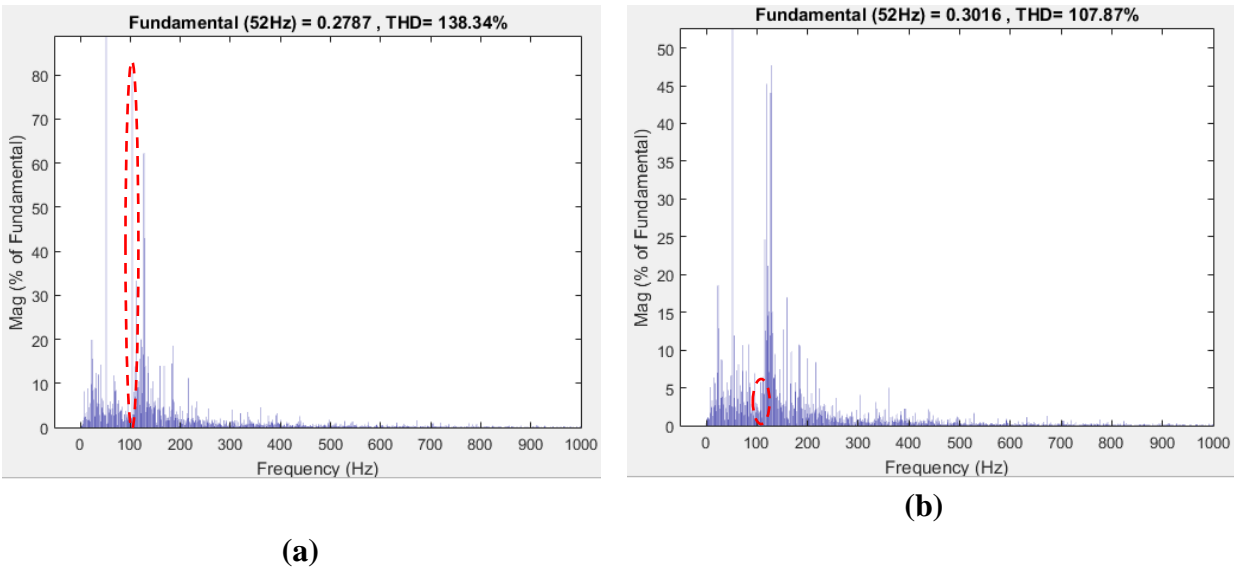
Figure 5.24 Adaptive T_s - harmonic spectrum with use of the circulating current, where **(a)** shows the non-adaptive controller in the period of $2.2 \leq t \leq 3.0$, and **(b)** shows the adaptive controller in the period of $3.2 \leq t \leq 4.0$.

Figure 5.24 shows the total harmonic distortion in the circulating current. The THD decreased from 138.34 % to 107.87 % and the second harmonic component, which is circled in red, decreased from 80.58 % to 1.71 % after activation of the adaptive controller.
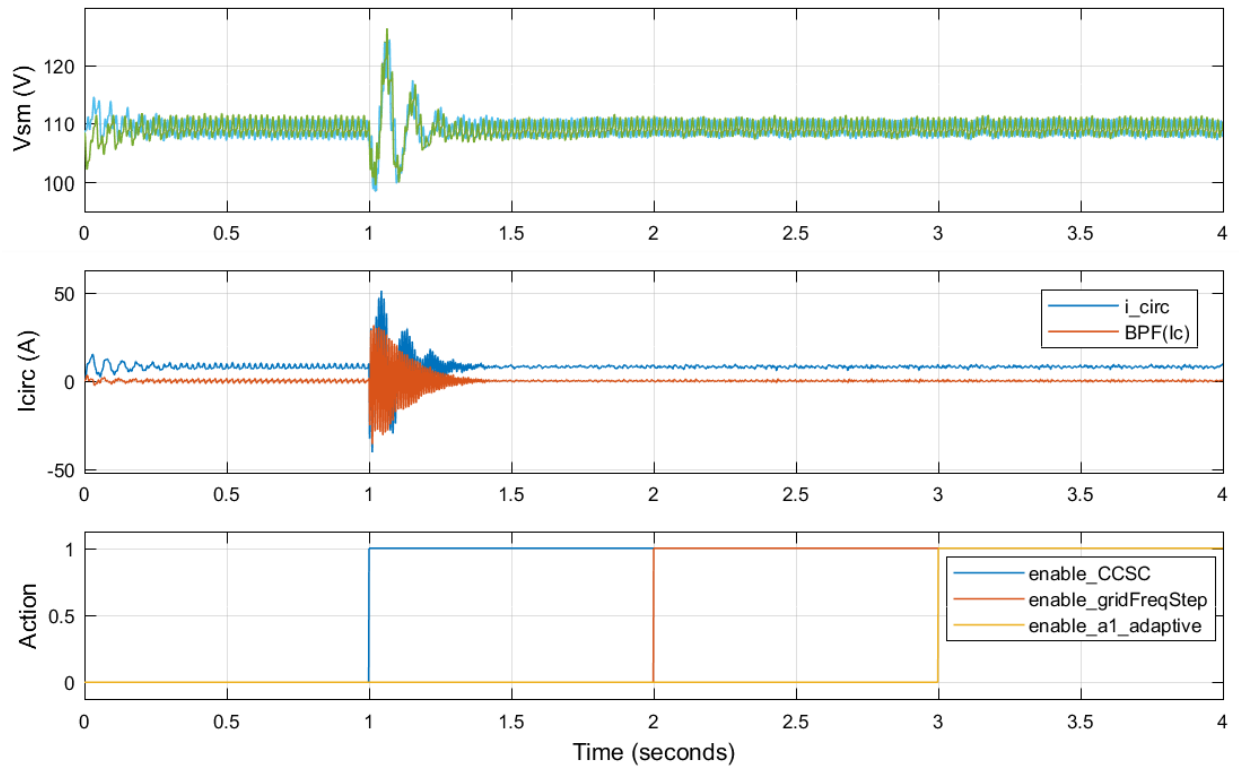
KP = 1.04 AND KR = 1036.1

Figure 5.25 Adaptive T_s - overview of submodule voltages, the bandpass filtered and ordinary circulating current and actions at different times with the controller gain set to K_P=1.04 and K_R=1,036.1.

In the time interval of $2.2 \leq t \leq 3.0$ in Figure 5.25, the circulating current was measured to 7.975 A, the bandpass filtered circulating current BPF(I_{circ}) = 3.86E-1 A and the error was measured to 5.58E-1 A. This yields the ratio BPF(I_{circ})/I_{circ} to become 4.85 %.

After activation of the adaptive controller at t = 3.0 seconds, the following values were recorded in the period of $3.2 \leq t \leq 4.0$. The circulating current was recorded to 7.989 A, the bandpass filtered circulating current BPF(I_{circ}) = 3.49E-1 A and the error was measured to 5.14E-1 A. This yields the ratio BPF(I_{circ})/I_{circ} to become 4.37 %.
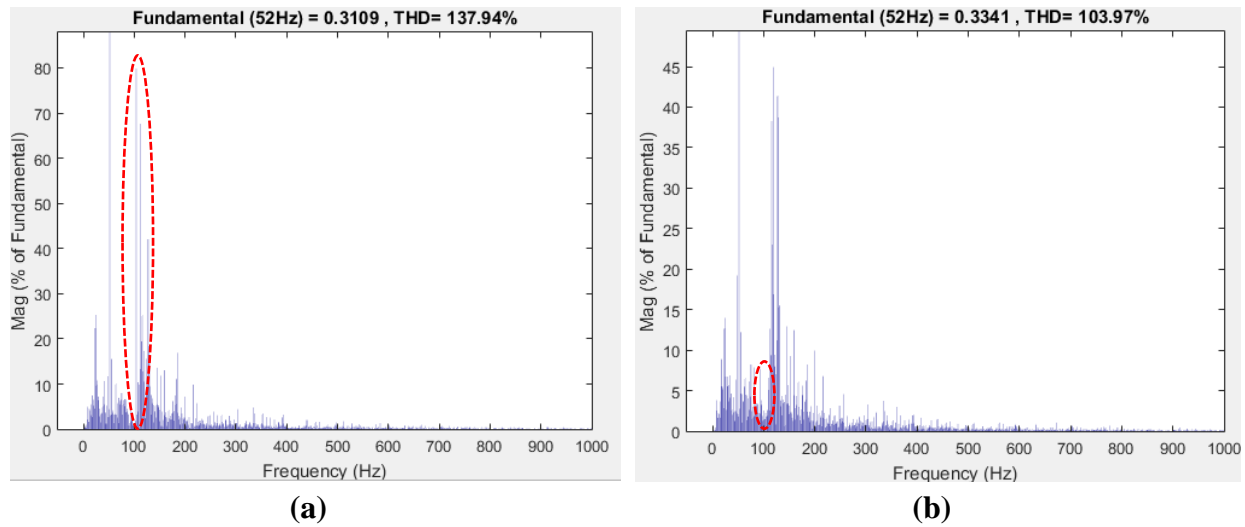
Figure 5.26 Adaptive T_s - harmonic spectrum with use of the circulating current, where **(a)** shows the non-adaptive controller in the period of $2.2 \leq t \leq 3.0$, and **(b)** shows the adaptive controller in the period of $3.2 \leq t \leq 4.0$.

Figure 5.26 shows the total harmonic distortion in the circulating current. The THD decreased from 137.94 % to 103.97 % and the second harmonic component, which is circled in red, decreased from 79.88 % to 2.31 % after activation of the adaptive controller.

SUMMARY OF SIMULATION RESULTS

Simulations show that the adaptive T_s method is also very effective at suppressing the $2\omega_0$ component of the circulating current. The adaptive T_s controller was able to suppress the second harmonic component with a percentage ranging from 96.8 to 98.01 % compared to its original value.

Table 5.3 Results when activating the circulating current controller with adaptive T_s.

K_P	K_R	Time (s)	$I_{c,rms}$			FFT (% of f_0)	
			(A)	BPF (A)	Error (A)	THD	$2f_0$
40.72	16,577	$2.2 \leq t \leq 3.0$	7.92	7.82E-1	1.59E-1	63.17	9.97
		$3.2 \leq t \leq 4.0$	7.92	8.95E-2	1.61E-1	57.34	0.19
20.36	4144.3	$2.2 \leq t \leq 3.0$	7.94	1.23E-1	2.06E-1	76.11	31.41
		$3.2 \leq t \leq 4.0$	7.95	1.24E-1	2.10E-1	62.61	0.81
10.23	1036.1	$2.2 \leq t \leq 3.0$	7.95	2.14E-1	2.86E-1	165.40	130.70
		$3.2 \leq t \leq 4.0$	7.95	1.57E-1	2.48E-1	82.26	2.05
5.09	1036.1	$2.2 \leq t \leq 3.0$	8.01	3.14E-1	4.44E-1	103.09	65.43
		$3.2 \leq t \leq 4.0$	8.00	2.74E-1	4.16E-1	65.43	1.31
2.05	1036.1	$2.2 \leq t \leq 3.0$	7.98	3.50E-1	5.10E-1	138.34	80.58
		$3.2 \leq t \leq 4.0$	7.98	3.21E-1	4.70E-1	107.87	1.71
1.35	1036.1	$2.2 \leq t \leq 3.0$	7.98	3.86E-1	5.58E-1	137.94	79.88
		$3.2 \leq t \leq 4.0$	7.99	3.49E-1	5.14E-1	103.97	2.31

5.3   Comparison of the Adaptive Proportional Resonant Controllers

Table 5.4 compares the results from the two controllers obtained in the time interval of $3.2 \leq t \leq 4.0$.

Table 5.4 Overview of the results from the adaptive ω_0 and T_s.

K_P	K_R	Adaptive Controller	$I_{c,rms}$			**FFT** (% of f_0)		**Comparison**
			(A)	BPF (A)	Error (A)	THD	$2f_0$	$T_s^{2f_0}/\omega_0^{2f_0}$ (%)
40.72	16,577	ω_0	7.92	7.88E-2	1.61E-1	58.85	0.39	48.71
		T_s	7.92	8.95E-2	1.61E-1	57.34	0.19	
20.38	4144.3	ω_0	7.95	1.36E-1	2.26E-1	54.3	0.41	197.56
		T_s	7.95	1.24E-1	2.10E-1	62.61	0.81	
10.23	1036.1	ω_0	7.96	1.58E-1	2.50E-1	80.69	1.63	125.77
		T_s	7.95	1.57E-1	2.48E-1	82.26	2.05	
5.06	1036.1	ω_0	8.01	2.81E-1	4.30E-1	59.87	0.78	167.95
		T_s	8.00	2.74E-1	4.16E-1	65.43	1.31	
2.04	1036.1	ω_0	7.98	3.21E-1	4.64E-1	110.58	1.40	122.14
		T_s	7.98	3.21E-1	4.70E-1	107.87	1.71	
1.04	1036.1	ω_0	7.98	3.30E-1	4.99E-1	96.27	2.28	101.32
		T_s	7.99	3.49E-1	5.14E-1	103.97	2.31	

The following observations can be made based on the results in Table 5.4

- Both methods manage to suppress the second harmonic component with high efficiency during grid fluctuations
- Overall, the adaptive ω_0 is slightly better at suppressing the second harmonic component compared to the adaptive T_s. Especially at medium and low bandwidth systems, it becomes evident that the adaptive ω_0 is more efficient. The last column of Table 5.4, show that the adaptive T_s resulted in a significantly higher second harmonic for all bandwidths except the original tuned adaptive ω_0.
- The adaptive T_s is more efficient at the original tuned PR controller. In comparison, the adaptive T_s resulted in a 48.71 % lower second harmonic component compared to the adaptive ω_0.

Chapter 6

This section concludes the master thesis. Further work for what can be done to get more better results is also presented.

6 Conclusion and Further Work

6.1 Conclusion

Analytical study of the internal behaviour in a modular multilevel converter has been undertaken. It was shown that the circulating current contains multiple harmonics of the fundamental frequency, especially the second harmonic component dominates the harmonic frequency spectrum. It is desired to have purely dc circulating current as other harmonics contribute to higher power losses and additional electric stress to passive components and semiconductor devices.

In real systems, it is likely that the fundamental frequency will change due to load- or generation variations. In terms of the second harmonic, a change of 2 Hz in the fundamental frequency will result in a change of 4 Hz in the circulating current's second harmonic. As seen in previous Bode plots, the gain reduces significantly outside the resonant peak. Therefore, the needed for a frequency adaptive controller is highly necessary.

Analysis of the circulating current's behaviour during changes of the fundamental frequency was carried out. Two digital, adaptive controllers proposed in [1] and [2] have been presented and compared under high, mid and low bandwidth systems. In terms of suppression of the second harmonic component, the simulation results led to the following conclusions:

- The adaptive T_s yielded better results for the high bandwidth converter.
- Over most bandwidths, the adaptive ω_0 performed slightly better than the adaptive T_s. Especially in medium and low bandwidth systems, the adaptive ω_0 yielded better results. Comparing the two against each other, the ω_0's performance gave 20.49 %, 67.95 % and 22.14 % lower second harmonic component for the following respective proportional gains 10.18, 5.06 and 2.04.

Based on the simulation study, the controller proposed in [1] yields better results than the [2] in medium and low bandwidth systems. Hence, the adaptive controller proposed in [1] be the desired controller.

6.2   Further Work

Although the simulated system with the two adaptive controllers functioned as supposed, several improvements could further enhance the results. The following suggestions could be implemented to get a more comprehensive understanding of the control methods.

- Investigate and evaluate the challenges in implementation in processors such as the DSP and the FPGA.
- Both methods require a PLL in order to work. However, the PLL in itself is not truly adaptive. Therefore, the performance of [1] and [2] with dynamics of the PLL needs to be studied.

In terms of the simulation model, this thesis has utilised a modular multilevel converter with some limitations. The simulations were run in a system where the opposing grid voltage was set to zero. This thesis focused on the effect of the two methods suppressing the second harmonic component of the circulating current. The following additional features would enhance the robustness of the simulated converter

- Implementation of an arm energy controller can be added to ensure that the average submodule voltage circulates around the reference value. In doing so, the additional circulating current would not be present as the voltage difference between the upper and lower arm would not be the source for this extra balancing current.
- Adding an output current controller in combination with a grid voltage would improve the stability of the MMC.
- Implementation of a series harmonic controller or a repetitive controller to suppress other harmonics in addition to the second harmonic. The FFT analyses in chapter 5 revealed several harmonics in the system. Expanding the digital controller to suppress other harmonics as well would reduce the circulating current, and consequently lower the losses inside the converter.

Bibliography

[1]   A. B. Acharya, L. Norum, S. D., and R. Teodorescu, "Frequency Adaptive Digital FIlter Implementation of Proportional-Resonant COntroller for Inverter Applications," 2018.

[2]   S. A. Khajehoddin, M. Karimi-Ghartemani, P. Jain, and A. Bakhshai, "A frequency adaptive resonant controller for fixed point digital implementation at high sampling frequency," in *2011 IEEE Energy Conversion Congress and Exposition*, 2011, pp. 2557-2561.

[3]   N. Ahmed, A. Haider, D. V. Hertem, L. Zhang, and H. P. Nee, "Prospects and challenges of future HVDC SuperGrids with modular multilevel converters," in *Proceedings of the 2011 14th European Conference on Power Electronics and Applications*, 2011, pp. 1-10.

[4]   E. Tedeschi, "Lecture 3," *ELK-23: Power Electronics in Future Power Systems,* Lecture 11/09/17 2017.

[5]   A. Lesnicar and R. Marquardt, "An innovative modular multilevel converter topology suitable for a wide power range," in *2003 IEEE Bologna Power Tech Conference Proceedings*, 2003, vol. 3, p. 6 pp. Vol.3.

[6]   S. Debnath, J. Qin, B. Bahrani, M. Saeedifard, and P. Barbosa, "Operation, Control, and Applications of the Modular Multilevel Converter: A Review," *IEEE Transactions on Power Electronics,* vol. 30, no. 1, pp. 37-53, 2015.

[7]   A. Beddard and M. Barnes, "Modelling of MMC-HVDC Systems – An Overview," *Energy Procedia,* vol. 80, pp. 201-212, 2015.

[8]   H. R. Parikh and R. S. Martin-Loches, "Control of Modular Multilevel Converter (MMC) based HVDC Application under Unbalanced Conditions," Master, Energy Technology, Aalborg University, 2016.

[9]   W. Yang, Q. Song, S. Xu, H. Rao, and W. Liu, "A MMC Topology Based on Unidirectional Current H-Bridge Sub-Module with Active Circuiting Current Injection," *IEEE Transactions on Power Electronics,* pp. 1-1, 2017.

[10]   K. Wang, Y. Li, Z. Zheng, and L. Xu, "Voltage Balancing and Fluctuation-Suppression Methods of Floating Capacitors in a New Modular Multilevel Converter," *IEEE Transactions on Industrial Electronics,* vol. 60, no. 5, pp. 1943-1954, 2013.

[11]   L. He, K. Zhang, J. Xiong, S. Fan, and Y. Xue, "Low-Frequency Ripple Suppression for Medium-Voltage Drives Using Modular Multilevel Converter With Full-Bridge Submodules," *IEEE Journal of Emerging and Selected Topics in Power Electronics,* vol. 4, no. 2, pp. 657-667, 2016.

[12]   L. He, K. Zhang, J. Xiong, S. Fan, and Y. Xue, "Modular multilevel converter with full-bridge submodules and improved low-frequency ripple suppression for medium-voltage drives," in *2015 IEEE Applied Power Electronics Conference and Exposition (APEC)*, 2015, pp. 2288-2294.

[13]   K. Sharifabadi, L. Harnefors, H.-P. Nee, S. Norrga, and R. Teodorescu, "Dynamics and Control," in *Design, Control and Application of Modular Multilevel Converters for HVDC Transmission Systems*: John Wiley & Sons, Ltd, 2016, pp. 133-213.

[14]   L. Harnefors, A. Antonopoulos, S. Norrga, L. Angquist, and H. P. Nee, "Dynamic Analysis of Modular Multilevel Converters," *IEEE Transactions on Industrial Electronics,* vol. 60, no. 7, pp. 2526-2537, 2013.

[15]   H. Nademi, A. Das, and L. E. Norum, "Modular Multilevel Converter With an Adaptive Observer of Capacitor Voltages," *IEEE Transactions on Power Electronics,* vol. 30, no. 1, pp. 235-248, 2015.

[16]   J. Qin and M. Saeedifard, "Predictive Control of a Modular Multilevel Converter for a Back-to-Back HVDC System," *IEEE Transactions on Power Delivery,* vol. 27, no. 3, pp. 1538-1547, 2012.

[17]   K. Ilves, L. Harnefors, S. Norrga, and H. P. Nee, "Predictive Sorting Algorithm for Modular Multilevel Converters Minimizing the Spread in the Submodule Capacitor Voltages," *IEEE Transactions on Power Electronics,* vol. 30, no. 1, pp. 440-449, 2015.

[18] J. Qin and M. Saeedifard, "Reduced Switching-Frequency Voltage-Balancing Strategies for Modular Multilevel HVDC Converters," *IEEE Transactions on Power Delivery,* vol. 28, no. 4, pp. 2403-2410, 2013.

[19] A. Hassanpoor, K. Ilves, S. Norrga, L. Ängquist, and H. P. Nee, "Tolerance-band modulation methods for modular multilevel converters," in *2013 15th European Conference on Power Electronics and Applications (EPE)*, 2013, pp. 1-10.

[20] B. P. McGrath and D. G. Holmes, "Multicarrier PWM strategies for multilevel inverters," *IEEE Transactions on Industrial Electronics,* vol. 49, no. 4, pp. 858-867, 2002.

[21] X. Shi, Z. Wang, L. M. Tolbert, and F. Wang, "A comparison of phase disposition and phase shift PWM strategies for modular multilevel converters," in *2013 IEEE Energy Conversion Congress and Exposition*, 2013, pp. 4089-4096.

[22] M. S. Rajan and R. Seyezhai, *Comparative study of multicarrier PWM techniques for a modular multilevel inverter*. 2013, pp. 4850-4865.

[23] I. Ouerdani, A. Bennani-Ben Abdelghani, and I. S. Belkhodja, *Harmonic analysis of pulse width modulation-based strategies for modular multilevel converter*. 2016, pp. 838-846.

[24] B. Li, R. Yang, D. Xu, G. Wang, W. Wang, and D. Xu, "Analysis of the Phase-Shifted Carrier Modulation for Modular Multilevel Converters," *IEEE Transactions on Power Electronics,* vol. 30, no. 1, pp. 297-310, 2015.

[25] K. Sharifabadi, L. Harnefors, H.-P. Nee, S. Norrga, and R. Teodorescu, *Design, Control, and Application of Modular Multilevel Converters for HVDC Transmission Systems*. John Wiley & Sons, Ltd, 2016.

[26] M. P. Kazmierkowski and L. Malesani, "Current control techniques for three-phase voltage-source PWM converters: a survey," *IEEE Transactions on Industrial Electronics,* vol. 45, no. 5, pp. 691-703, 1998.

[27] T. M. Rowan and R. J. Kerkman, "A New Synchronous Current Regulator and an Analysis of Current-Regulated PWM Inverters," *IEEE Transactions on Industry Applications,* vol. IA-22, no. 4, pp. 678-690, 1986.

[28] D. N. Zmood and D. G. Holmes, "Stationary frame current regulation of PWM inverters with zero steady-state error," *IEEE Transactions on Power Electronics,* vol. 18, no. 3, pp. 814-822, 2003.

[29] D. G. Holmes, T. A. Lipo, B. P. McGrath, and W. Y. Kong, "Optimized Design of Stationary Frame Three Phase AC Current Regulators," *IEEE Transactions on Power Electronics,* vol. 24, no. 11, pp. 2417-2426, 2009.

[30] R. Kabiri, D. G. Holmes, and B. P. McGrath, "Double synchronous frame current regulation of distributed generation systems under unbalanced voltage conditions without sequence current separation," in *2015 IEEE Applied Power Electronics Conference and Exposition (APEC)*, 2015, pp. 1822-1829.

[31] Y. Sato, T. Ishizuka, K. Nezu, and T. Kataoka, "A new control strategy for voltage-type PWM rectifiers to realize zero steady-state control error in input current," *IEEE Transactions on Industry Applications,* vol. 34, no. 3, pp. 480-486, 1998.

[32] D. N. Zmood, D. G. Holmes, and G. H. Bode, "Frequency-domain analysis of three-phase linear current regulators," *IEEE Transactions on Industry Applications,* vol. 37, no. 2, pp. 601-610, 2001.

[33] L. Harnefors and H. P. Nee, "Model-based current control of AC machines using the internal model control method," *IEEE Transactions on Industry Applications,* vol. 34, no. 1, pp. 133-141, 1998.

[34] L. Harnefors, K. Pietilainen, and L. Gertmar, "Torque-maximizing field-weakening control: design, analysis, and parameter selection," *IEEE Transactions on Industrial Electronics,* vol. 48, no. 1, pp. 161-168, 2001.

[35] K. Ilves, A. Antonopoulos, S. Norrga, and H. P. Nee, "Steady-State Analysis of Interaction Between Harmonic Components of Arm and Line Quantities of Modular Multilevel Converters," *IEEE Transactions on Power Electronics,* vol. 27, no. 1, pp. 57-68, 2012.

[36]   S. Golestan, E. Ebrahimzadeh, J. M. Guerrero, and J. C. Vasquez, "An Adaptive Resonant Regulator for Single-Phase Grid-Tied VSCs," *IEEE Transactions on Power Electronics,* vol. 33, no. 3, pp. 1867-1873, 2018.

[37]   G. Roedal, "Circulating Current Control for the Modular Multilevel Converter," MSc Research, Department of Electric Power Engineering, Norwegian University of Technology and Science, NTNU Gløshaugen, 2017.

[38]   D. Siemaszko, A. Antonopoulos, K. Ilves, M. Vasiladiotis, L. Ängquist, and H. P. Nee, "Evaluation of control and modulation methods for modular multilevel converters," in *The 2010 International Power Electronics Conference - ECCE ASIA -*, 2010, pp. 746-753.

[39]   A. Antonopoulos, L. Ängquist, L. Harnefors, K. Ilves, and H. P. Nee, "Global Asymptotic Stability of Modular Multilevel Converters," *IEEE Transactions on Industrial Electronics,* vol. 61, no. 2, pp. 603-612, 2014.

[40]   L. Harnefors, "Implementation of Resonant Controllers and Filters in Fixed-Point Arithmetic," *IEEE Transactions on Industrial Electronics,* vol. 56, no. 4, pp. 1273-1281, 2009.

[41]   R. Teodorescu, F. Blaabjerg, M. Liserre, and P. C. Loh, "Proportional-resonant controllers and filters for grid-connected voltage-source converters," *IEE Proceedings - Electric Power Applications,* vol. 153, no. 5, 2006.

[42]   J. O. G. Tande and K. Uhlen. Vindkraft i kraftsystemet [Online].

[43]   T. Remus, L. Marco, and R. Pedro, "Grid Synchronization in Single-Phase Power Converters," in *Grid Converters for Photovoltaic and Wind Power Systems*: Wiley-IEEE Press, 2011, p. 416.

Appendices

Appendix A - Matlab and Simulink Model

A.1 Model Topology and Measurement Block
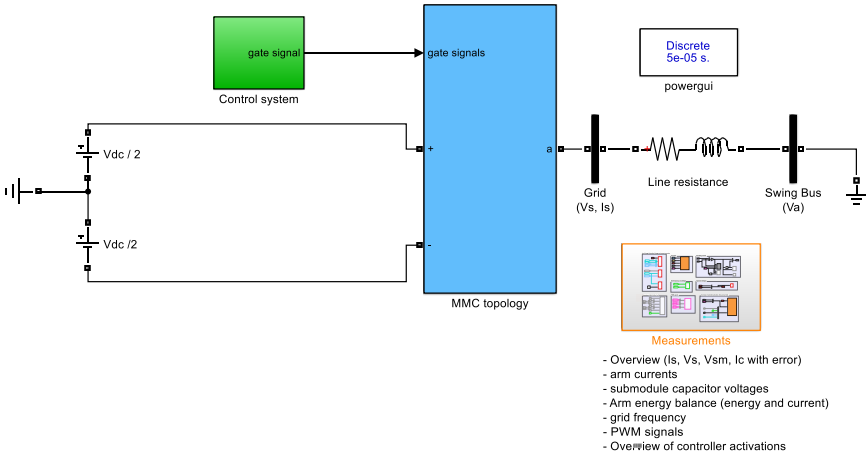
Figure A.1 MMC model
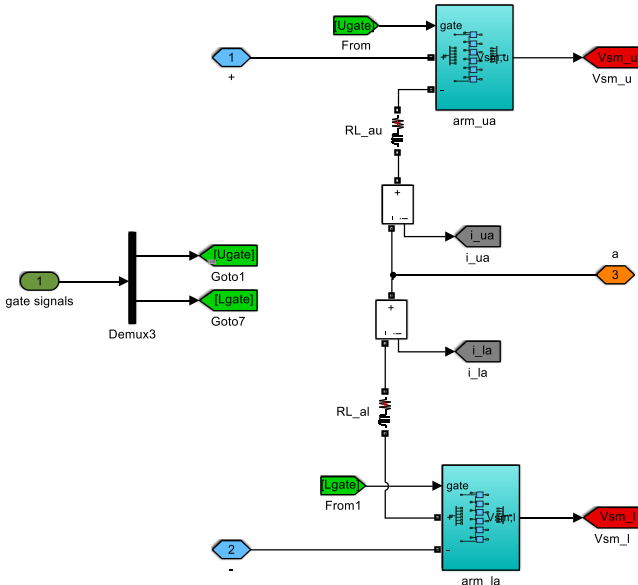
Figure A.2 Topology showing upper and lower arm
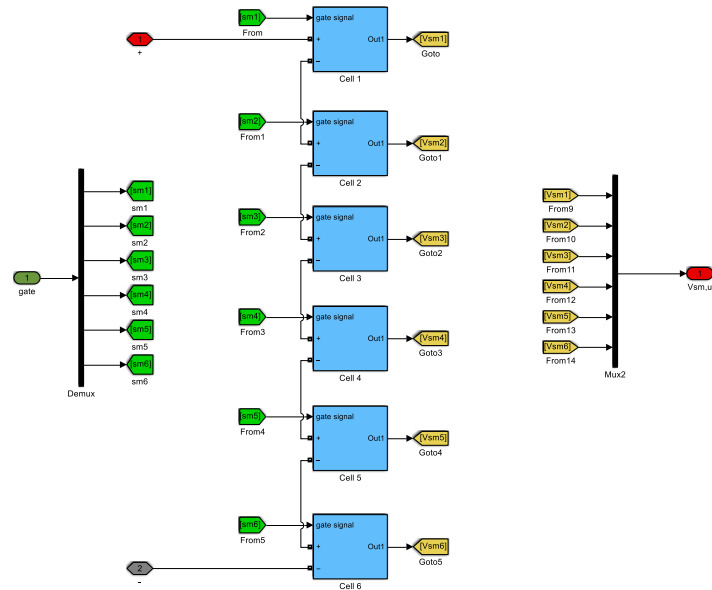
Figure A.3 The topology is equal for the upper and lower arm. Both arms consist of six submodules.
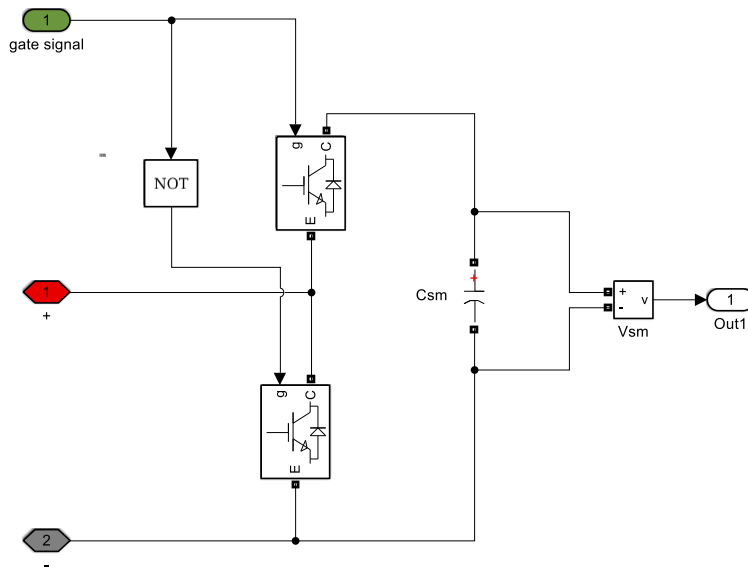
Figure A.4 Topology of the submodule.
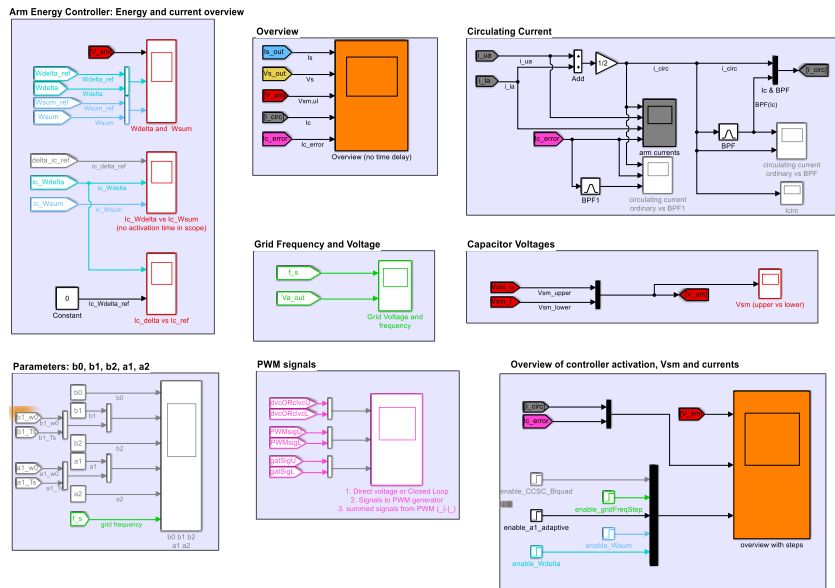
Figure A.5 All measurements of the converter.

A.2 Control System
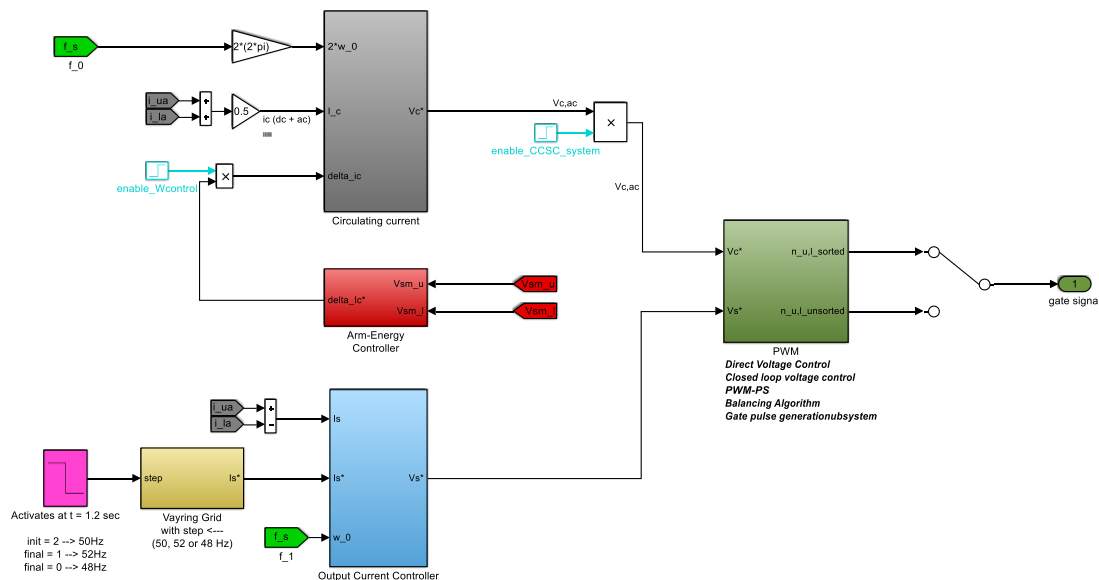
Figure A.6 Overview of the control system needed to operate the MMC.

CIRCULATING CURRENT CONTROL SYSTEM
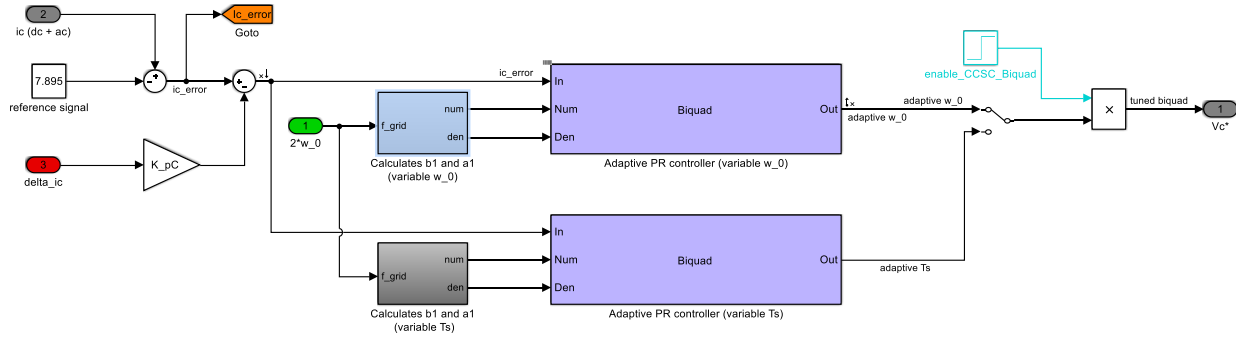
Figure A.7 Circulating current made adaptive using LUT. Plots of both the variable T_s and ω_0 filter.
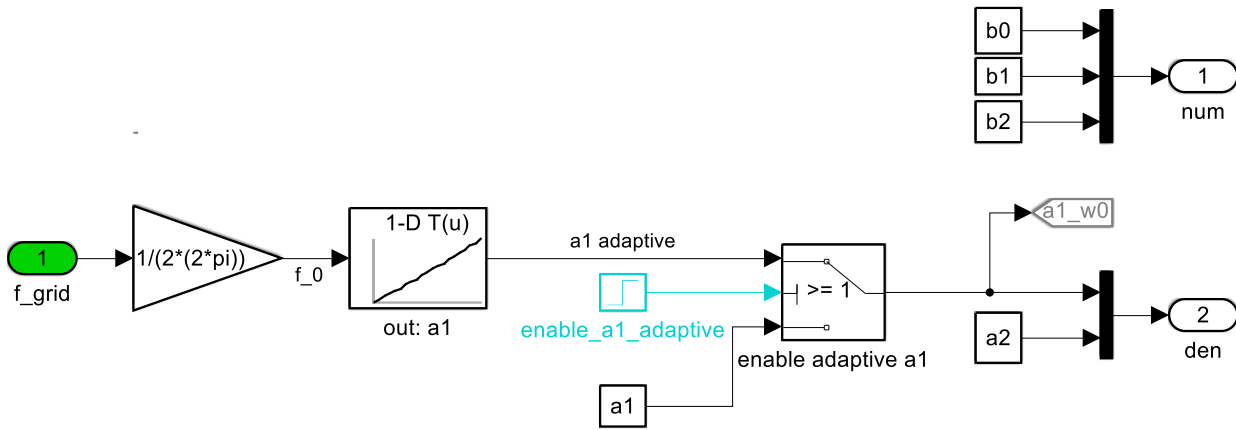
Figure A.8 Look-up table for finding variable a1.

OUTPUT CURRENT CONTROL
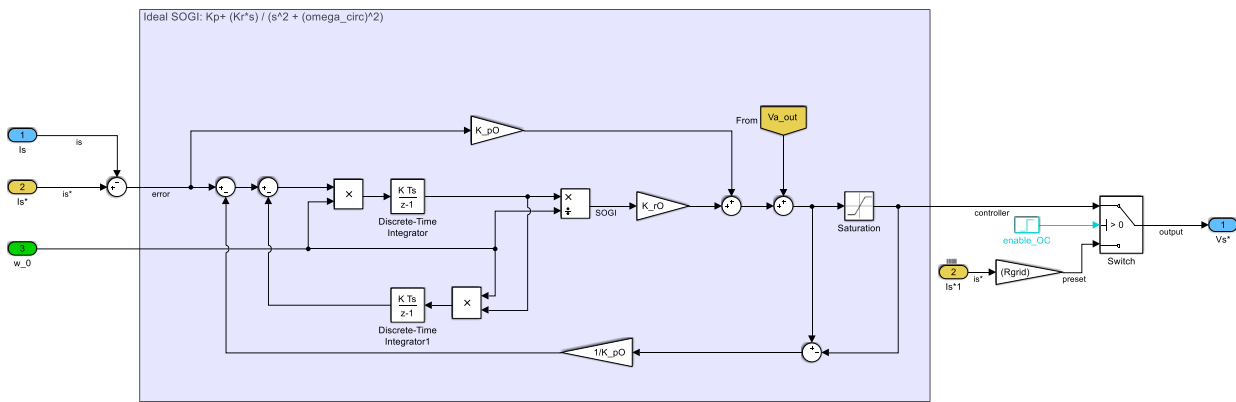
Figure A.9 Output Current Control

ARM ENERGY CONTROLLER
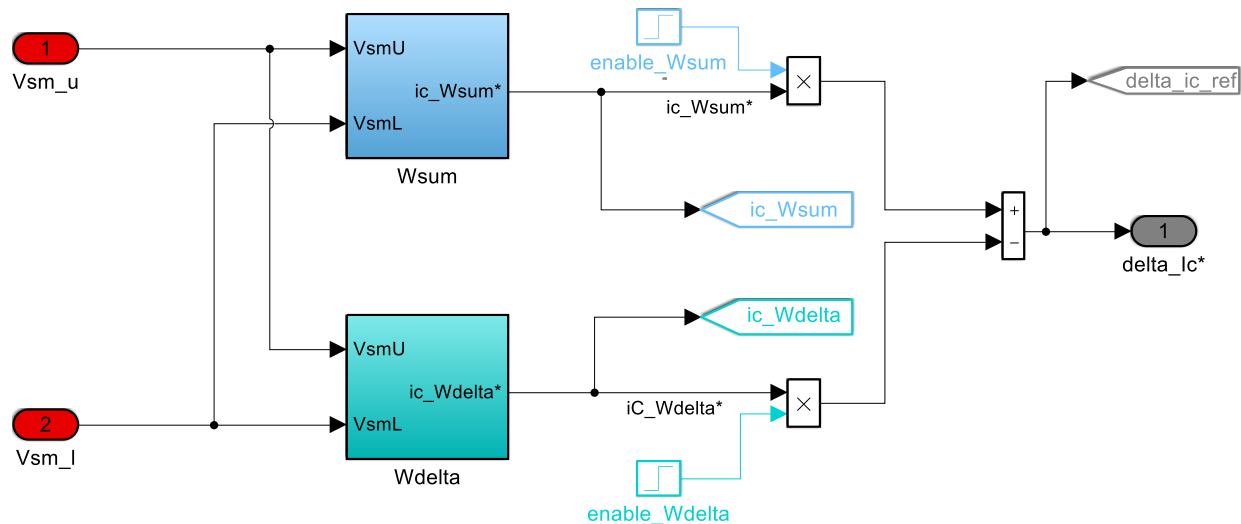
Figure A.10 Arm Energy Controller
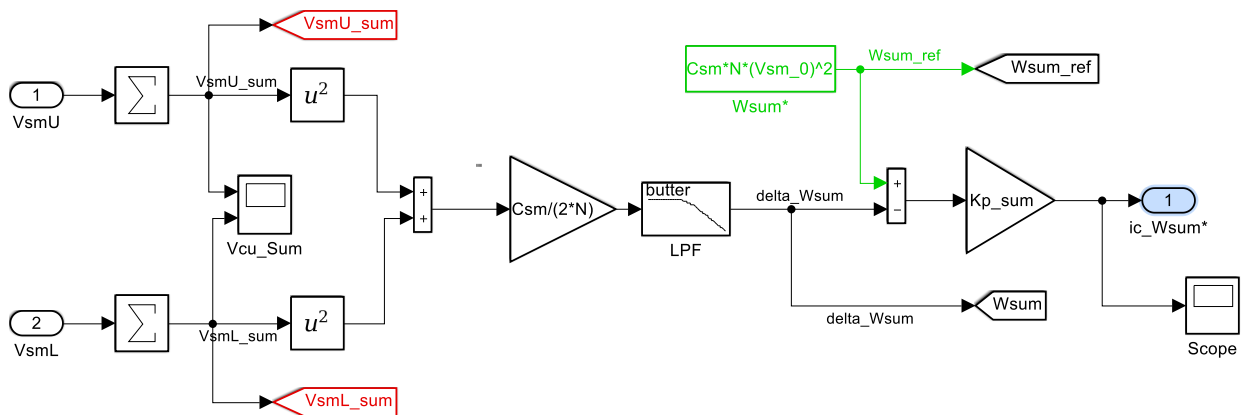
Figure A.11 Sum Energy Controller
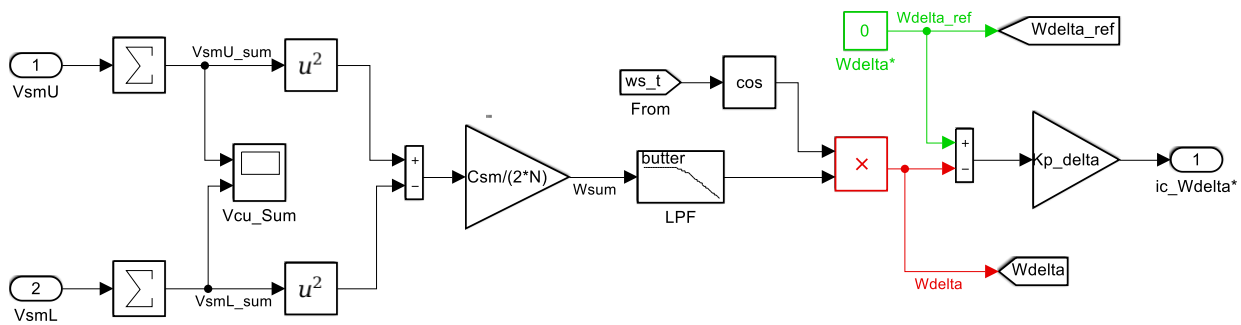
Figure A.12 Delta energy controller

101
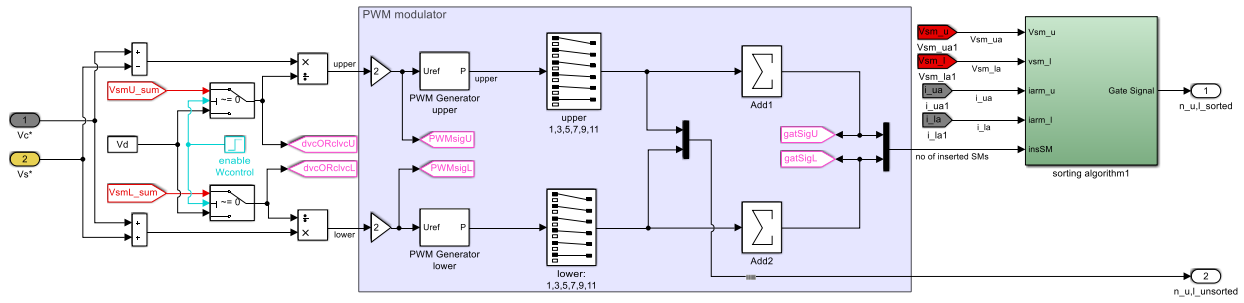
PWM CONTROLLER

Figure A.13 PWM controller.
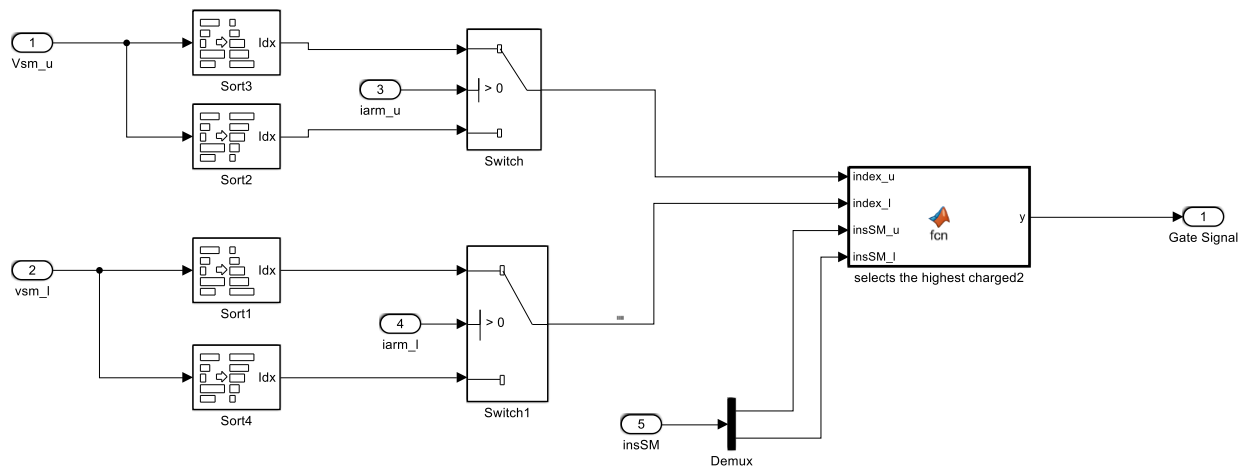
Figure A.14 Sorting algorithm with Matlab function.

THE SORTING ALGORITHM MATLAB FUNCTION IN FIGURE A.14

```
function y = fcn(index_u, index_l, insSM_u, insSM_l)

gatSig = zeros(1,2*length(index_u));
gatSig_u = zeros(1,length(index_u));
gatSig_l = zeros(1,length(index_l));

for i = 1:insSM_u
    gatSig_u(index_u(i))=1;
end

for j = 1:insSM_l
    gatSig_l(index_l(j))=1;
end
for i = 1:length(index_u)
    gatSig(i)=gatSig_u(i);
```

```matlab
        gatSig(i+length(index_l))=gatSig_l(i);
end
y = gatSig;
```

MATLAB SCRIPT – INITIALISATION NEEDED TO RUN THE SIMULINK MODEL

```matlab
clear all;
```

PARAMETERS

```matlab
discrete_time = 50e-6;

%Desired output voltage
Vs_rms = 230;
Vs_peak = Vs_rms * sqrt(2);

%DC bus
Vd = 2*Vs_rms*sqrt(2); % Vdc/2 = V

%Grid
Rgrid = 10;%Operational: 10 ohm. 0 ohm - short circuit. 10e6= open circuit;
Lgrid = 1e-3;
fgrid = 50;
w_0 = 2*pi*(fgrid);
Va_peak = 0; %Vs_peak;
Ph_a = 0; %Model works more smoothly by having Ph_a = 130. Suspeciouly synch errors?


%Submodule (First 6 values from datasheet. Values from ABB Datasheet)
N = 6; %number of SMs
Ron_IGBT =1/1400; %ohm @125 deg C
Lon_IGBT = 0; %H

Rsnubber = 1e12; %ohm.          IDEAL: Rsnubber = inf;
Csnubber = 1e-15;%10e-3; %F.    IDEAL: Csnubber = 0;

Csm = 10e-3;   %1=Battery ,10mF for operation.
Vsm_0=Vd/N; %

%Arm
Rarm = 0.1;
Larm = 10e-3;
```

PWM AND TIME DELAYS

```matlab
%carrier and switching
f_carrier = 540; %carrier frequency in PW. default= 540.
fsw = N*f_carrier; % -Switching frequency = SM*carrier frequency
w_sw = 2*pi*fsw;
Tsw = 1/fsw;
```

```matlab
%sampling frequency - based on Nyquist
fs = 2*fsw; %Sample frequency;Nyquist rule; fsample = 2*fswitching
w_s = 2*pi*fs;
Ts = Tsw/2;

%total time delay
Td = 1.5*Ts; %Td = 0.5Ts (PWM) + Ts (Tc - computational)
```

ACTIVATION OF CONTROLLERS

```matlab
enable_gridFreqStep = 2; %2; %1.2

%Adaptive a1 - Enable ON (1) or OFF (0) and time of activation
enable_a1_adaptive_onORoff = 1; %1/0 (on/off)
enable_b1_adaptive_onORoff = 0; %1/0 (on/off)

enable_a1_adaptive = 3; % seconds
enable_b1_adaptive = 10;   % seconds

% Activation time of controllers
enable_CCSC_system = 0; % 0 = on at 0s.  %total CCSC block
enable_CCSC = 1; %%Enables Biquad-Filter: Kp+Kr(s/(s^2+w_c*s+(h*w)^2));
enable_OC = 0; %Output current control: 0 = off.


%energy arm control
enable_Wsum = 5; %.8; %0.8clccl
enable_Wdelta = 4; % .8; %0.8
if enable_Wsum <= enable_Wdelta %enables the energy arm controller when the smallest activated
    enable_Wcontrol = enable_Wsum;
else
    enable_Wcontrol = enable_Wdelta;
end
```

OUTPUT CONTROLLER

```matlab
%Alpha is the same as previously.
alpha_cO =(w_s)/10; %((pi/2 - 0.2*pi)/(1.5*Ts))
alpha_rO = alpha_cO/20;

% Gain and parameters (circulating current)
LcO = Larm/2+Lgrid;   %Larm/2 + Lgrid;
RcO = Rarm/2+Rgrid; %Rarm/2 + Rgrid;

K_pO = alpha_cO * LcO;  %5
K_rO = 2*alpha_rO *K_pO;
```

ENERGY ARM CONTROLLER

```matlab
%filter
FiltO = 2; %Order of Butterworth filter.
```

```matlab
PB_freq = 10; %Hz
PB =2*pi*PB_freq;


%Gains
Kp_sum = PB/Vd/5;      %/5 %or 1 %taken from book model: Kp_sum = PB/Vd;
Kp_delta =PB/Vs_peak/10; %/1 works %taken from book model: Kp_delta =PB/Vs_peak;
```

CCSC CONTROLLER - FREQUENCIES AND SWITCHING SPEED

```matlab
alpha_cC = (w_sw)/(10); %10%((pi/2 - 0.2*pi)/1.5*fsw)= same %omega_sw*Nsm/10 (thumb of rule).
fsw = 540;
alpha_rC = alpha_cC/20; %Tuning says: /20.

% Gain and parameters (circulating current)
LcC = Larm;
RcC = Rarm;


K_pC = alpha_cC * LcC;
K_rC = 2*alpha_rC*alpha_cC*LcC; %2*alpha_rC *K_pC;


PM = (pi/2 - 1.5*alpha_cC*Ts)*180/pi; %phase margin [deg]
```

BIQUAD FILTER PARAMETERS

```matlab
Ts = 50e-6;
s = tf('s');
z = tf('z');
w_c = 0.1; %0.1;
h = 2; %the harmonic component to supress


Gprc_c = K_pC + K_rC*(s) /(s^2 + w_c*s + (h*w_0)^2); %creates tranfer function


c2dopts = c2dOptions('Method','tustin','PrewarpFrequency',h*w_0); %prewarps around the chosen
frequency; h*w
Gprd_c = c2d(Gprc_c,Ts,c2dopts); %creates discrete transfer function based on sampling time (Ts)
and preferred distretized method
[nz_cc,dz_cc]=tfdata(Gprd_c,'v') ; %return numerator and denumerator as vectors: v - vector

%sets the correct parameters for the DFII-t method
normz_cc=dz_cc(1,1); %value a0 is found. a0 is not neccessarily a0 =1  at this poin. (though it
is)
nz_cc=nz_cc/normz_cc; % devide the numereator by a0
dz_cc=dz_cc/normz_cc; %debide the denominator by a0 to get a0 = 1.

%Next line just chooses b0, b1,b2, a0, a1 and a2.
b0=nz_cc(1,1);
b1=nz_cc(1,2);
b2=nz_cc(1,3);
a0=dz_cc(1,1);% is also =1.
a1=dz_cc(1,2);
a2=dz_cc(1,3);
```

DISCRETISING AND CREATING VARIABLE A1 AND B1

```matlab
freqmat = 45:0.5:55;
paramat = zeros(length(freqmat),6);
%
% This for-loop
for i = 1:length(freqmat)
    w_var = 2*pi*freqmat(i); %variable omega

    Hpr=K_pC+K_rC*(s)/(s^2+w_c*s+(h*w_var)^2); %creates transfer function
    c2dopts = c2dOptions('Method','tustin','PrewarpFrequency',h*w_var); %prewarps around the
chosen frequency; h*w
    Hprz = c2d(Hpr,Ts,c2dopts); %creates discrete transfer function based on sampling time (Ts)
and preferred distretized method
    [nz_cc,dz_cc]=tfdata(Hprz,'v') ; %return numerator and denumerator as vectors: v - vector

    normz_cc=dz_cc(1,1); %value a0 is found. a0 =/ 1 at this point.
    nz_cc=nz_cc/normz_cc; % devide the numereator by a0
    dz_cc=dz_cc/normz_cc; %debide the denominator by a0 to get a0 = 1.

    %  Next line just chooses b0, b1,b2, a0, a1 and a2.
    paramat(i,1) = nz_cc(1,1); %b0
    paramat(i,2) = nz_cc(1,2);%b1
    paramat(i,3) = nz_cc(1,3);%b2
    paramat(i,4) = dz_cc(1,1); %dz_cc(1,1) is also 1.
    paramat(i,5) = dz_cc(1,2); %a1
    paramat(i,6) = dz_cc(1,3);%a2
end
```

DISCRETISING AND CREATING VARIABLE PARAMETERS OF A1,A2,B0,B1,B2 BASED ON Ts

```matlab
paramat_Ts = zeros(length(freqmat),6);
delta_Ts_mat = freqmat*1e-6;

for i = 1:length(delta_Ts_mat)

    a_var = K_rC*sin(h*w_0*(delta_Ts_mat(i)))/(2*(h*w_0+0.5*w_c*sin(h*w_0*(delta_Ts_mat(i)))));
    a1_var = -2*h*w_0*cos(h*w_0*(delta_Ts_mat(i)))/(h*w_0+0.5*w_c*sin(h*w_0*(delta_Ts_mat(i))));
    a2_var = (h*w_0-
0.5*w_c*sin(h*w_0*(delta_Ts_mat(i))))/(h*w_0+0.5*w_c*sin(h*w_0*(delta_Ts_mat(i))));

    b0_var = K_pC+a_var;
    b1_var = K_pC*a1_var;
    b2_var = K_pC*a2_var-a_var;

%     %  Next line just chooses b0, b1,b2, a0, a1 and a2.
    paramat_Ts(i,1) = b0_var; %b0
    paramat_Ts(i,2) = b1_var; %b1
    paramat_Ts(i,3) = b2_var; %b2
    paramat_Ts(i,4) = 1;      %a0 = 1
    paramat_Ts(i,5) = a1_var; %a1
    paramat_Ts(i,6) = a2_var; %a2
```

```matlab
    Gprc_c = K_pC + K_rC*(s) /(s^2 + w_c*s + (h*w_0)^2); %creates tranfer function

c2dopts = c2dOptions('Method','tustin','PrewarpFrequency',h*w_0); %prewarps around the chosen
frequency; h*w
Gprd_c = c2d(Gprc_c,delta_Ts_mat(i),c2dopts); %creates discrete transfer function based on
sampling time (Ts) and preferred distretized method
[nz_cc,dz_cc]=tfdata(Gprd_c,'v') ; %return numerator and denumerator as vectors: v - vector

%sets the correct parameters for the DFII-t method
normz_cc=dz_cc(1,1); %value a0 is found. a0 is not neccessarily a0 =1  at this poin. (though it
is)
nz_cc=nz_cc/normz_cc; % devide the numereator by a0
dz_cc=dz_cc/normz_cc; %debide the denominator by a0 to get a0 = 1.

%Next line just chooses b0, b1,b2, a0, a1 and a2.
paramat_Ts_new(i,1)=nz_cc(1,1);
paramat_Ts_new(i,2)=nz_cc(1,2);
paramat_Ts_new(i,3)=nz_cc(1,3);
paramat_Ts_new(i,4)=dz_cc(1,1);% is also =1.
paramat_Ts_new(i,5)=dz_cc(1,2);
paramat_Ts_new(i,6)=dz_cc(1,3);

end

% a1_comparison = [paramat(:,5) , paramat_Ts(:,5)];
a1_comparison = [paramat(:,5) , paramat_Ts(:,5), paramat_Ts_new(:,5)];
```

CALCULATES A₁, A₂, B₀, B₁ AND B₂ WITH DERIVED FORMULAS

```matlab
delta_Ts = 0;

aa = K_rC*sin(h*w_0*(Ts + delta_Ts))/(2*(h*w_0+0.5*w_c*sin(h*w_0*(Ts + delta_Ts))));
a11 = -2*h*w_0*cos(h*w_0*(Ts + delta_Ts))/(h*w_0+0.5*w_c*sin(h*w_0*(Ts + delta_Ts)));
a22 = (h*w_0-0.5*w_c*sin(h*w_0*(Ts + delta_Ts)))/(h*w_0+0.5*w_c*sin(h*w_0*(Ts + delta_Ts)));

b00 = K_pC+aa;
b11 = K_pC*a11;
b22 = K_pC*a22-aa;
```

Appendix B – Bode Plot Script

This appendix contains the Matlab script used for plotting continuous and discontinuous Bode plots.

B.1 Continuous Bode Plots

This script is used to plot the continuous Bode plots.

```
clear all;
```

PARAMETERS

```
noSM = 6;

%Grid
Rgrid = 10;%Operational: 10 ohm. 0 ohm - short circuit. 10e6= open circuit;
Lgrid = 1e-3;
fgrid = 50;

%Arm (THESE VALUES MUST BE CROSS-CHECKED)
Rarm = 0.1; %using 0 ohm gives a higher circulating currnet.
Larm = 10e-3;
```

PWM AND TIME DELAYS

```
%carrier and switching
f_carrier = 540; %carrier frequency in PW. default= 540.
fsw = noSM*f_carrier; % -Switching frequency = SM*carrier frequency
w_sw = 2*pi*fsw;
Tsw = 1/fsw;

%sampling frequency - based on Nyquist
fs = 2*fsw; %Sample frequency;Nyquist rule; fsample = 2*fswitching
w_s = 2*pi*fs;
Ts = Tsw/2;

%total time delay
Td = 1.5*Ts; %Td = 0.5Ts (PWM) + Ts (Tc - computational)
```

CONTROLLERS - PR (NON AND IDEAL)

CCSC CONTROLLER

```
alpha_c =(w_s)/10; %((pi/2 - 0.2*pi)/1.5*fsw)= same%omega_sw*Nsm/10 (thumb of rule). fsw = 540;
alpha_r = alpha_c/20;

w_c= 0.10; %sensitivty

w_50 = 2*pi*50; %
```

```
w_48 = 2*pi*48;
w_52 = 2*pi*52;


h=2; %harmonic order
```

GAIN AND PARAMETERS (CIRCULATING CURRENT)

```
Lc = Larm;  %Larm/2 + Lgrid;
Rc = Rarm; %Rarm/2 + Rgrid;


K_p = alpha_c * Lc;  %5
K_r = 2*alpha_r*alpha_c*Lc;
```

PR - IDEAL

```
%plots all bode plots for Kp = [40,20,10,5,2.5]
 res= linspace(2*pi*(2*(fgrid-5)),2*pi*(2*(fgrid+5)),1e6);
% res= linspace(2*pi*(1)),2*pi*((fgrid+950)),1e6);
k = 1;
for i = 1:6
    Gpr_48 = tf([1 0],[1 0 (h*w_48)^2])*K_r  + K_p;
    Gpr_50 = tf([1 0],[1 0 (h*w_50)^2])*K_r + K_p;
    Gpr_52 = tf([1 0],[1 0 (h*w_52)^2])*K_r + K_p;

    figure(i)
    bodePlots = bodeplot(Gpr_48, Gpr_50, Gpr_52,res);
    bodeOptions = getoptions(bodePlots); %write to get all options of bodeplot.
    bodeOptions.FreqUnits = 'Hz'; %creates Hz axis
    bodeOptions.PhaseVisible = 'off'; %returns plot without phase-axis
    bodeOptions.Grid = 'on';
    bodeOptions.FreqScale = 'log';
    setoptions(bodePlots,bodeOptions);

    title(['Kp= ' num2str(round(K_p,1)), ', Kr = ' num2str(round(K_r),4)]);
    legend('48 Hz','50 Hz','52 Hz'); %without omega_c
%   legend('48 Hz','50 Hz','52 Hz','50Hz \omega_c'); %with omega_c

    K_p = K_p/2;
    if K_p > 10
        alpha_c = alpha_c/2;
        alpha_r = alpha_c/20;
    end

    K_r = 2*alpha_r*alpha_c*Lc

end
```

NON IDEAL PR CONTROLLER

```
figure(1);
Gpr_50 = tf([1 0],[1 0 (h*w_50)^2])*K_r + K_p;
```

```matlab
bodePlots = bodeplot(Gpr_50,res);
hold on;
w_c0 = w_c;
for i = 1:6
    figure(1);
    hold on;
    if i >= 5
        w_c = 0.5;
        Gpr_50_Wc = tf([1 0],[1 w_c (h*w_50)^2])*K_r + K_p;
        if i == 6
            w_c =0.1;
            Gpr_50_Wc = tf([1 0],[1 w_c (h*w_50)^2])*K_r + K_p;
        end

    else
        Gpr_50_Wc = tf([1 0],[1 w_c (h*w_50)^2])*K_r + K_p;
        w_c = w_c/2;

    end
    bodePlots = bodeplot(Gpr_50_Wc,res);
end

hold off;

bodeOptions = getoptions(bodePlots); %write to get all options of bodeplot.
bodeOptions.FreqUnits = 'Hz'; %creates Hz axis
bodeOptions.PhaseVisible = 'off'; %returns plot without phase-axis
bodeOptions.Grid = 'on';
bodeOptions.FreqScale = 'log';
setoptions(bodePlots,bodeOptions);

title(['Kp= ' num2str(round(K_p,1)), ', Kr = ' num2str(round(K_r),4)]);
legend('\omega_c = 0',['\omega_c= ' num2str(w_c0)], ...
    ['\omega_{c}= ' num2str(w_c0/2,2)], ['\omega_c= ' num2str(w_c0/2^2,2)],...
    ['\omega_{c}= ' num2str(w_c0/2^3,3)],'\omega_c= 0.5', '\omega_c = 0.1'); %with omega_c
```

B.2 Discrete Transfer Functions

PARAMETERS

```
noSM = 6;


%Grid
Rgrid = 10;%Operational: 10 ohm. 0 ohm - short circuit. 10e6= open circuit;
Lgrid = 1e-3;
fgrid = 50;


%Arm (THESE VALUES MUST BE CROSS-CHECKED)
Rarm = 0.1; %using 0 ohm gives a higher circulating currnet.
Larm = 10e-3;
```

```
%carrier and switching
f_carrier = 540; %carrier frequency in PW. default= 540.
fsw = noSM*f_carrier; % -Switching frequency = SM*carrier frequency
w_sw = 2*pi*fsw;
Tsw = 1/fsw;


%sampling frequency - based on Nyquist
fs = 2*fsw; %Sample frequency;Nyquist rule; fsample = 2*fswitching
w_s = 2*pi*fs;
Ts = Tsw/2;


%total time delay
Td = 1.5*Ts; %Td = 0.5Ts (PWM) + Ts (Tc - computational)
```

CONTROLLERS - CCSC CONTROLLER

```
alpha_c =(w_s)/10; %((pi/2 - 0.2*pi)/1.5*fsw)= same%omega_sw*Nsm/10 (thumb of rule). fsw = 540;
alpha_r = alpha_c/20;

w_50 = 2*pi*50;
w_48 = 2*pi*48;
w_52 = 2*pi*52;


h=2; %harmonic order
```

GAIN AND PARAMETERS (CIRCULATING CURRENT)

```
Lc = Larm;
Rc = Rarm;


K_p = alpha_c * Lc;   %5
K_r = 2*alpha_r*alpha_c*Lc;
```

BODE PLOTS- PR CONTROLLERS

```
res= linspace(2*pi*(2*(fgrid-.05)),2*pi*(2*(fgrid+.05)),1e6);
```

PR - IDEAL AND NON-IDEAL DISCRETE

```
Ts=52e-6;
w_c= 0.1; %sensitivty

%Continous
s=tf('s'); %allows "s" to be used as derivator in tf.
Hpr_ideal = K_p + K_r*(s)/(s^2+(h*w_50)^2);
Hpr_nonIdeal = K_p + K_r*(s)/(s^2+w_c*s+(h*w_50)^2);

%discrete
z=tf('z'); %allows "z" to be used as derivator in tf

c2dopts = c2dOptions('Method','tustin','PrewarpFrequency',h*w_50); %prewarps around the chosen
frequency; h*w
Hprz_nonIdeal = c2d(Hpr_nonIdeal,Ts,c2dopts); %creates discrete transfer function based on
sampling time (Ts) and preferred distretized method
[nz_cc,dz_cc]=tfdata(Hprz_nonIdeal,'v') ; %return numerator and denumerator as vectors: v -
vector

normz_cc=dz_cc(1,1); %value a0 is found. a0 =/ 1 at this point.
nz_cc=nz_cc/normz_cc; % devide the numereator by a0
dz_cc=dz_cc/normz_cc; %debide the denominator by a0 to get a0 = 1.

%Next line just chooses b0, b1,b2, a0, a1 and a2.
b0=nz_cc(1,1);
b1=nz_cc(1,2);
b2=nz_cc(1,3);
a0=1; %dz_cc(1,1) is also 1.
a1=dz_cc(1,2);
a2=dz_cc(1,3);

parameters = tf([b0 b1 b2], [a0 a1 a2])

% Bode Plot
bodePlots = bodeplot(Hpr_ideal, Hprz_nonIdeal,res);
bodeOptions = getoptions(bodePlots); %write to get all options of bodeplot.
bodeOptions.FreqUnits = 'Hz'; %creates Hz axis
bodeOptions.PhaseVisible = 'off'; %returns plot without phase-axis
bodeOptions.Grid = 'on';
bodeOptions.FreqScale = 'log';
setoptions(bodePlots,bodeOptions);
```

Appendix C – Pulse Width Modulation Models

The following PWM models were used to simulate the PWM signals in section 2.3. The same models are also used in the specialisation project conducted autumn 2017.

PHASE OPPOSITION PWM (PO-PWM)
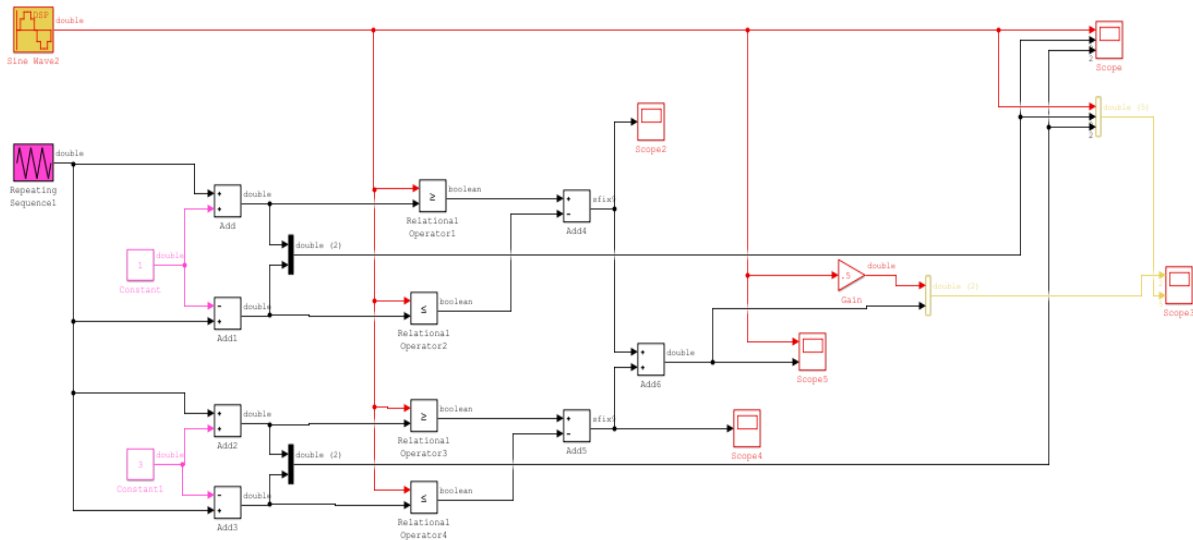
Figure C.1 The Simulink model for creating the PO-PWM signal

PHASE OPPOSITION DISPOSITION PWM (POD-PWM)
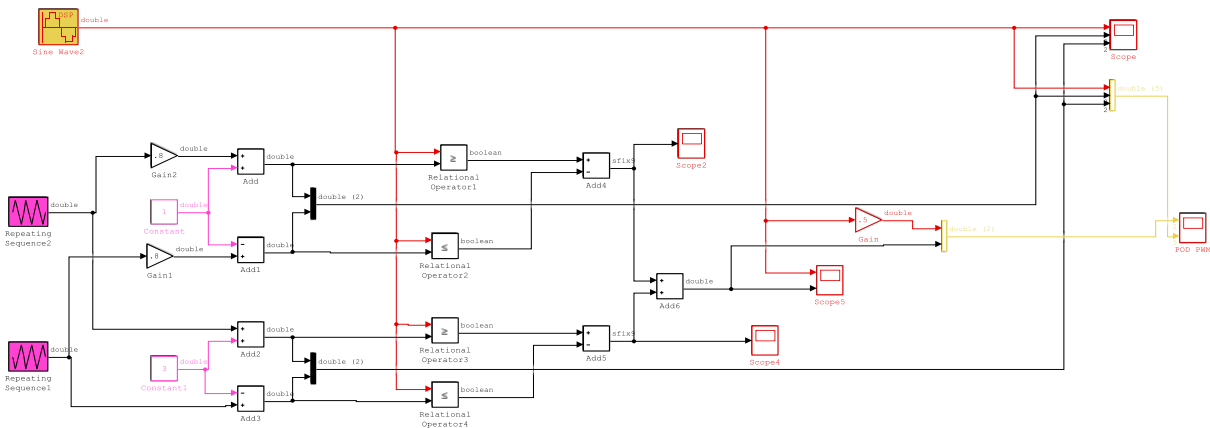
Figure C.2 The Simulink model for creating the POD-PWM signal.

Different amplitude of the two middle carriers.

ALTERNATE PHASE OPPOSITION DISPOSITION PWM (APOD-PWM)
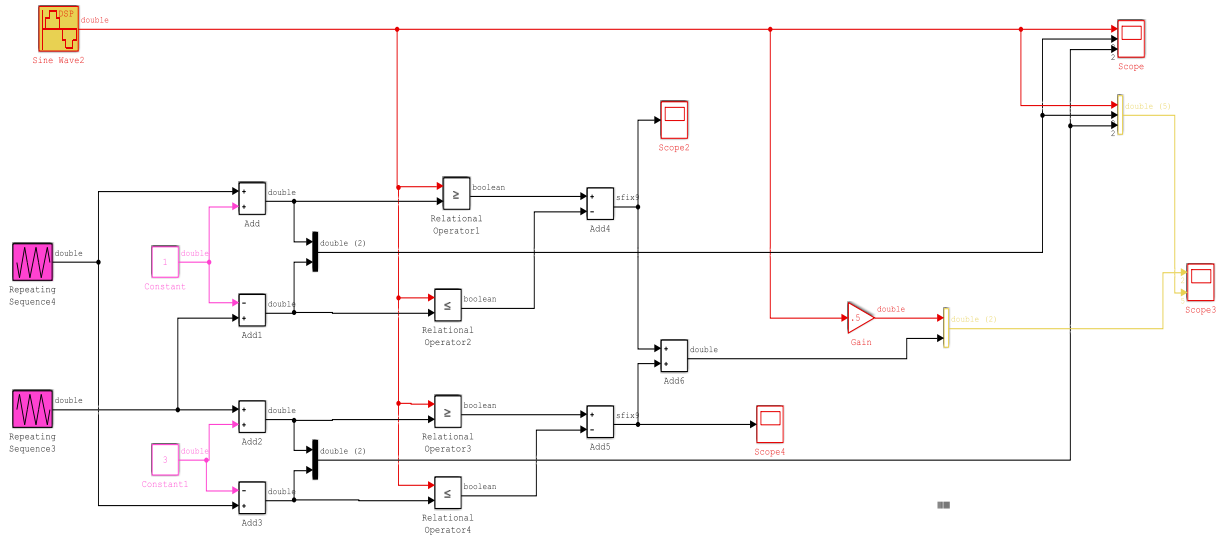
Figure C.3 The Simulink model for creating the APOD-PWM signal.

PHASE SHIFTED PWM (PS-PWM)
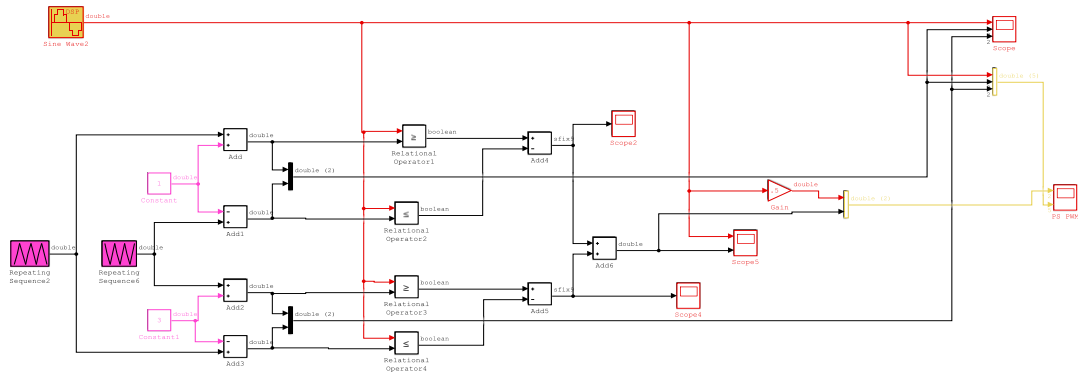
Figure C.4 The Simulink model for creating the PS-PWM signal.